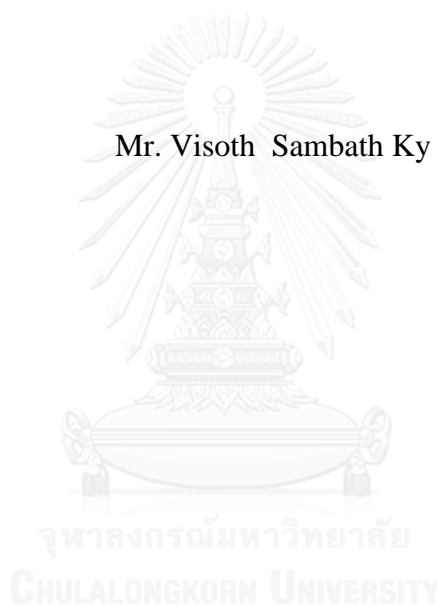


NONLINEAR INELASTIC ANALYSIS OF CONCRETE ENCASED STEEL
STRUCTURES

Mr. Visoth Sambath Ky



บทคัดย่อและแฟ้มข้อมูลฉบับเต็มของวิทยานิพนธ์ตั้งแต่ปีการศึกษา 2554 ที่ให้บริการในคลังปัญญาจุฬาฯ (CUIR)
เป็นแฟ้มข้อมูลของนิสิตเจ้าของวิทยานิพนธ์ ที่ส่งผ่านทางบัณฑิตวิทยาลัย

The abstract and full text of theses from the academic year 2011 in Chulalongkorn University Intellectual Repository (CUIR)
are the thesis authors' files submitted through the University Graduate School.

A Dissertation Submitted in Partial Fulfillment of the Requirements
for the Degree of Doctor of Philosophy Program in Civil Engineering

Department of Civil Engineering

Faculty of Engineering

Chulalongkorn University

Academic Year 2014

Copyright of Chulalongkorn University

การวิเคราะห์ไม่ยึดหยุ่น ไร้เชิงเส้นของโครงสร้างเหล็กหุ้มด้วยคอนกรีต



วิทยานิพนธ์นี้เป็นส่วนหนึ่งของการศึกษาตามหลักสูตรปริญญาวิศวกรรมศาสตรดุษฎีบัณฑิต

สาขาวิชาวิศวกรรมโยธา ภาควิชาวิศวกรรมโยธา

คณะวิศวกรรมศาสตร์ จุฬาลงกรณ์มหาวิทยาลัย

ปีการศึกษา 2557

ลิขสิทธิ์ของจุฬาลงกรณ์มหาวิทยาลัย

| | |
|-------------------|---|
| Thesis Title | NONLINEAR INELASTIC ANALYSIS OF CONCRETE ENCASED STEEL STRUCTURES |
| By | Mr. Visoth Sambath Ky |
| Field of Study | Civil Engineering |
| Thesis Advisor | Professor Thaksin Thepchatri, Ph.D. |
| Thesis Co-Advisor | Sawekchai Tangaramvong, Ph.D. |

Accepted by the Faculty of Engineering, Chulalongkorn University in
Partial Fulfillment of the Requirements for the Doctoral Degree

..... Dean of the Faculty of Engineering
(Professor Bundhit Eua-arporn, Ph.D.)

THESIS COMMITTEE

..... Chairman
(Professor Teerapong Senjuntichai, Ph.D.)

..... Thesis Advisor
(Professor Thaksin Thepchatri, Ph.D.)

..... Thesis Co-Advisor
(Sawekchai Tangaramvong, Ph.D.)

..... Examiner
(Associate Professor Akhrawat Lenwari, Ph.D.)

..... Examiner
(Assistant Professor Withit Pansuk, Ph.D.)

..... External Examiner
(Associate Professor Sayan Sirimontree, Ph.D.)

วิศุท สมบัติ ที : การวิเคราะห์ไม่ยืดหยุ่น ไร้เชิงเส้นของโครงสร้างเหล็กหุ้มด้วยคอนกรีต (NONLINEAR INELASTIC ANALYSIS OF CONCRETE ENCASED STEEL STRUCTURES) อ.ที่ปรึกษาวิทยานิพนธ์หลัก: ทักษิณ เทพชาติ, อ.ที่ปรึกษาวิทยานิพนธ์ร่วม: เสวกชัย ตั้งอร่ามวงศ์, 167 หน้า.

คุณิพนธ์นี้นำเสนอระเบียบวิธีเชิงตัวเลขที่มีประสิทธิภาพในการจำลองพฤติกรรมแบบไม่ยืดหยุ่น ไร้เชิงเส้น ได้อย่างสมบูรณ์ สำหรับเสา/คาน-เสาเหล็กหุ้มด้วยคอนกรีต (concrete encased steel หรือ CES) ทั้งชนิดสั้นและชะลูด โดยวิธีไฟเบอร์เอลิเมนต์ การวิเคราะห์ได้คำนึงถึงหลายอิทธิพลหลัก ได้แก่ ความไร้เชิงเส้นวัสดุ ความไร้เชิงเส้นเรขาคณิต ความไม่สมบูรณ์เรขาคณิต ระดับการจำกัดขอบเขตของคอนกรีต และการโค้งเดาะเฉพาะที่ของเหล็กโครงสร้าง และเหล็กเสริม (rebar) อนึ่ง หน้าตัด CES ที่ใช้ในการศึกษามีเหล็กโครงสร้างหน้าตัด H, I และกากบาท (cross-shaped) โดยจะมี/ไม่มีเหล็กเสริมร่วมด้วยก็ได้

ระเบียบวิธีเชิงตัวเลขที่พัฒนานี้ มีความสามารถในการศึกษาสมรรถภาพของโครงสร้างประเภทวัสดุผสมได้อย่างสมบูรณ์ ได้แก่เส้นแสดงความสัมพันธ์ระหว่างแรง-การโก่งตัว แรง-ความเครียด/การหดตัวในแนวแกน เส้นปฏิสัมพันธ์ของแรงแนวแกน-โมเมนต์ และแรง-โมเมนต์-ความโค้ง อนึ่ง ในขั้นตอนการคำนวณ ได้นำเสนอแนวทางการกำหนดสภาวะเริ่มต้นที่ปรับค่าได้ ทำงานร่วมกับระเบียบวิธีเชิงตัวเลขมุลเลอร์ (Müller) เพื่อให้การคำนวณคู่เข้าค่าตอบได้อย่างเสถียร และจากการเปรียบเทียบกับผลการทดลองในอดีตจำนวน 50 ตัวอย่าง ซึ่งมีทั้งเสา และคาน-เสาวัสดุผสมขนาดต่างๆ พบว่า มีความถูกต้องดี

ในการศึกษานี้ได้มีการนำเสนอแบบจำลองการครากเชิงเส้นเป็นช่วงแทนคุณสมบัติการอ่อนตัวของหน้าตัด CES และสูตรทางคณิตศาสตร์สำหรับใช้คำนวณค่าต่างๆ ที่เป็นส่วนประกอบความเป็นพลาสติก ซึ่งความแม่นยำของแบบจำลองนี้ได้รับการตรวจสอบโดยเปรียบเทียบกับผลการทดสอบในอดีต จากนั้นได้นำวิธีโฮโลโนมิกเชิงวิเคราะห์ที่ละชั้นทำการศึกษาผลการสนองไร้เชิงเส้นของโครงสร้าง CES ผลการวิเคราะห์สามารถแสดงพฤติกรรมพร้อมกับลำดับการเกิดของจุดหมุนพลาสติก ณ ตำแหน่งต่างๆ ในโครงสร้าง CES ได้อย่างสมบูรณ์ สุดท้ายได้นำเสนอผลการศึกษานำค้ำยันเหล็กไปใช้ในการเสริมกำลังโครงสร้าง รวมทั้งให้คำแนะนำแนวทางการเลือกประเภทค้ำยันที่เหมาะสมในโครงสร้างที่ได้ทำการศึกษา

ภาควิชา วิศวกรรมโยธา

สาขาวิชา วิศวกรรมโยธา

ปีการศึกษา 2557

ลายมือชื่อนิสิต

ลายมือชื่อ อ.ที่ปรึกษาหลัก

ลายมือชื่อ อ.ที่ปรึกษาร่วม

5671451021 : MAJOR CIVIL ENGINEERING

KEYWORDS: NONLINEAR INELASTIC ANALYSIS / COMPOSITE STRUCTURE / CONCRETE ENCASED STEEL COLUMN/BEAM-COLUMN / POST-PEAK SOFTENING RESPONSE / STRUCTURAL RETROFITTING / STEEL BRACING

VISOTH SAMBATH KY: NONLINEAR INELASTIC ANALYSIS OF CONCRETE ENCASED STEEL STRUCTURES. ADVISOR: PROF. THAKSIN THEPCHATRI, Ph.D., CO-ADVISOR: DR. SAWEKCHAI TANGARAMVONG, Ph.D., 167 pp.

This dissertation presents an efficient numerical approach based on fiber element method to simulate the complete nonlinear inelastic behaviors of stub and slender concrete encased steel (CES) columns/beam-columns. The analysis scheme accommodates various important influences, i.e. materials and geometric nonlinearity, geometric imperfection, levels of concrete confinement, local buckling of structural steel and reinforcement bar. CES sections having H-, I-, and Cross-shaped steel with/without reinforcement bars were investigated.

The developed approach is capable of tracing the complete structural performance such as load-lateral deflection curve, load-axial strain/shortening response, force-moment interaction diagram, and force-moment-curvature curve. An adaptive initial condition formulation with Müller numerical method has been developed to ensure the convergence solution. A total of 50 full-scale experimental tests of CES columns/beam-columns were used to validate the developed numerical approach. Good comparisons between the analysis and experimental tests have been achieved.

A novel piecewise linear yield model of softening material properties underpinning CES sections have been proposed. Mathematical expressions for plasticity components were derived and validated with tests. The stepwise holonomic analysis approach has been adopted to trace the complete responses of structures with CES members. Both geometric and material nonlinearity were included in the analysis of CES structures. The proposed analysis method can predict CES structural behaviors with panoramas illustrations of plastic hinge. Structural retrofitting by means of typical steel bracings has been carried out. Some recommendations were given to select a suitable type of bracing configurations for the desired purpose.

Department: Civil Engineering

Student's Signature

Field of Study: Civil Engineering

Advisor's Signature

Academic Year: 2014

Co-Advisor's Signature

ACKNOWLEDGEMENTS

First of all, I would like to express my deep gratitude and sincere appreciation to my dissertation advisor, Professor Thaksin Thepchatri, for his productive academic guidance, very kind assistance, and strong support. I am truly thankful for his invaluable time, encouragement, and attention to listen and discuss issues with me. In addition to his great academic contribution, his positive personalities exceptionally inspire my life as well as my future academic profession.

My profound thanks and grateful gratitude go to my co-advisor, Dr. Sawekchai Tangaramvong (The University of New South Wales), for his constructive advice, valuable time, and continuous support. His insight and fruitful discussion have given me a better understanding regarding mathematical programming and stepwise holonomic elastoplastic analysis.

I also would like to thank all committee members for reviewing and giving constructive comments to qualify this dissertation; Associated Professor Qing Quan Liang (Victoria University) for enlightening discussion concerning Müller's method; lecturers and professors at Institute of Technology of Cambodia and Chulalongkorn University for providing me engineering knowledge to conduct my researches.

The PhD scholarship supported by Chulalongkorn University is gratefully acknowledged. I wish to thank all scholarship coordinators and administrative staffs at Chulalongkorn University for their kind facilitation and friendly environment.

I sincerely appreciate my dear wife, John Sara, for her remarkable patience, sweet encouragement, unwavering support, and warming care. I also would like to thank my brothers, sisters, and friends for their prayers and encouragement.

It is my great honor to specially dedicate my PhD dissertation to my beloved parents, Ky Bakchuor (1948–2011) and Sou Hon, who always love, advice, encourage, and support me. They own my endless gratitude and deepest love.

Above all, I would like to thank the living God, Jesus Christ, with all my heart and all my soul for being my Lord and Savior. He granted my prayers that I wished to finish PhD within two years and to have a first baby girl, Ky Visoth Anita (13/02/2015).

CONTENTS

| | Page |
|---|------|
| THAI ABSTRACT | iv |
| ENGLISH ABSTRACT..... | v |
| ACKNOWLEDGEMENTS | vi |
| CONTENTS..... | vii |
| CHAPTER 1 INTRODUCTION | 1 |
| 1.1 Concrete Encased Steel (CES) Structures | 1 |
| 1.2 Motivation | 2 |
| 1.3 Research Objectives and Scopes | 3 |
| 1.4 Research Methodology | 4 |
| 1.5 Layout of the Thesis | 5 |
| CHAPTER 2 LITERATURE REVIEW | 8 |
| 2.1 Introduction | 8 |
| 2.2 Concrete Encased Steel Columns and Beam-Columns | 9 |
| 2.2.1 Experimental Studies..... | 9 |
| 2.2.2 Nonlinear Analysis Approaches | 14 |
| 2.3 Steel–Concrete Composite Frames..... | 16 |
| 2.4 Structural Bracing Systems | 18 |
| CHAPTER 3 CONSTITUTIVE MODELS OF MATERIALS | 22 |
| 3.1 Introduction | 22 |
| 3.2 Concrete..... | 23 |
| 3.2.1 Concrete in Compression | 23 |
| 3.2.2 Concrete in Tension..... | 28 |
| 3.3 Structural Steel | 29 |
| 3.3.1 Structural Steel in Compression | 29 |
| 3.3.2 Structural Steel in Tension | 30 |
| 3.4 Reinforcement Bar..... | 32 |
| 3.4.1 Reinforcement Bar in Compression | 32 |
| 3.4.2 Reinforcement Bar in Tension | 33 |

| | Page |
|--|------|
| CHAPTER 4 NONLINEAR INELASTIC NUMERICAL MODELS OF CONCRETE ENCASED STEEL SECTIONS | 34 |
| 4.1 Introduction | 34 |
| 4.2 Concrete Confinement Zones | 35 |
| 4.3 Fiber Element Method | 36 |
| 4.3.1 Assumptions | 36 |
| 4.3.2 Discretization of Composite Sections | 37 |
| 4.4 Strain-Curvature Relationships | 37 |
| 4.5 Stress Resultants | 40 |
| CHAPTER 5 CONCRETE ENCASED STEEL COLUMNS UNDER AXIAL COMPRESSION..... | 42 |
| 5.1 Introduction | 42 |
| 5.2 Numerical Analysis Approach | 43 |
| 5.2.1 Imperfection and Buckling Modeling of Composite Columns | 43 |
| 5.2.2 Müller's Algorithm..... | 44 |
| 5.2.3 Computational Procedures for Load and Axial Strain Responses | 47 |
| 5.3 Validation of the Numerical Approach | 52 |
| 5.3.1 Summary of Relevant Experimental Tests | 52 |
| 5.3.2 Comparison between the numerical and experimental results | 56 |
| 5.4 Parametric Sensitivity Analyses | 61 |
| 5.4.1 Description of Parameters | 61 |
| 5.4.2 Results and Discussions | 63 |
| 5.5 Concluding Remarks | 66 |
| CHAPTER 6 CONCRETE ENCASED STEEL COLUMNS UNDER COMBINED AXIAL COMPRESSION AND UNIAXIAL BENDING..... | 69 |
| 6.1 Introduction | 69 |
| 6.2 Geometrically Nonlinear Analysis of CES Beam-Columns | 70 |
| 6.2.1 Eccentric Load and Buckling Modeling of Beam-Columns | 70 |
| 6.2.2 Numerical Method for Nonlinear Analysis | 72 |

| | Page |
|---|-----------|
| 6.2.3 Computational Procedures for Load and Lateral Deflection Responses.. | 74 |
| 6.3 Validation of the Numerical Approach | 79 |
| 6.3.1 Summary of Relevant Experimental Tests | 79 |
| 6.3.2 Comparison between the numerical and experimental results | 82 |
| 6.4 Parametric Sensitivity Analyses | 84 |
| 6.4.1 Description of Parameters | 84 |
| 6.4.2 Effects of eccentricity ratios with different effective length ratios | 87 |
| 6.4.3 Effects of concrete strength with different effective length ratios | 91 |
| 6.4.4 Effects of steel strength with different effective length ratios | 94 |
| 6.5 Concluding Remarks | 97 |
| CHAPTER 7 PERFORMANCE ASSESSMENT OF CES STRUCTURES AND STRENGTHENING WITH STEEL BRACING SYSTEMS..... | 99 |
| 7.1 Introduction | 99 |
| 7.2 Mathematical Programming Tools | 100 |
| 7.3 Plasticity Model..... | 102 |
| 7.3.1 Review of Yield Criterion | 102 |
| 7.3.2 Yield Criterion and Softening Rule for CES sections..... | 111 |
| 7.4 Validation of Proposed Plasticity Components with Experimental Tests..... | 118 |
| 7.5 Performance Assessment of CES Structures | 122 |
| 7.5.1 Description of Illustrative Examples | 122 |
| 7.5.2 Example 1: Three-bay, two-story rigid frame | 123 |
| 7.5.3 Example 2: Five-bay, five-story rigid frame | 126 |
| 7.5.4 Example 3: Three-bay, twelve-story rigid frame | 130 |
| 7.6 Strengthening of CES Structures with Common Steel Bracings..... | 136 |
| 7.6.1 Description of Retrofitted Structures | 136 |
| 7.6.2 Example 4: Strengthening a three-bay, two-story rigid frame | 137 |
| 7.6.3 Example 5: Strengthening a five-bay, five-story rigid frame..... | 141 |
| 7.6.4 Example 6: Strengthening a three-bay, twelve-story rigid frame | 145 |
| 7.7 Concluding Remarks | 150 |

| | Page |
|--|------|
| CHAPTER 8 | 152 |
| CONCLUSIONS AND RECOMMENDATIONS | 152 |
| 8.1 Summary..... | 152 |
| 8.2 Concluding Remarks | 154 |
| 8.3 Recommendations for Future Research..... | 155 |
| REFERENCES | 157 |
| VITA..... | 167 |



LIST OF TABLES

| | |
|---|-----|
| Table 5.1: Dimensions, steel sections, and material strength of CES column specimens..... | 52 |
| Table 5.2: Reinforcement bar and structural steel details of CES column specimens..... | 55 |
| Table 5.3: Comparisons between the numerical analyses with the test results..... | 57 |
| Table 5.4: Parametric variations of specimen dimensions and material properties of concrete encased steel composite columns..... | 62 |
| Table 5.5: Ultimate strength by the present analysis with parametric variations | 64 |
| Table 6.1: Specimen dimensions and material properties of CES beam-columns | 79 |
| Table 6.2: Detailed section dimensions and reinforcement of CES beam-columns... | 80 |
| Table 6.3: Comparison between numerical approach with tests and previous researchers..... | 82 |
| Table 6.4: Dimensions and material properties of CES parametric beam-columns... | 86 |
| Table 6.5: Results of the verified numerical approach for parametric study..... | 88 |
| Table 7.1: Properties of CES composite columns for example 1. | 124 |
| Table 7.2: Properties of CES composite columns for example 2. | 127 |
| Table 7.3: Properties of CES composite columns for example 3. | 132 |

LIST OF FIGURES

| | |
|---|----|
| Figure 2.1: Unconfined, partially confined, highly confined concrete for encased H-shaped, I-shaped, and Cross-shaped steel composite sections. | 15 |
| Figure 2.2: A Load and displacement response of composite frame, and beam-column joint by FEM (Li et al. 2012). | 17 |
| Figure 2.3: Bracing configurations (Taranath 2011). | 19 |
| | |
| Figure 3.1: Stress-strain curves of unconfined and confined concrete (Mander et al. 1988). | 26 |
| Figure 3.2: Stress-strain curves of unconfined, partially confined, and highly confined concrete. | 27 |
| Figure 3.3: Stress-strain relationship of concrete in tension. | 28 |
| Figure 3.4: Stress-strain relationship of structural steel in compression. | 30 |
| Figure 3.5: Stress-strain relationship of structural steel in tension. | 32 |
| Figure 3.6: Stress-strain relationship for reinforcement bar in compression. | 33 |
| | |
| Figure 4.1: Confinement zones and fiber element discretization of CES sections. | 36 |
| Figure 4.2: Strain-curvature relationship using fiber element model. | 38 |
| | |
| Figure 5.1: Concentrically applied force and initial imperfection of a pin-ended column. | 44 |
| Figure 5.2: Flowchart summarizing the analysis procedures to obtain axial load and strain responses of concrete encased steel composite columns. | 51 |
| Figure 5.3: Cross-section configurations of CES columns (a) H-, I-shaped with distributed rebar, (b) H-, I-shaped with corner rebar, (c) H-, I-shaped without rebar, (d) Cross-shaped with distributed rebar, and (e) Cross-shaped with corner rebar. | 54 |
| Figure 5.4: Axial load and strain response from the present analysis approach and the experiment for H-shaped encased specimen C2. | 58 |

| | |
|--|----|
| Figure 5.5: Axial load and strain response from the present analysis approach and the experiment for I-shaped encased specimen C4..... | 59 |
| Figure 5.6: Axial load and strain response from the present analysis approach and the experiment for Cross-shaped encased specimen C8..... | 59 |
| Figure 5.7: Axial load and strain responses of each composite component of specimen C1 obtained by the present analysis approach..... | 60 |
| Figure 5.8: Axial load and strain responses corresponding to variation of stirrup spacing and B/kL ratio of (a) square concrete encased H-shaped steel columns, (b) rectangular concrete encased I-shaped steel columns..... | 64 |
| Figure 5.9: Axial load and strain responses corresponding to variation of concrete strength and B/kL ratio of (a) square concrete encased H-shaped steel columns, (b) rectangular concrete encased I-shaped steel columns..... | 65 |
| Figure 5.10: Axial load and strain responses corresponding to variation of structural steel yield stress and B/kL ratio of (a) square concrete encased H-shaped steel columns, (b) rectangular concrete encased I-shaped steel columns..... | 66 |
| Figure 6.1: Force and deformations in pin-ended beam-column model with initial imperfection..... | 71 |
| Figure 6.2: Flowchart for determining axial load and deflection responses of concrete encased steel composite beam-columns..... | 78 |
| Figure 6.3: Cross-section configurations of concrete encased steel beam-columns... | 81 |
| Figure 6.4: Comparison between numerical and experimental nonlinear load-deflection response for specimen BC4. | 83 |
| Figure 6.5: Comparison between numerical and experimental nonlinear load-deflection response for specimen BC5. | 84 |
| Figure 6.6: Effects of eccentricity and column effective length on nonlinear load and deflection responses. | 89 |
| Figure 6.7: Effects of column effective length on force and moment interaction diagrams..... | 89 |
| Figure 6.8: Effects of eccentricity and column effective length on axial force..... | 90 |
| Figure 6.9: Effects of eccentricity and column effective length on bending moment. | 90 |
| Figure 6.10: Effects of concrete strength and column effective length on nonlinear load and deflection responses. | 92 |

| | |
|--|-----|
| Figure 6.11: Effects of concrete strength on force and moment interaction diagrams..... | 92 |
| Figure 6.12: Effects of concrete strength on axial force and eccentricity curves. | 93 |
| Figure 6.13: Effects of concrete strength on moment and eccentricity curves..... | 93 |
| Figure 6.14: Effects of steel strength and column effective length on nonlinear load and deflection responses. | 94 |
| Figure 6.15: Effects of steel strength on force and moment interaction diagrams. | 95 |
| Figure 6.16: Effects of steel strength on axial force and eccentricity curves. | 95 |
| Figure 6.17: Effects of steel strength on moment and eccentricity curves. | 96 |
| | |
| Figure 7.1: Simplified yield surface by piecewise linear yield hyperplanes. | 103 |
| Figure 7.2: Types of piecewise linear yield hyperplanes..... | 104 |
| Figure 7.3: Hardening rules (a) Koiter's noninteracting hardening, (b) Prager's kinematic hardening, (c) Isotropic hardening. | 106 |
| Figure 7.4: Hexagonal piecewise linear yield surface. | 107 |
| Figure 7.5: Piecewise linear (a) hexagonal yield surface (b) softening law for plane j | 109 |
| Figure 7.6: Piecewise linear (a) hexagonal yield surface (b) perfectly plastic law for plane j | 110 |
| Figure 7.7: Piecewise linear yield surface for CES section..... | 112 |
| Figure 7.8: Piecewise linear softening rule for CES section. | 113 |
| Figure 7.9: Key parameters of piecewise linear yield surface for CES section..... | 114 |
| Figure 7.10: Key parameters of piecewise linear softening rule for CES section. ... | 116 |
| Figure 7.11: Load and axial shortening response from the present analysis and the experiment for H-shaped encased column specimen C2. | 120 |
| Figure 7.12: Load and axial shortening response from the present analysis and the experiment for I-shaped encased column specimen C4..... | 120 |
| Figure 7.13: Load and lateral deflection response from the present analysis and the experiment for H-shaped encased beam-column specimen BC4..... | 121 |
| Figure 7.14: Load and lateral deflection response from the present analysis and the experiment for H-shaped encased beam-column specimen BC5..... | 121 |

| | |
|--|-----|
| Figure 7.15: Example 1: Three-bay, two-story rigid frame..... | 123 |
| Figure 7.16: Example 1: Responses of CES composite structures..... | 124 |
| Figure 7.17: Examples 1: Hinge developments (● denotes hinge on perfectly plastic or 1st softening branch; ■, ♦ denote respectively hinge on 2nd, 3rd softening branch). | 125 |
| Figure 7.18: Examples 2: Five-bay, five-story rigid frame. | 127 |
| Figure 7.19: Examples 2: Responses of CES composite structures. | 128 |
| Figure 7.20: Examples 2: Hinge developments (● denotes hinge on perfectly plastic or 1st softening branch; ■, ♦ denote respectively hinge on 2nd, 3rd softening branch; and ○ denotes unloading hinge). | 129 |
| Figure 7.21: Examples 3: Three-bay, twelve-story rigid frame..... | 131 |
| Figure 7.22: Examples 3: Hinge developments (● denotes hinge on perfectly plastic or 1st softening branch; ■, ♦ denote respectively hinge on 2nd, 3rd softening branch; and ○ denotes unloading hinge)..... | 133 |
| Figure 7.23: Examples 3: Responses of CES composite structures. | 134 |
| Figure 7.24: Examples 4: Inverted V-bracing. | 137 |
| Figure 7.25: Examples 4: Eccentrically Inverted V-bracing. | 138 |
| Figure 7.26: Examples 4: Mega X-bracing..... | 138 |
| Figure 7.27: Examples 4: Responses of CES structures before and after retrofitting. | 140 |
| Figure 7.28: Examples 4: Hinge formations at peak load (● denotes hinge on perfectly plastic)..... | 140 |
| Figure 7.29: Examples 5: Inverted V-bracing. | 141 |
| Figure 7.30: Examples 5: V-bracing..... | 142 |
| Figure 7.31: Examples 5: X-bracing..... | 142 |
| Figure 7.32: Examples 5: Responses of CES structures before and after retrofitting. | 143 |
| Figure 7.33: Examples 5: Hinge formations at peak load (● denotes hinge on perfectly plastic or 1st softening branch)..... | 143 |
| Figure 7.34: Examples 6: (a) Inverted V-bracing, (b) X-bracing. | 145 |
| Figure 7.35: Examples 6: Mega X-bracing..... | 146 |

Figure 7.36: Examples 6: Responses of CES structures before and after retrofitting. 147

Figure 7.37: Examples 6: Hinge developments (● denotes hinge on perfectly plastic or 1st softening branch; ■, ◆ denote respectively hinge on 2nd, 3rd softening branch; and ○ denotes unloading hinge). 148



CHAPTER 1

INTRODUCTION

1.1 Concrete Encased Steel (CES) Structures

The earliest composite construction consisted of structural steel beams and reinforced concrete slabs, with shear connectors in between. The system called the composite floor system, first developed for bridge construction, was readily adopted to buildings. Its phenomenal success inspired engineers to develop composite building systems by combining structural steel and reinforced concrete in a variety of vertical building systems. The composite column has gained its popularity mainly for high-rise building design due to its high rigidity, stiffness, strength, and speed of construction. Studies in North America indicate that composite columns are four or five times less expensive than a pure steel column. There are three types of composite columns mentioned in European code, i.e. concrete encased steel sections, partially concrete encased steel sections, and concrete filled steel hollow sections. Particularly, the concrete encased steel section has high fire resistance comparing to the partially encased section, concrete filled hollow section, and the conventional steel section.

Composite frame systems which contain both steel and reinforced concrete structural elements have been widely chosen for construction solutions and typically for high-rise buildings due to their stronger, stiffer, and more ductile frames than those provided by conventional pure steel or reinforced concrete structures. However, the numerical analysis approach for such composite structures has not yet kept up well with their practical applications. Some specifications still refer the engineers to

the analysis procedures mentioned in the pure steel specifications with little explicit guidance to include all the necessary effects. Many researchers in the past tried to use a full 3D FEM to trace the complete responses of such composite structures, although it is not practical to model the whole high-rise buildings with such computational approach. Some proposed a hybrid modeling which combined numerical approaches with the general FEM so as to decrease the computational effort and time. However, there is still less simplified numerical approach to analyze and capture the complete performance of CES structures with practical application.

1.2 Motivation

The present study proposes a simple inelastic fiber element based analysis approach (i.e. without complicated, time-consuming FEA) to efficiently map out the complete responses of stub and slender CES columns and beam-columns. The maximum strength capacity of the columns can be obtained as a by-product. The computational time is highly efficient and instantaneous, whilst the full 3D solid composite model probably takes much more significant time and might not find the converged solution. In essence, the proposed scheme realistically accommodates the simultaneous influences of concrete confinement associated with structural steel and reinforcement bars, buckling of the reinforcement bars, local buckling of the structural steel, and initial geometric imperfection of the composite columns. Once the behaviors of the structural elements are well-simulated, the full 3D structural modeling and analysis can then be simplified to a simple frame-based analysis. Piecewise linear yield hyper-planes are proposed to incorporate into the geometrically nonlinear analysis to simulate the complete performance of CES structures (i.e.

elastic, maximum load capacity, post-peak softening response). Full structural response including its softening behavior plays a very important role for the optimization of practical structural strengthening. Various common steel bracing systems are chosen to enhance the structural performance of CES composite structures. The effects of different bracing configurations are investigated and compared in terms of load and lateral displacement response for optimal design of steel bracing systems.

1.3 Research Objectives and Scopes

Main purposes of this study are as briefly described as follows:

1. Develop a non-linear inelastic analysis approach to investigate the behaviors of the CES columns and beam-columns.
2. Take into account the effects of material nonlinearity, geometric imperfection, geometry nonlinearity, conventional concrete confinements and highly confinement, local buckling of structural steel, buckling of reinforcement bar, and slenderness.
3. Conduct sensitive parametric analyzes to study various effects on the behaviors of CES columns and beam-columns.
4. Propose the piecewise linear yield hyper-planes for combined stress model to capture the post-peak softening of CES columns.
5. Trace the full spectrum of force and displacement responses of CES structures using nonlinear 2nd order analysis (both geometry and material nonlinearity).
6. Compare the efficiency of different bracing systems on the overall responses of CES structures in a sense of structural strengthening.

7. Recommend guidelines for analyzing and strengthening CES structures.

1.4 Research Methodology

Below are the procedures to achieve the mentioned objectives and scopes:

1. Develop an efficient numerical method to rapidly converge the solutions of nonlinear inelastic analyzes.
2. Develop a nonlinear inelastic fiber analysis method to map out the complete structural responses of the CES columns and beam-columns, i.e. axial load and strain response, load and deflection response, axial force-bending moment interaction diagram, moment-curvature diagram, and maximum load-carrying capacity.
3. Validate the proposed approach by comparing the analysis results with the previous experimental tests and researches.
4. Use the validated approach to study various effects on the behaviors of CES columns and beam-columns.
5. Propose a novel piecewise linear yield model with an associated softening rule and derive the mathematical relationships for the proposed combined stress model (viz. post-peak softening of CES columns).
6. Verify the proposed piecewise linear yield hyper-planes with available experimental tests.
7. Generate necessary responses of CES columns for the analysis of CES structures.
8. Perform nonlinear 2nd order analysis (both geometry and material nonlinearity) of CES structures for full spectrum of force and displacement responses.

9. Adopt common types of bracing systems to strengthen the overall responses of CES structures, and investigate their efficiency on CES structural performance.
10. Draw conclusions and recommend guidelines for analyzing and strengthening CES structures.

1.5 Layout of the Thesis

The current research presents nonlinear inelastic analyses of concrete encased steel structures using the simplified numerical analysis and mathematical programming approaches. The thesis is composed of eight chapters with a brief contextual introduction and concluding remarks for each corresponding chapter.

Chapter 1 gives an overview of concrete encased steel structures and whole research study. Chapter 2 describes literature reviews of previous experimental studies and nonlinear analysis approaches concerning with CES columns, beam-columns, composite frames, and structural bracing systems.

Chapter 3 provides a short description of material models used in previous researches, and detailed discussion of the constitutive models used in the current study. Particularly for concrete materials under compression, three different stress-strain curves are used simultaneously to account for different levels of concrete confinement (i.e. unconfined concrete, partially confined concrete, and highly confined concrete). Local buckling of structural steel and buckling of reinforcement bars after the crushing of concrete are simulated using their mechanical material constitutive laws, respectively. The determination of confinement zones for different steel cross-section, i.e. H, I, and cross shapes, has been recommended. Chapter 4

presents the nonlinear inelastic analysis of CES sections based on fiber element analysis. Assumptions and methods of composite sectional discretization are described. And the procedures to determine the strain and curvature relationships as well as the stress resultants are provided.

Chapter 5 presents the detailed step-by-step algorithms for tracing the full structural responses, i.e. load and axial strain curves, of CES columns under pure axial compression with initial geometric imperfection. An adaptive initial condition technique is proposed to cooperate with numerical approach to efficiently converge the solutions. Relevant experimental tests are summarized and compared to validate the proposed numerical approach (i.e. ultimate capacity, load and axial strain response). Key parameters such as concrete compressive strength, steel yield stress, spacing of lateral ties, and structural steel shapes have been extensively investigated and discussed. Chapter 6 extends the numerical approach to simulate the complete load and lateral displacement of the beam-columns under eccentric load. Step-by-step computational approach is outlined and explained. Relevant experimental results are summarized and validated against the analysis results (i.e. ultimate capacity, load and lateral displacement curve). Nonlinear interaction diagrams with different slenderness effects are also presented. Parametric sensitivity analyses have been performed to study the effect of eccentricity ratio, concrete compressive strength, and steel yield stress with different effective length ratios.

Chapter 7 aims to assess the performance of CES structures by tracing the full load and displacement response using nonlinear second order analysis (i.e. both material and geometric nonlinearity). Piecewise linear yield hyper-planes are proposed to activate the softening response of CES structures. Mathematical

programming tools, which are used with the proposed yield function, are briefly described. The proposed piecewise linear yield function is validated against relevant experimental tests. Common steel bracing systems have been used to strengthen the performance of existing CES structures with the sense of optimal design.

Chapter 8 concludes the whole study of the thesis and gives useful recommendations on the behavior (i.e. ultimate capacity, ductility, and post-peak softening) of CES structures as well as the efficiency of steel bracing systems. Potential future studies have been briefly outlined at the end.



CHAPTER 2

LITERATURE REVIEW

2.1 Introduction

The behavior of concrete encased steel composite structures has been an interesting topic of research for many years. Many full-scale experimental tests of concrete encased steel columns and beam-columns have been carried out since the last five decades all around the world. Analysis approaches including numerical methods, analytical models, finite element simulations, and design codes have been developed to explore the hidden behaviors of CES structures as well as to justify the safety for practical design purpose. The responses of such structures are influenced by many parameters such as the concrete compressive strength, steel and reinforcement bar yield stress, steel configuration, confinements from structural steel and reinforcement bars, slenderness ratios, and boundary conditions (supports and loadings). Although experimental studies can be carried out to investigate the behavior of CES columns and beam-columns, they are very expensive and time consuming to test for all variations of key parameters. Experiments should be used for validation of analysis approaches, not to derive the theory (Liang 2009). Therefore, the nonlinear inelastic analysis of CES columns and beam-columns play important roles to compensate the drawbacks of expensive, controlled conditions, and limited numbers of experimental tests.

This chapter reviews some key experimental studies and nonlinear analysis approaches of CES columns, beam-columns, and composite frames. Structural steel

bracing systems and their effects on the structural performance are also briefly reviewed.

2.2 Concrete Encased Steel Columns and Beam-Columns

2.2.1 Experimental Studies

Various experimental tests were carried out to investigate the behavior and to approximate the maximum strength capacity of the concrete encased steel composite columns. Abundant experimental studies investigate the influences of various physical and material parameters (i.e. steel cross-sectional shape, steel and concrete strength, slenderness ratio, steel-to-concrete ratio and loading condition) on the intrinsic behaviors of the concrete encased steel composite columns.

The committee of Structural Stability Research Council (SSRC Fourth Quarter 1979) issued a report regarding the recommended design rules and discussion of the behavior of the composite column along with experimental tests. The council recognized that the composite steel-concrete compression members exhibited the behavior almost the same as steel columns if the strength and stiffness of the plain steel alone were several times greater than those of the structural concrete. And if the strength and stiffness of the structural concrete alone were significantly greater than those of the structural steel, the composite steel-concrete compression members would behave more or less the same as the normal reinforced concrete compression members. However, in order that the steel-concrete columns are considered as the composite steel-concrete columns, the quantity of the structural steel must comprise at least 4 percent of the total composite column cross section.

The strength and load-deflection behaviors of biaxially loaded steel reinforced concrete columns were studied experimentally and theoretically by Morino et al. (1984). Forty column specimens were tested by grouping into four main groups according to the slenderness ratio computed for the gross section of the concrete column, and varied the angles of rotation of the eccentricity. It was concluded that the maximum capacity of short columns was controlled by the crushing of concrete material, and the load-deflection curve exhibited a very sharp peak. Unlike for the case of slender columns, the maximum load carrying capacity is obtained when the stiffness of the columns becomes zero. The behavior of the concrete encased steel composite columns with different stiffnesses in both directions subjected to the biaxially eccentric compression is the same as those subjected to the uniaxial bending in the final state. This behavior occurs because only the deflection about the weak axis keeps increasing in the large deflection range, while the deflection about the strong axis stops increasing and in some cases even decreases due to the P-Delta effect.

Sixteen physical experimental tests of composite steel-concrete beam-columns were carried out by Mirza et al. (1996). Three series of specimens with different bonding conditions of steel rib connectors welded to the flanges were loaded to failure. The first series were employed with steel ribs having holes of 27 mm in diameter spaced at 50 mm center-to-center, and bonding was allowed between ribs and concrete. The second series were made with the same steel ribs but without holes, and bonding condition was still allowed. The last series of specimens were chosen exactly the same as the first series except that no bonding between the steel ribs and the surrounding concrete was allowed. The unbonding conditions were achieved by

covering the holes with wooden disks and the steel rib surfaces were covered by smooth plastic tape coated with a layer of oil. Three main objectives of this experimental study were to investigate the behavior and ultimate strength of CES beam-columns whose second-order effects are significant, to examine the effects of different bonding conditions between the steel rib connectors and concrete, and to validate the ACI 318-95, Eurocode 4, and proposed nonlinear numerical simulation using finite element software ABAQUS. The observations from these physical tests concluded that the bonding conditions at the surface contacts between the steel ribs and concrete had a small effect on the ultimate strength of CES beam-columns. The design codes, both and AIC 318-95 and Eurocode 4, safely predict the ultimate capacity of such composite beam-columns. Also, the main assumption used in ACI 318-95 that the maximum compressive strain at the extreme fiber of value 0.003 was valid for such type of CES beam-columns.

Chen and Yeh (1996), and Tsai et al. (1996) performed three series of tests for concrete encased steel composite stub columns of 1.2m height having three shapes of structural steel section, i.e. I-, H-, and Cross-shaped sections. The tests from Chen and Yeh (1996) consisted of square concrete sections encasing three specimens of H-150 x 150 x 7 x 10, three specimens of Cross (Two H)-150 x 90 x 5 x 8, and four specimens of I-150 x 75 x 5 x 7. And the tests from Tsai et al. (1996) were conducted for square concrete sections encasing four specimens of Cross (Two H)- 150 x 90 x 5 x 8, and six specimens of Cross (Two H)- 160 x 50 x 3.2 x 4.5. Both ultimate strength and behavior of axially loaded CES stub columns were investigated.

Another set of full-scale column tests was conducted by Al-Shahari et al. (2003) to investigate the behavior of eccentric lightweight aggregate concrete encased

steel composite columns and to verify the application validity of such concrete type in composite structure. Two codes of design practice were used to check the adequacy of their design application – AISC-LRFD and BS 5400. Sixteen full-scaled composite columns were pin ended and subjected to uniaxial bending about their major axis. In his study, the column height varied from two to three meters with equal end eccentricities of the applied load at both ends. It is observed from the testing that the failure mode of all the composite columns was the crushing of concrete on the compressive side with some cracking on the tensile side of the column. The damage of concrete can be noticed at the loading stage of more than 95% of the failure load in all tests. It is found that the effect of steel ratio on the capacity of the concrete encased steel composite column was very significant, where the increase of steel ratio of only 2% would result the increase of load carrying capacity about 40% to 47%. However, the effect of steel ratio did not introduce any significant effect on the lateral deflection of the columns whenever the steel ratio was in the range from 4% to 6%. It is observed that the lateral deflection was very small at the low loading stage, and started to increase significantly the applied load from 20% to 30% of the failure load. And the effect of the column length on the load capacity was very small by comparing between the columns of 2m and 3m in the experiments. It was concluded from the experimental study that the application of the lightweight concrete in the concrete encased steel composite columns increases the load carrying capacity of the steel sections significantly, but at the same time decreases its ductility also. Furthermore, it induced less lateral deflection than those from the normal concrete composite columns.

Eight full-scale slender high-strength concrete encased steel composite columns were tested under axial load with and without eccentricity by Zhao et al. (2005). The strength of concrete was selected in the range between 43.3 MPa to 67 MPa. Six specimens were axially loaded while two specimens were loaded with eccentricities of 30mm and 40mm. The tests were set up mainly based on two motivations. Firstly, the increase of high-strength concrete used in high-rise building made the current design trend lean toward more slender column designs. Therefore, the real performance of slender high-strength CES columns posted a major concern for practical design engineers. Secondly, most previous tests were mainly carried out for stub CES columns of low and normal strength concrete under axial load only. Only a few experimental studies had full-scale test of slender CES columns of high-strength concrete with eccentric loading while the complete behavior of such CES columns have not been fully understood yet. For specimen subjected to axial load, it was observed that all columns failed due to the crushing of concrete cover at the column mid-height, and no sign of tensile cracks or concrete spalling were observed before reaching the ultimate load. For specimens loaded with eccentricity, the tensile cracks were noticed when applied loading reached 90% of the maximum capacity. Similarly, the beam-columns failed due to the spalling of concrete at the column mid-height.

The extensive experimental test summary and reviews of steel-concrete composite structures can be found in the works of Shanmugam and Lakshmi (2001), Weng and Yen (2002), and Kim (2005). These experimental tests extensively covered various steel cross-sectional shapes, steel and concrete strengths, slenderness ratios,

steel-to-concrete ratio, and loading conditions of the concrete encased steel composite columns and beam-columns.

2.2.2 Nonlinear Analysis Approaches

Taking advantages of the available experimental data, many numerical models have been developed, i.e. Kato (1996), El-Tawil and Deierlein (1999), Wang (1999), Zhao et al. (2005), Chen and Lin (2006), Weng et al. (2007). Some of them took into account the concrete confinement given by reinforcement bars, yet many of them still neglected the confinement associated with structural steel leading to underestimation of the maximum load carrying capacity of the columns (Li et al. 2003). Recently, the high confinement was accounted in the fiber analysis program (CSRAP-Flex) by Zhou and Attard (2013) to predict the nonlinear behavior of damaged concrete encased steel girders. However, the constitutive model for confined concrete used in the analysis was from reinforcement bars only. Chen and Lin (2006) proposed an analysis approach to approximate the maximum strength and behavior of the concrete encased steel composite columns that incorporate the effects of concrete confinement from both conventional reinforcement bars and structural steel. However, such approach only considers the behavior of the axially-loaded stub columns, which eliminate the vital influences from member slenderness and bending moment. Three different levels of the concrete confinement (namely unconfined, partially confined and highly confined) are illustrated in Figure 2.1.

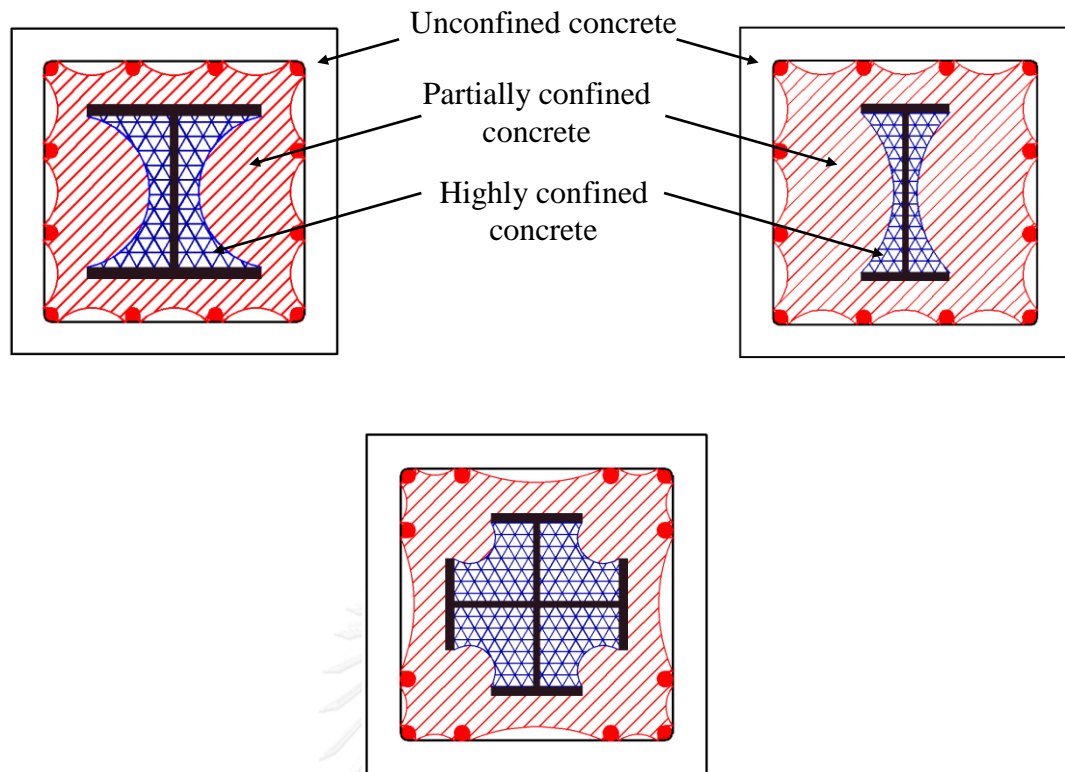


Figure 2.1: Unconfined, partially confined, highly confined concrete for encased H-shaped, I-shaped, and Cross-shaped steel composite sections.

Fiber element approach was implemented to investigate the behavior of stocky and slender concrete encased composite columns under the combined axial and flexural forces, i.e. El-Tawil et al. (1995), El-Tawil and Deierlein (1999), Chen et al. (2001), Spacone and El-Tawil (2004), and Weng et al. (2007). However, none of these studies have yet incorporated the high confinement of concrete encasing the structural steel member. Ellobody and Young (2011) adopted a commercial software, called ABAQUS, to simulate the response of concrete encased steel composite columns using the sophisticated 3D solid elements. Still, the model discretized the concrete into the three different (viz. unconfined, partially confined, and highly confined concrete) confinement areas. Such a full 3D FEM is generally very expensive, time-consuming, and error-prone during the modeling process. Thus,

Wang et al. (2013) recently proposed a steel-concrete composite fiber beam-column model to simplify the modeling procedures compared to the tradition 3D FEM. Yet, a user-defined material subprogram UMAT in ABAQUS was still needed.

2.3 Steel–Concrete Composite Frames

Many nonlinear analysis approaches have been developed to fully capture the complete response of steel-concrete composite frames. Elnashai and Broderick (1996) used the nonlinear dynamic analysis to investigate the seismic response of moment-resisting composite frames and discussed the adjustments that should be made to improve the design code. It was concluded that the Eurocode 8 for the composite frames was excessively conservative and recommendations should be suggested. The program ADAPTIC was used to perform a series of nonlinear dynamic analyses with different ground motions. Thermou et al. (2004) discussed the seismic design and performance of the European design codes, i.e. Eurocode 4 (Design of Composite Steel and Concrete Structures), and Eurocode 8 (Design of Structures for Earthquake Resistance). The inelastic static pushover analysis was used to trace the full response of the composite frames. Two groups of frames were designed, a composite slab for the first group and a solid concrete slab for the second group. The finite element program INDYAS was used for the nonlinear inelastic analysis phase where the top displacement versus the base shear responses were plotted. Several clauses in the Eurocode 4 were suggested for improvement or even correction, and more importantly, the clauses related to the lateral-torsional buckling check criteria for composite beams. Similarly, Elghazouli et al. (2008) employed a simplified nonlinear static loading approaches to examine the seismic performance of composite steel-

concrete moment-resisting frames. The nonlinear finite element program ADAPTIC, which accounted for material and geometric nonlinearities, was utilized in accordance with the provisions of the European seismic code, Eurocode 8.

In addition to the frame-based analysis approaches, Wang et al. (2009), Han et al. (2011), Li et al. (2011), and Li et al. (2012) tried to investigate the composite frames using the full 3D FEM simulation although it is not practical to model the whole high-rise buildings with such computational approach.

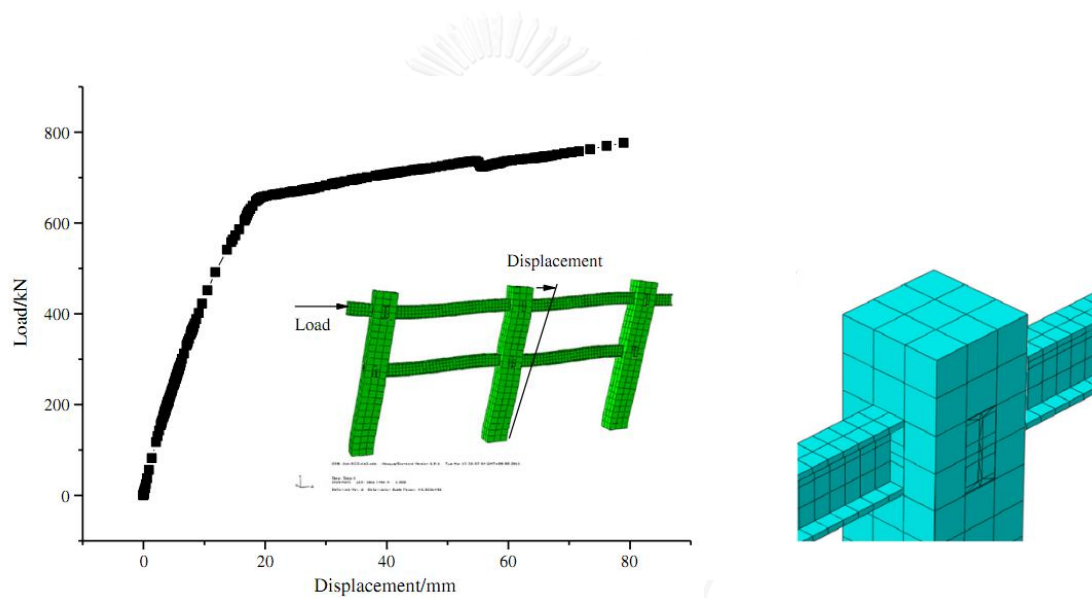


Figure 2.2: A Load and displacement response of composite frame, and beam-column joint by FEM (Li et al. 2012).

Wang et al. (2013) proposed a hybrid numerical modeling which combined the fiber beam-column model with the general FEM software “ABAQUS” in order to decrease the computational effort and time. There are some applications of the fiber element method with plastic hinge ranging from complex to simple approaches to analyze the composite frames, such as Iu et al. (2009), Liu et al. (2012), Chiorean (2013), and Tenchini et al. (2014). However, there are still less numerical approach to

analyze and capture the performance of CES composite frames with practical application.

2.4 Structural Bracing Systems

Lateral drift due to wind or seismic loadings causes a major concern in the design of tall buildings. The provision of adequate lateral stiffness to satisfy the serviceability limit states must be carefully considered. There are various structural systems to control the lateral drift, one of the most common and efficient solutions is to provide the structural braces. The common bracing configurations for braced frames are shown in Figure 2.3 (Taranath 2011).

Kameshki and Saka (2001) presented a genetic algorithm to optimize the design of three-bay, fifteen-story steel buildings with different types of bracing systems, i.e. X, V, and Z bracings. The design conformed to both serviceability and strength criteria from BS 5950 (1990), where lateral torsional buckling was also taken into account for beam-columns. Pinned and fixed support conditions were examined. It was concluded that the X-bracing produced the lightest frame among the three in both support conditions, whereas the Z-bracing produced the heaviest frame. The V- and Z-bracings did not provide better lateral stiffness than the X-bracing system for such steel frames.

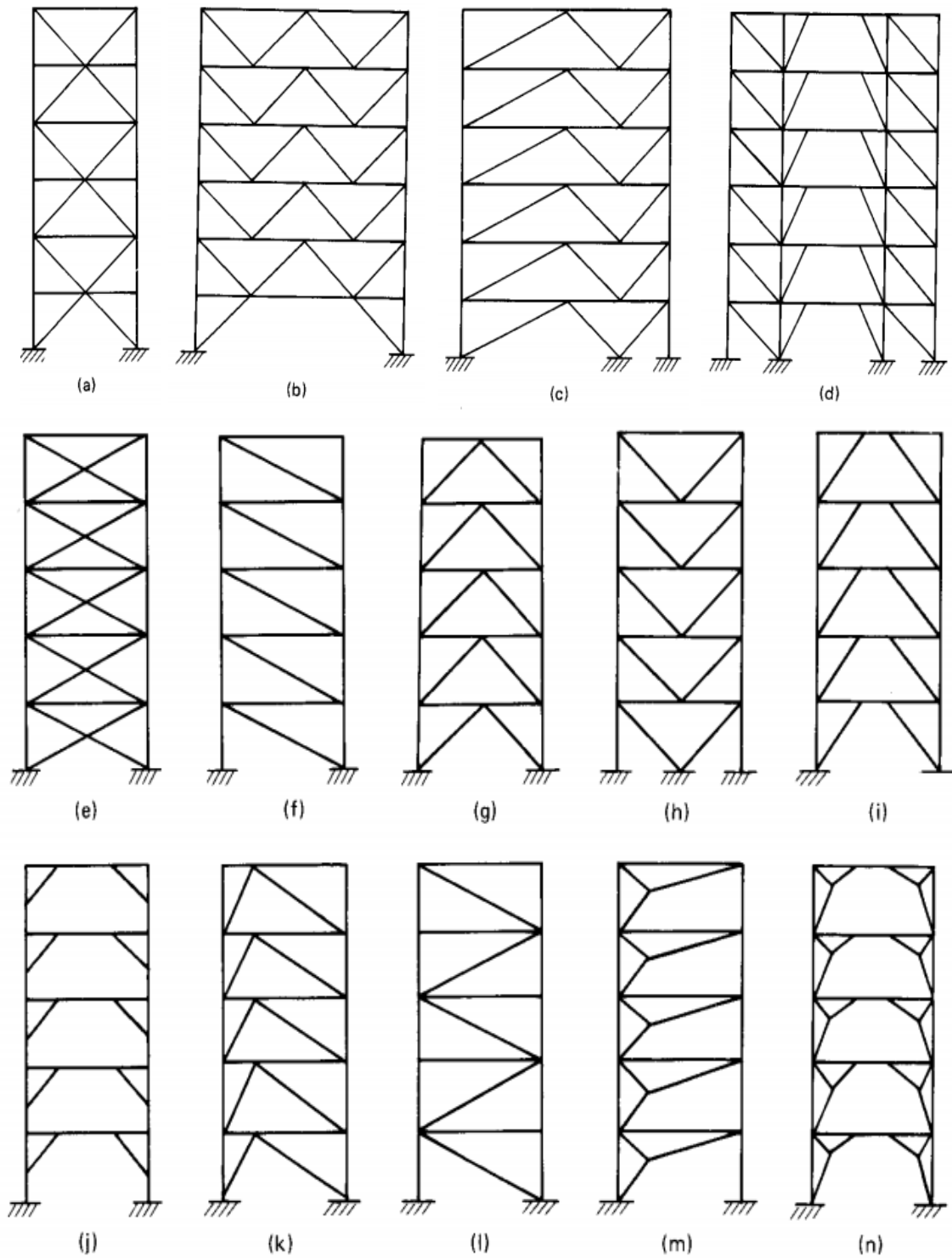


Figure 2.3: Bracing configurations (Taranath 2011).

Di Sarno and Elnashai (2009) assessed the seismic performance of steel moment-resisting frames retrofitted with different bracing systems. A five-bay, nine-story steel building was retrofitted with special concentrically braces, buckling-restrained braces, and mega-braces. Inelastic time-history analyses were employed to assess the performance of steel frames under earthquake ground motions. A general finite element 2D program DRAIN-2DX was used to carry out the elastic and inelastic (static and dynamic) analyses. The results of the nonlinear inelastic analyses concluded that the mega-braces was the most cost-effective bracing systems. The maximum lateral drift in mega-braces was lower than the special concentrically braces between 45% to 55%, and also the total steel weight was 20% lower.

Türker and Bayraktar (2011) conducted both experimental and numerical investigations of the effects of bracing configuration on steel structures. A two-bay, three-story rectangular steel building was constructed with 1/2 scale of a real building for experimental tests. Four different types of bracings, i.e. X-type, V-type, Inverted V-type, and K-type were applied to the structure for investigations. Finite element models were developed using SAP2000 to carry out the modal analyses and compared to the experimental test results. The study showed that the numerical results were larger than the experimental results in all cases, thus the finite element model needed to be adjusted. Among the four bracing configurations, the X-type provided the highest stiffness to the steel buildings in both the experimental tests and numerical analyses.

Tsai (2012) proposed a performance-based design approach for retrofitting regular building frames with steel braces against sudden column loss. The design approach was developed from the pseudo-static analysis and was validated with

incremental dynamic analysis from the general purpose finite element program SAP2000. The concept of the retrofit design algorithm was to provide adequate steel braces to compensate the sudden loss of column resistance.

Four full-scale experimental tests of steel frames with y-bracings of different geometries and cross-sections were conducted by Majid Zamani et al. (2012). The y-bracing consisted of three members connected in y-shaped geometry; it was used to provide adequate openings to the braced bays. The full-scale specimens were applied with quasi-static cyclic loading until yielding and failure occurred. The performance of these frames was compared with nonlinear static push-over analyses using software program ABAQUS. It was concluded that the performance of the y-bracing and X-bracing was comparable, and the seismic design of two-bay with y-braced frames could be made with the same assumptions of X-braced frames. The buckling resistance of y-braced frames could be increased by locating the convergence point towards the center. The benefits of using y-bracing system were highly desirable in terms of practical viewpoints.

In addition to the experimental tests of steel bracing systems, more experimental studies concerning with seismic performance of buckling restrained braced frame systems can be found from the works of Huang et al. (2000), Fahnstock et al. (2003), and Mahin et al. (2004).

CHAPTER 3

CONSTITUTIVE MODELS OF MATERIALS

3.1 Introduction

The material constitutive relationship acts as the backbone for the nonlinear inelastic analyses. The modeling of concrete including the confinement effects is very essential for both strength and ductility of the concrete encased steel composite columns. CES composite member consists of concrete, structural steel, and reinforcement bars. Sanz Picon (1992) investigated the behavior of composite column cross sections under biaxial bending by using the confined concrete model from Kent and Park (1971), and steel model of elastic plastic with nonlinear strain hardening. Similarly, Mirza and Skrabek (1992) adopted the concrete model from the modified Park et al. (1982) with three regions of confinement, and steel model of elastic plastic with nonlinear strain hardening to perform the statistical analysis of slender composite beam-column strength. For concrete model, confinement from reinforcement bars is usually included by using a well-known confinement model from Mander et al. (1988). However, the confinement in the model of Mander et al. (1988) considers only the influences from the longitudinal and transverse reinforcement bars. When this model is applied to the concrete encased steel composite columns, it will underestimate the confinement which comes from the structural steel section which is known as the highly confinement to the concrete. Li et al. (2003) studied the behavior of the steel encased reinforced concrete beam-column under seismic loading without considering the confinement effect from the structural steel section. And they concluded that one of the reasons why their analysis underestimated the ultimate

strength was because they did not include the confinement effect from the structural steel section in their analysis. Chen and Lin (2006) predicted the axial load carrying capacity and the behavior of the concrete encased steel composite stub column by taking into account the confinement effects from both the reinforcement bars and the structural steel shapes. They replaced the maximum compressive confined concrete by multiplying the maximum compressive unconfined concrete strength with the confinement factors – partially confined factor and highly confined factor.

3.2 Concrete

3.2.1 Concrete in Compression

The confinement in CES section comes from many factors. The confinement from lateral ties and longitudinal reinforcement bars are known as the partially confinement. Figure 3.1 shows the stress-strain relationship of unconfined and confined concrete. This effect can be modeled using a widely accepted stress-strain curve from Mander et al. (1988) as:

$$f_c = \frac{f'_{cc} x^r}{r - 1 + x^r} \quad (3.1)$$

where f'_{cc} is the maximum compressive strength of confined concrete

$$x = \frac{\varepsilon_c}{\varepsilon_{cc}} \quad (3.2)$$

$$r = \frac{E_c}{E_c - E_{sec}} \quad (3.3)$$

where ε_c is the longitudinal compressive concrete strain; ε_{cc} is the strain corresponding to the maximum confined concrete strength; E_c is the tangent modulus of elasticity of the concrete; E_{sec} is the secant modulus of maximum confined concrete strength.

The tangent modulus of elasticity of the concrete is taken from ACI (2011):

$$E_c = 4700\sqrt{f'_{co}} \text{ MPa} \quad (3.4)$$

And the secant modulus of maximum confined concrete strength which can be expressed as:

$$E_{sec} = \frac{f'_{co}}{\varepsilon_{cc}} \quad (3.5)$$

where f'_{co} is the maximum unconfined concrete strength.

The strain at the peak confined concrete stress is given as:

$$\varepsilon_{cc} = \varepsilon_{co} \left[1 + 5 \left(\frac{f'_{cc}}{f'_{co}} - 1 \right) \right] \quad (3.6)$$

where ε_{co} is the strain corresponding to the unconfined concrete strength;

The maximum compressive strength of confined concrete due to the longitudinal and transverse reinforcement is determined by:

$$f'_{cc} = f'_{co} \left(-1.254 + 2.254 \sqrt{1 + \frac{7.94f'_l}{f'_{co}}} - 2 \frac{f'_l}{f'_{co}} \right) \quad (3.7)$$

where the confinements come from the effective lateral confining pressure from the transverse reinforcement $f'_l = k_e \rho f_{yh}$; and k_e is the confinement effectiveness coefficient which is expressed as:

$$k_e = \frac{\left(1 - \sum_{i=1}^n \left[\frac{(w'_i)^2}{6b_c d_c} \right] \right) \left(1 - \frac{s'}{2b_c}\right) \left(1 - \frac{s'}{2d_c}\right)}{(1 - \rho_{cc})} \quad (3.8)$$

depending on the effective area confined by the longitudinal reinforcement layout and the stirrup spacing.

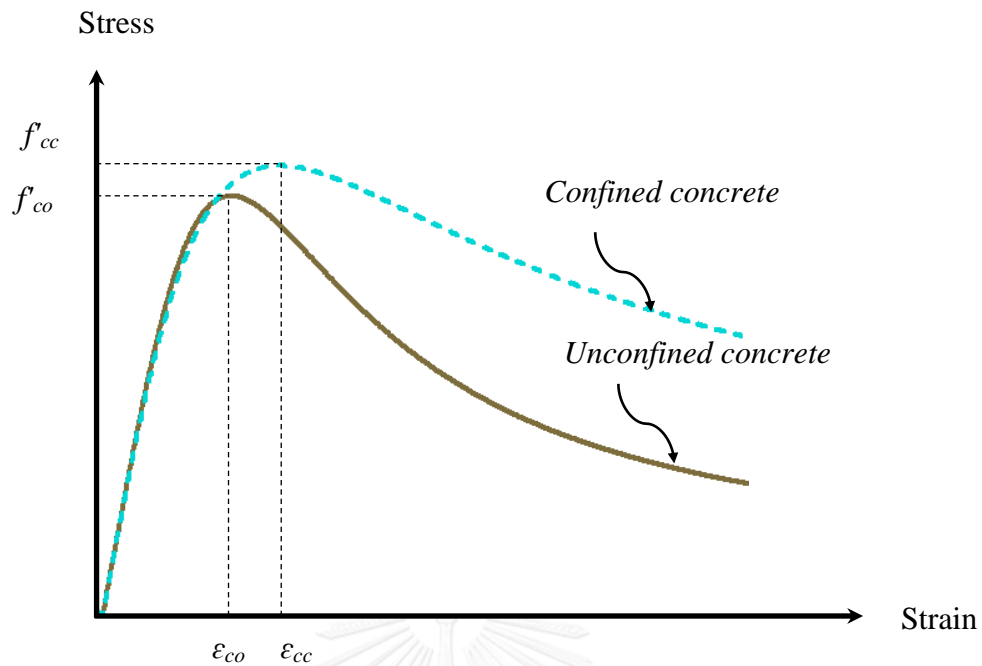


Figure 3.1: Stress-strain curves of unconfined and confined concrete (Mander et al. 1988).

The maximum compressive strength for the partially confined concrete and the highly confined concrete (Chen and Lin 2006) are respectively determined by:

$$f'_{cc.p} = K_p f'_{co} \quad (3.9)$$

$$f'_{cc.h} = K_h f'_{co} \quad (3.10)$$

where the confinement factors K_p and K_h are in the range from 1.09 to 1.5 and 1.1 to 1.97, respectively, depending on the reinforcement configurations and structural steel shapes. Figure 3.2 shows the stress-strain relationship of the unconfined, partially confined, and highly confined concrete.

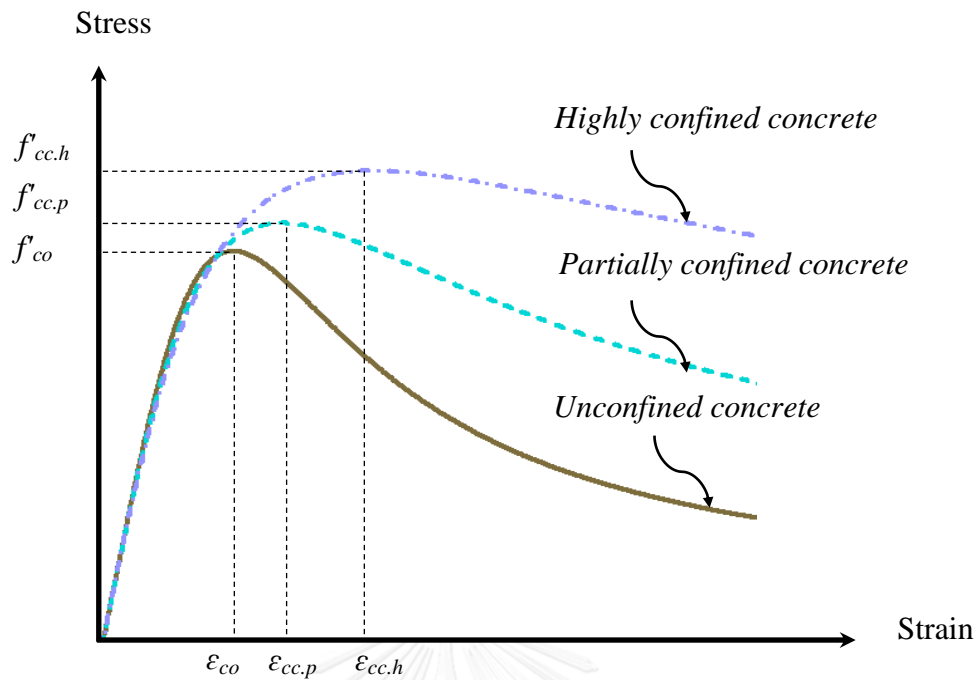


Figure 3.2: Stress-strain curves of unconfined, partially confined, and highly confined concrete.

Three different stress-strain curves for concrete in compression are defined and assigned to three different concrete zones accordingly. For the unconfined concrete zone, the stress-strain curve is determined from Equation 3.7 by setting the effective lateral confining pressure $f'_l = 0$, which makes the maximum compressive strength of confined concrete f'_{cc} equal to the maximum unconfined concrete strength f'_{co} . The maximum concrete unconfined strength is measured from the standard cylinder specimen test, which is taken equal to 0.8 of the standard cube specimen test. And the unconfined strain corresponding to the maximum unconfined strength is taken as 0.002. For the partially confined zone and the highly confined zone, the stress-strain curves are generated using the model from Mander et al. (1988) by replacing the maximum compressive strength of confined concrete f'_{cc} with the

maximum compressive strength for the partially confined concrete $f'_{cc,p}$ and the maximum compressive strength for the highly confined concrete $f'_{cc,h}$.

3.2.2 Concrete in Tension

When the slender column exhibits the initial geometry imperfection and buckles under axial load, one face of the column is in compression while the opposite face is in tension. The concrete uniaxial stress-strain curve for the concrete in tension follows the linear elastic path proportionally up to the maximum tensile strength of concrete f_{ct} which is taken as $0.6\sqrt{f'_{co}}$. The softening part of the stress-strain curve after the concrete cracking is represented by a linearly degradation down to zero when the tensile strain reaches the ultimate tensile strain of concrete ϵ_{ctu} which is taken as 10 times of the strain corresponding to the maximum tensile strength of concrete. The stress-strain relationship for the concrete in tension is shown in Figure 3.3.

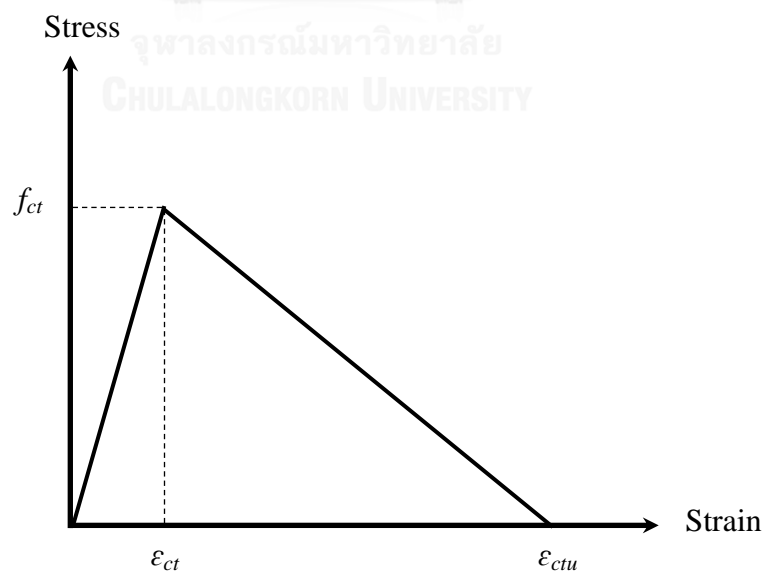


Figure 3.3: Stress-strain relationship of concrete in tension.

3.3 Structural Steel

3.3.1 Structural Steel in Compression

Generally, the stress-strain curve for structural steel is assumed to be identical when studying the behavior of the composite members under bending moment. However, for composite members subjected to compressive load, the local buckling of the structural steel is usually observed. For the concrete encased steel composite column, the local buckling of the steel is likely to occur in the flanges after the spalling of the partially confined concrete. Thus, it was suggested by Chen and Lin (2006) that the stress degradation was assumed to happen after the axial strain of the composite column pass the partially confined strain $\varepsilon_{cc,p}$ corresponding to the maximum partially confined strength $f'_{cc,p}$.

The stress-strain curve for the structural steel in compression is divided into four regions as shown in Figure 3.4. The first region was assumed initially to be linear elastic with the Young's modulus of 200GPa. The second region was kept constant up to when the axial strain reached the partially confined concrete strain $\varepsilon_{cc,p}$. The third region, which showed the degradation of the stress representing the post-buckling behavior, the strength of the structural steel is assumed to drop from the yield strength to only 20 percent of its yield strength. And fourth region was defined when the axial strain reached 2.5 times of the partially confined strain $\varepsilon_{cc,p}$, the steel strength became constant.

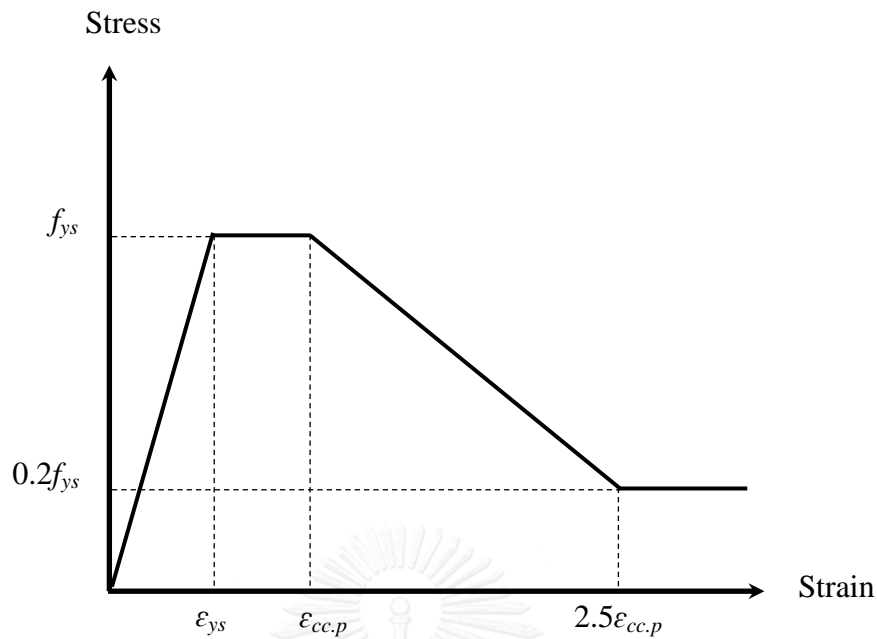


Figure 3.4: Stress-strain relationship of structural steel in compression.

3.3.2 Structural Steel in Tension

The stress-strain relationship for the structural steel in tension was chosen to take into account for the effects of strain hardening as well as the strain softening which was suggested by Holzer et al. (1975). The stress-strain curve has four distinct regions – an elastic region, a perfectly plastic region, a strain hardening region, and a strain softening region. The complete curve, as shown in Figure 3.5, can be determined from the following equations:

For elastic region ($\varepsilon_s \leq \varepsilon_y$):

$$f_s = E_s \varepsilon_s \quad (3.11)$$

where E_s is the modulus of elasticity of steel; ε_s is the strain of steel; ε_{ys} is the strain corresponding to the yield stress of steel.

For perfectly plastic region ($\varepsilon_{ys} < \varepsilon_s \leq \varepsilon_{sh}$):

$$f_s = f_{ys} \quad (3.12)$$

where f_{ys} is the yield stress of steel; ε_{sh} is the strain where the strain hardening begins depending on the area of steel.

For strain hardening and strain softening regions ($\varepsilon_{sh} < \varepsilon_s \leq \varepsilon_r$):

$$f_s = f_{ys} \left(1 + r \left(\frac{f_u}{f_{ys}} - 1 \right) e^{(1-r)} \right) \quad (3.13)$$

where

$$r = \frac{\varepsilon_s - \varepsilon_{sh}}{\varepsilon_u - \varepsilon_{sh}} \quad (3.14)$$

f_u is the maximum stress of steel; ε_r is the strain at the rupture of steel; ε_u is the strain corresponding to the maximum stress of steel.

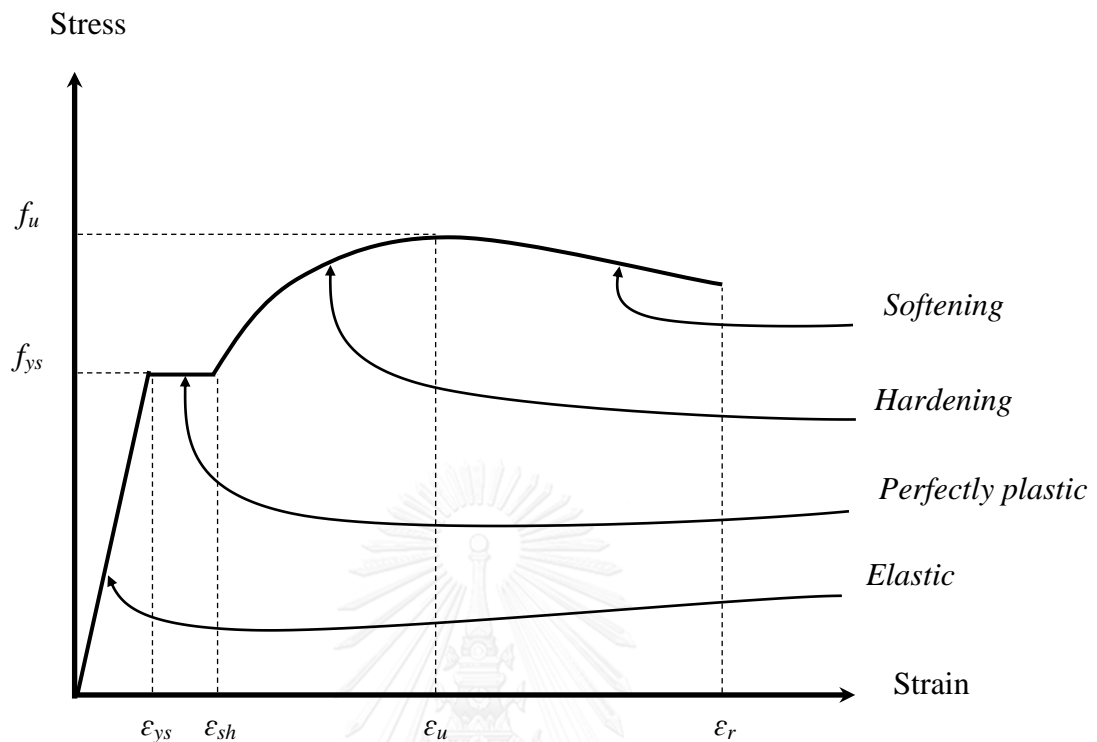


Figure 3.5: Stress-strain relationship of structural steel in tension.

3.4 Reinforcement Bar

3.4.1 Reinforcement Bar in Compression

The constitutive modeling of the reinforcement bars is assumed similarly to the structural steel with four parts. The stress-strain relationship for the reinforcement bar under compression is shown in Figure 3.6. Under compressive load, the buckling of the longitudinal rebar occurred when the its inelastic strain becomes large. And the strength and ductility of the structural members is significantly decreased after the buckling of the longitudinal bars (Chen and Lin 2006). For the composite column under compression, it is assumed that the reinforcement bars buckled at the time the unconfined concrete crushed. Thus, the stress in the rebar degraded when the axial

strain reached the unconfined concrete strain ϵ_{co} corresponding to the maximum compressive unconfined concrete strength f'_{co} . And the post-buckling strength was assumed to dropped to 20 percent of its yield strength, and became constant after the axial strain reached 2.5 times of the unconfined concrete strain ϵ_{co} .

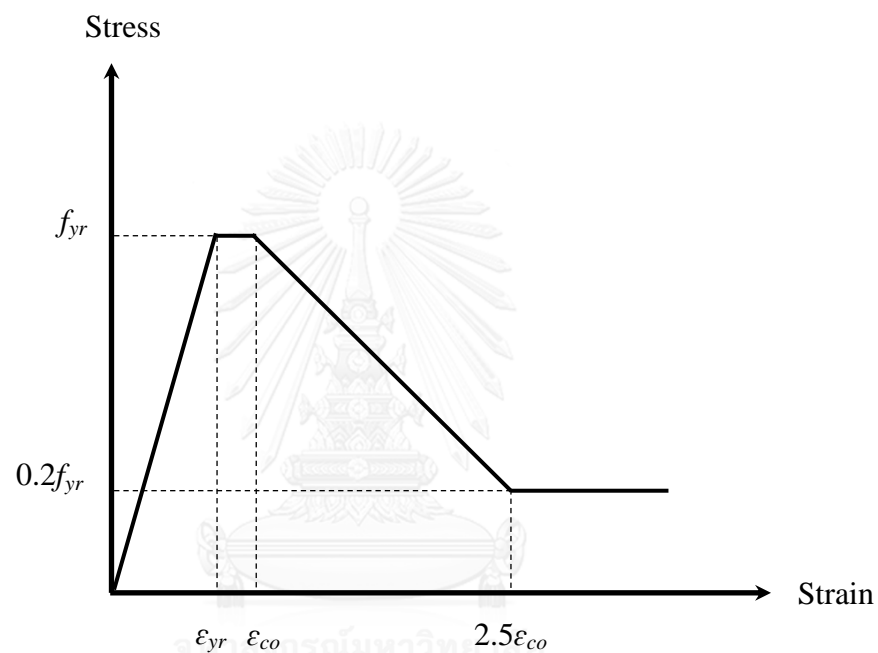


Figure 3.6: Stress-strain relationship for reinforcement bar in compression.

3.4.2 Reinforcement Bar in Tension

When the slender composite column buckles under compression load with large lateral displacement at the mid-height, the reinforcement bars in one side could buckle and the other in the opposite side are in tension. The complete stress-strain relationship of the rebar is adopted using the model suggested by Holzer et al. (1975) which could also predict the effects of both the strain hardening and strain softening of the reinforcement bar (see Figure 3.5).

CHAPTER 4

NONLINEAR INELASTIC NUMERICAL MODELS OF CONCRETE ENCASED STEEL SECTIONS

4.1 Introduction

Nonlinear numerical analysis using fiber element method has gained its popularity to depict the response of the composite columns. Fiber element analysis method is a powerful analysis method yet easy to be implemented. There are several remarkable advantages of using this method as mentioned below:

1. Materials nonlinear behavior can be easily simulated into the fiber element program using the uniaxial stress-strain relationship of the materials where different materials can be assigned to different fiber elements, i.e. the concrete confinement effects from the reinforcement bar and structural steel, local buckling of the structural steel, the strain-hardening and softening of the materials, and so on.

2. It can generate any shape of cross-section and any number of materials. Since a fiber section can be discretized into small fiber regions, any shape of cross-section is not limited.

3. It can be used to model non-prismatic structural elements. In fiber analysis program, the length of the fiber is not covered in the algorithm. Thus, along the length of the element can be subdivided into many integration points where different fiber cross-sections can be assigned accordingly.

4. Accurate response with time efficiency. To study the complete behavior or determine the ultimate strength of the structural element with complex cross-section and nonlinear materials, the fiber element method can capture higher accuracy than the frame element model, with much less time consuming than the three-dimension finite element model.

4.2 Concrete Confinement Zones

According to Shakir-Khalil and Zeghiche (1989) and Mander et al. (1988), the effectively partially confined concrete zone was assumed to be in the form of the parabolic arches which lie between the longitudinal reinforcements. Similarly, Chen and Lin (2006) also assumed that the highly confined concrete zone occurs in the form of parabolic arching which lie between the structural steel flanges (see Figure 2.1). In order to define the confinement area of the composite column as highly confined area, the parabolic shape can be simplified into the rectangular shape as previously adopted by Mirza and Skrabek (1992), El-Tawil and Deierlein (1999), and Ellobody and Young (2011). For H- and I-shaped steel sections, the highly confined concrete is measured from the web of the steel section to the mid-width of each cantilever flange of the steel. However, for Cross-shaped steel sections, the highly confined concrete is proposed herein to be measured from the web of the steel section to the end of each cantilever flange of the steel. The proposed defined zone is verified through comparing the ultimate load-carrying capacity and the full nonlinear response (elastic and inelastic post-peak softening-response) of the CES columns from the experimental tests. And the partially confined concrete is defined as the concrete area inside the stirrup excluding the highly confined concrete (see Figure 4.1).

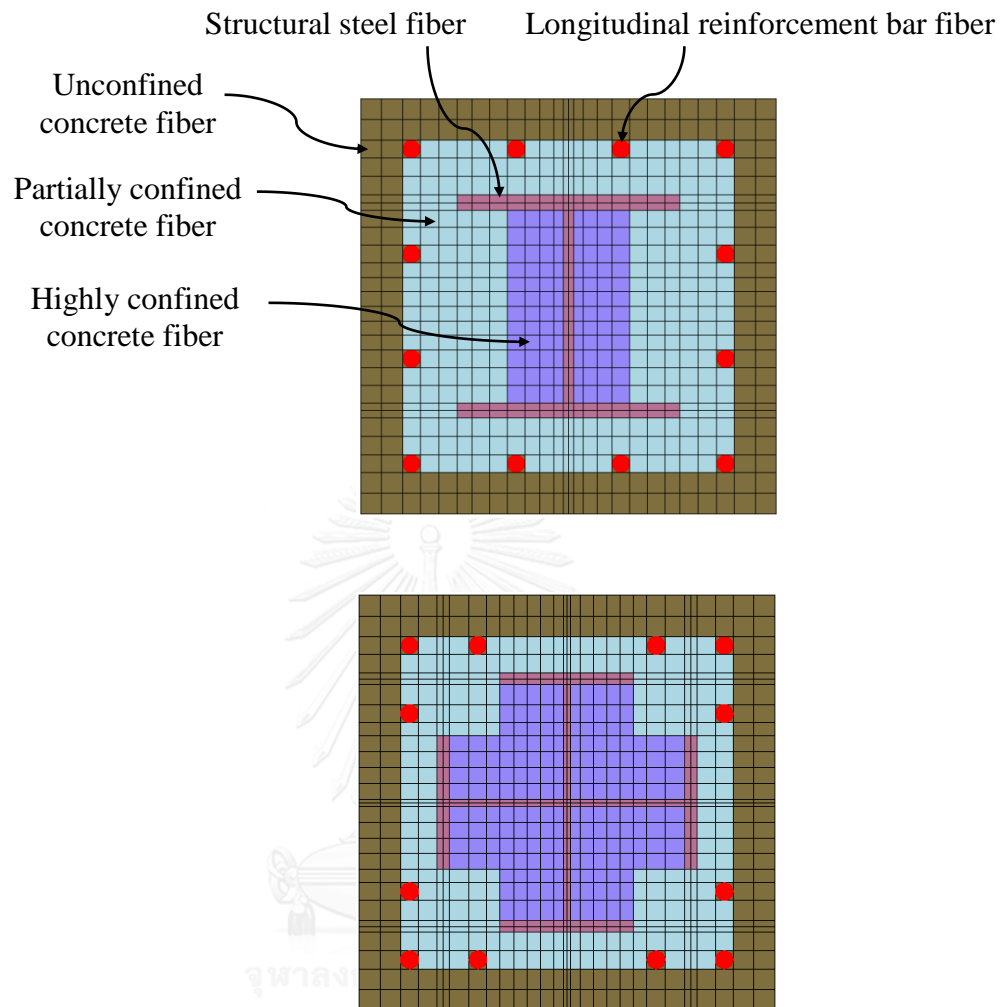


Figure 4.1: Confinement zones and fiber element discretization of CES sections.

4.3 Fiber Element Method

4.3.1 Assumptions

The present fiber analysis method is formulated based on the following assumptions:

1. Plane cross-section remains plane after deformation.
2. Strain is linearly proportional to the distance from the neutral axis.

3. Perfect bond exists between each material – concrete, steel, and reinforcement bars.
4. The effects of creep and shrinkage are neglected.
5. The confinement distribution of the partially confined and highly confined concrete is uniform.
6. Residual stresses of the structural concrete, steel, and rebar are not considered.

4.3.2 Discretization of Composite Sections

The whole composite cross-section is discretized into a suitable number of small connected elements using fiber element concept. Each of the fiber elements can be assigned with different material properties that constitute the models associated with the member length. In essence, the adopted model discretizes the concrete encased steel composite section into five different material regions, namely unconfined concrete, partially confined concrete, highly confined concrete, structural steel and reinforcement bars (see Figure 4.1). The element size adopted typically reads the same size as that of the longitudinal reinforcement bar, where the origin of the cross-section is at the centroid of the composite section. The fiber coordinates (x_i, y_i) and the area of each fiber are based on the fiber discretization and geometry of the composite cross-section with respect to the origin.

4.4 Strain-Curvature Relationships

For the composite section under a uniaxial load incorporating both initial geometric imperfection and slenderness effects, the fiber strain is taken as a function of the curvature (ϕ) and the neutral axis depth (d_n). The strain (ε_i) of each fiber i is calculated from the multiplication of the curvature (ϕ) with an orthogonal distance of

that fiber element from the neutral axis ($d_{o,i}$). Hence, the strain at the extreme top fiber (ε_t) is determined by multiplying the curvature (ϕ) with the depth of the neutral axis. The sign convention used in this work is positive in a compressive strain and negative in a tensile strain.

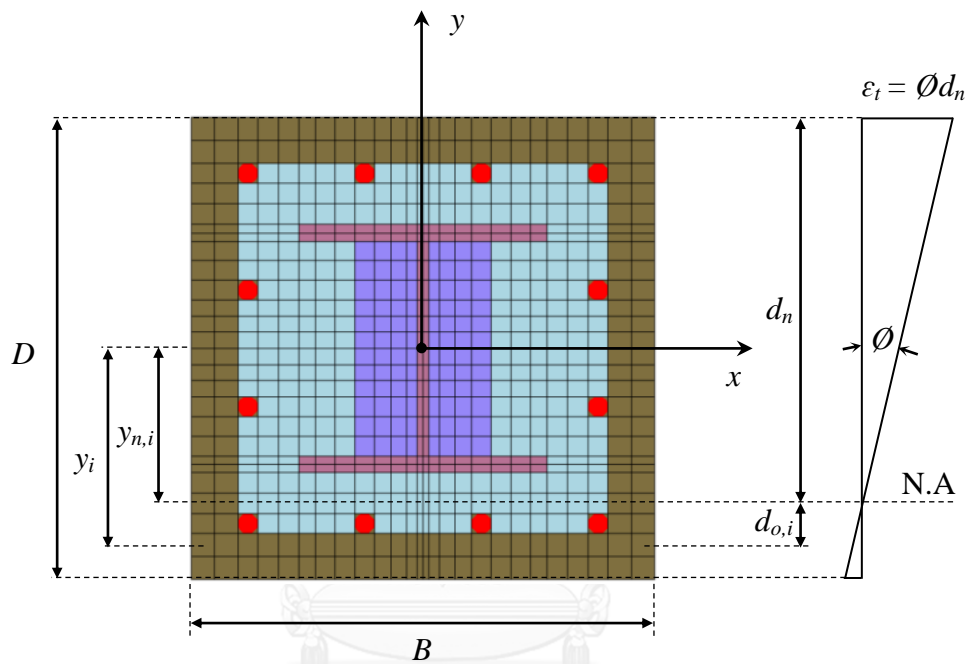


Figure 4.2: Strain-curvature relationship using fiber element model.

In the case of buckling about the x -axis as shown in Figure 4.2, the strain in unconfined concrete, partially confined concrete, highly confined concrete, structural steel and reinforcement bar can be determined by:

$$\varepsilon_i = \begin{cases} \phi d_{o,i} & \text{for } y_i \geq y_{n,i} \\ -\phi d_{o,i} & \text{for } y_i < y_{n,i} \end{cases} \quad (4.1)$$

where y_i is an ordinate of the fiber element i ; $y_{n,i}$ distance from the neutral axis to the fiber element i .

The orthogonal distance from the neutral axis to the centroid of each fiber element i reads:

$$d_{o,i} = |y_i - y_{n,i}| \quad (4.2)$$

The distance from the neutral axis to each fiber element is:

$$y_{n,i} = \frac{D}{2} - d_n \quad (4.3)$$

where D is a cross-sectional depth.

In the case of buckling about the y -axis, the strain in unconfined concrete, partially confined concrete, highly confined concrete, structural steel and reinforcement bar is determined by:

$$\varepsilon_i = \begin{cases} \phi d_{o,i} & \text{for } x_i \geq x_{n,i} \\ -\phi d_{o,i} & \text{for } x_i < x_{n,i} \end{cases} \quad (4.4)$$

where x_i is the ordinate of the fiber element i ; $x_{n,i}$ distance of the neutral axis to a fiber element i . The orthogonal distance of the neutral axis to the centroid of the fiber element i is:

$$d_{o,i} = |x_i - x_{n,i}| \quad (4.5)$$

The distance of the neutral axis to each fiber element is:

$$x_{n,i} = \frac{B}{2} - d_n \quad (4.6)$$

where B is the cross-sectional width.

4.5 Stress Resultants

The fiber element analysis determines the axial force and bending moments developed from the stress resultants. The fiber stresses of the composite section are calculated from the stress-strain relationship of an individual material, and therefore the stress resultants can be determined by integrating the stresses over the corresponding areas; which yields the following expressions:

$$P = \sum_{i=1}^{n_{cu}} (\sigma_{cu,i} A_{cu,i}) + \sum_{i=1}^{n_{cp}} (\sigma_{cp,i} A_{cp,i}) + \sum_{i=1}^{n_{ch}} (\sigma_{ch,i} A_{ch,i}) + \sum_{i=1}^{n_s} (\sigma_{s,i} A_{s,i}) + \sum_{i=1}^{n_r} (\sigma_{r,i} A_{r,i}) \quad (4.7)$$

$$M_x = \sum_{i=1}^{n_{cu}} (\sigma_{cu,i} A_{cu,i} y_{cu,i}) + \sum_{i=1}^{n_{cp}} (\sigma_{cp,i} A_{cp,i} y_{cp,i}) + \sum_{i=1}^{n_{ch}} (\sigma_{ch,i} A_{ch,i} y_{ch,i}) + \sum_{i=1}^{n_s} (\sigma_{s,i} A_{s,i} y_{s,i}) + \sum_{i=1}^{n_r} (\sigma_{r,i} A_{r,i} y_{r,i}) \quad (4.8)$$

$$M_y = \sum_{i=1}^{n_{cu}} (\sigma_{cu,i} A_{cu,i} x_{cu,i}) + \sum_{i=1}^{n_{cp}} (\sigma_{cp,i} A_{cp,i} x_{cp,i}) + \sum_{i=1}^{n_{ch}} (\sigma_{ch,i} A_{ch,i} x_{ch,i}) + \sum_{i=1}^{n_s} (\sigma_{s,i} A_{s,i} x_{s,i}) + \sum_{i=1}^{n_r} (\sigma_{r,i} A_{r,i} x_{r,i}) \quad (4.9)$$

where P is an axial force; M_x, M_y the two bending moments about the x - and y -axes, respectively; $\sigma_{cu,i}, \sigma_{cp,i}, \sigma_{ch,i}, \sigma_{s,i}, \sigma_{r,i}$ the stresses at the centroid of the fiber element i associated with the unconfined concrete, partially confined concrete, highly confined concrete, steel and reinforcement bar, respectively; $A_{cu,i}, A_{cp,i}, A_{ch,i}, A_{s,i}, A_{r,i}$ the

areas of the fiber element i in the unconfined concrete, partially confined concrete, highly confined concrete, steel and reinforcement bar, respectively; $x_{cu,i}$, $y_{cu,i}$, $x_{cp,i}$, $y_{cp,i}$, $x_{ch,i}$, $y_{ch,i}$, $x_{s,i}$, $y_{s,i}$, $x_{r,i}$, $y_{r,i}$ the x-y coordinates of the fiber element i in the unconfined concrete, partially confined concrete, highly confined concrete, steel and reinforcement bar, respectively; n_{cu} , n_{cp} , n_{ch} , n_s , n_r the total number of fiber elements consisted in the unconfined concrete, partially confined concrete, highly confined concrete, steel and reinforcement bar, respectively.



CHAPTER 5

CONCRETE ENCASED STEEL COLUMNS UNDER AXIAL COMPRESSION

5.1 Introduction

In this chapter, the simultaneous ultimate load-carrying capacity and full structural response (post-peak strain softening) of concrete encased steel columns under axial compression are efficiently investigated through a developed numerical nonlinear inelastic analysis. Not only the stub columns, where slenderness and geometric imperfection are negligible, but also the slender CES columns (H-, I-, Cross-encased shaped steel) are numerically analyzed and compared with the relevant experimental tests. The present analysis approach carefully accounts for the materials nonlinearity, geometric nonlinearity, geometric imperfection, various levels of concrete confinement, local buckling of structural steel, and buckling of reinforcement bar (viz. after the crushing concrete material occur during simulation). The resultant stresses contributed from each material, i.e. unconfined, partially-confined, highly-confined concrete, structural steel, and reinforcement bars, under incrementally applied loading can be fully captured and traced for a better understanding of the CES columns responses. After validating the proposed numerical approach, parametric sensitivity analyses are performed to dig into the influences from key parameters such as the spacing of lateral ties (effects of confinement level), effective length ratio, structural steel yield stress, and concrete compressive strength on the performance of CES columns.

5.2 Numerical Analysis Approach

5.2.1 Imperfection and Buckling Modeling of Composite Columns

The concrete encased steel composite column is modeled as a pin-ended column subjected to a concentric axial load with initial geometric imperfection as shown in Figure 5.1. It is assumed that the columns buckle in a single curvature and the most critical section occurs at the column mid-height. The buckling shape of the column can be described by a sine wave equation (Shakir-Khalil and Zeghiche 1989):

$$\delta(z) = \delta_{mi} \sin\left(\frac{\pi z}{L}\right) \quad (5.1)$$

where δ is a lateral displacement at any point along the column length; L the column effective length; δ_{mi} the lateral displacement at the column mid-height; and z the longitudinal direction of the column.

The column curvature can then be determined from the lateral displacement:

$$\phi(z) = \frac{\partial^2 \delta(z)}{\partial z^2} = \left(\frac{\pi}{L}\right)^2 \delta_{mi} \sin\left(\frac{\pi z}{L}\right) \quad (5.2)$$

The column curvature at the mid-height is taken as

$$\phi_{mi} = \left(\frac{\pi}{L}\right)^2 \delta_{mi} \quad (5.3)$$

The total external bending moment at the column mid-height under the concentrically applied axial load with the initial imperfection reads

$$M_{e,mi} = P(\delta_{im} + \delta_{mi}) \quad (5.4)$$

where δ_{im} is the initial geometric imperfection of the column.

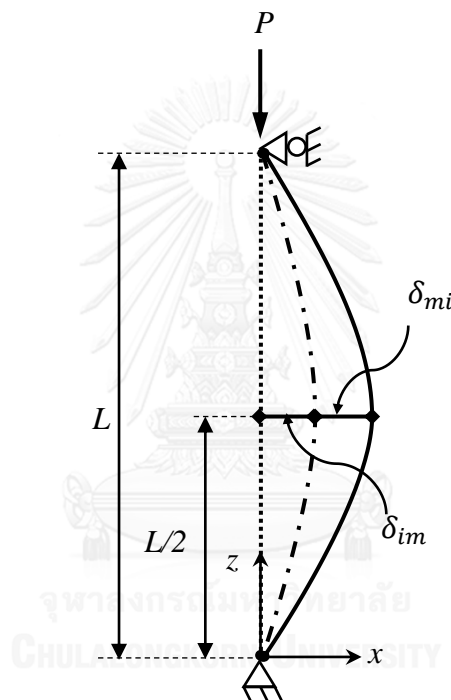


Figure 5.1: Concentrically applied force and initial imperfection of a pin-ended column.

5.2.2 Müller's Algorithm

The numerical method of Müller (1956) requires three initial points to iteratively approximate the solutions. The present scheme adopts the three initial neutral axis depth values to find in the next iteration the neutral axis depth, which satisfies the moment equilibrium of the concrete encased steel composite column with the confinement effects. For each incremental step, the external moments associated

with the initial geometric imperfection and the lateral displacement at a column mid-height under an axial load must be in equilibrium with the internal moment at the same height. For the given initial values of the neutral axis depth ($d_{n,1}, d_{n,2}, d_{n,3}$), the neutral axis depth value in the next iteration is determined by:

$$f_m = P(\delta_{im} + \delta_{mi}) - M_{mi} \quad (5.5)$$

$$A = \frac{(d_{n,2} - d_{n,3})(f_{m,1} - f_{m,3}) - (d_{n,1} - d_{n,3})(f_{m,2} - f_{m,3})}{(d_{n,1} - d_{n,2})(d_{n,2} - d_{n,3})(d_{n,1} - d_{n,3})} \quad (5.6)$$

$$B = \frac{(d_{n,1} - d_{n,3})^2(f_{m,2} - f_{m,3}) - (d_{n,2} - d_{n,3})^2(f_{m,1} - f_{m,3})}{(d_{n,1} - d_{n,2})(d_{n,2} - d_{n,3})(d_{n,1} - d_{n,3})} \quad (5.7)$$

$$C = f_{m,3} \quad (5.8)$$

$$d_{n,4} = d_{n,3} - \frac{2C}{B \pm \sqrt{B^2 - 4AC}} \quad (5.9)$$

where f_m is Müller's function of the residual moment at the column mid-height; δ_{im} the initial geometric imperfection of the column, i.e. $L/2000$ (Ellobody and Young 2011); δ_{mi} the lateral displacement at the column mid-height; M_{mi} the internal bending moment of the composite cross-section; A, B, C the coefficients underlying Müller's parabolic equation.

At each step, the initial trial of the neutral axis depth values $d_{n,1}, d_{n,2}, d_{n,3}$ is crucial to obtain the solution convergence. Therefore, the present approach proposes the simple yet efficient adaptive technique that can provide the good initial approximation. In essence, during the pre-peak structural response the neutral axis depth lies within the range between 0 to $2D/3$. When the structural response establishes strain softening and large lateral deformation at the mid-height, the neutral axis is found at $D/2$.

Thus, the algorithm adopts the initial neutral axis depth values of $d_{n,1} = D/4$, $d_{n,2} = D/2$ and $d_{n,3} = 2D/3$ as when the resulting neutral axis depth is less than 80 percent of the cross-section mid-depth. On the other hand, these initial values take $d_{n,1} = D/4$, $d_{n,2} = D/2$ and $d_{n,3} = D$ as when the resulting depth reaches 80 percent of the cross-section mid-depth.

Equation 5.9 yields the two solution roots that correspond to the positive and negative signs in the denominator. The Müller's method selects the solution with the root sign that is similar to the sign of B . If only real roots are located, it is important to choose the two original points that are closest to the new estimated root. Hence, the values of $d_{n,1}, d_{n,2}, d_{n,3}$ with the corresponding functions $f_{m,1}, f_{m,2}, f_{m,3}$ are exchanged accordingly (viz. $d_{n,4}$ is close to $d_{n,3}$) using the following algorithms:

$$\begin{pmatrix} d_{n,1} \\ d_{n,2} \\ f_{m,1} \\ f_{m,2} \end{pmatrix}_{i+1} = \begin{pmatrix} d_{n,2} \\ d_{n,1} \\ f_{m,2} \\ f_{m,1} \end{pmatrix}_i \quad \text{if} \quad |d_{n,4} - d_{n,2}| < |d_{n,4} - d_{n,1}| \quad (5.10)$$

$$\begin{pmatrix} d_{n,2} \\ d_{n,3} \\ f_{m,2} \\ f_{m,3} \end{pmatrix}_{i+1} = \begin{pmatrix} d_{n,3} \\ d_{n,2} \\ f_{m,3} \\ f_{m,2} \end{pmatrix}_i \quad \text{if} \quad |d_{n,4} - d_{n,3}| < |d_{n,4} - d_{n,2}| \quad (5.11)$$

The Müller's iterative procedures are repeated until the preset tolerance (ε_{tol}) satisfies the convergence condition of $|f_m| \leq \varepsilon_{tol}$. In this study, the tolerance is set to $\varepsilon_{tol} = 0.0001$.

5.2.3 Computational Procedures for Load and Axial Strain Responses

The complete nonlinear responses of the concrete encased steel composite column under the concentrically applied axial load with the initial geometric imperfection can be traced using the proposed inelastic fiber element analysis in the lateral displacement (δ_{mi}) control at a column mid-height. The analysis procedures are summarized by the flowchart in Figure 5.2.

More explicitly, the lateral displacement δ_{mi} is incrementally increased by the analysis to simulate the buckling behavior of the column, whilst the corresponding curvature ϕ_{mi} is obtained as a by-product. The strain developed at the centroid of each fiber element of the composite column cross-section is calculated from Equations 4.1 and 4.4. The stresses associated with the unconfined concrete, partially confined concrete, highly confined concrete, structural steel and reinforcement bars are determined from the uniaxial stress-strain relationship of the material concerned. For each of the lateral displacement increments, the neutral axis depth is adjusted using Müller's method that enforces equilibrium of the moment at the column mid-height. The analysis procedure is then repeated with the successive increment of the mid-height lateral displacement, such that the complete axial force and strain

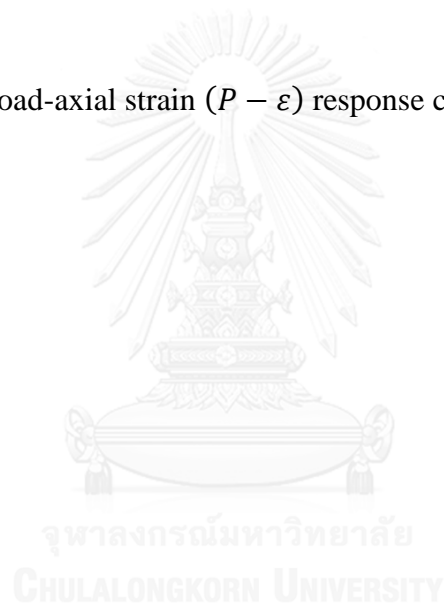
(nonlinear) responses can be computed. Various critical behaviors of the concrete encased steel composite column under the full history of the axial force with the initial geometric imperfection (e.g. initial stiffness, maximum strength capacity, post-peak response and ductility) can be identified directly from the resulting axial load and strain diagram.

The step-by-step procedures along with the flowchart, as shown in Figure 5.2, of the nonlinear inelastic analysis program of the concrete encased steel composite columns under axial load with initial geometric imperfection are summarized below:

1. Input the dimensions and the initial geometric imperfection of the concrete encased steel composite column.
2. Define the zones of the unconfined concrete, partially confined concrete, highly confined concrete.
3. Impose the stopping criteria by specifying the maximum axial load P_{max} , the limit deflection δ_{limit} , the convergence tolerances ϵ_{tol} , ϵ_d .
4. Define the material models for the unconfined concrete, partially confined concrete, highly confined concrete, structural steel, and reinforcement bar.
5. Discretize the composite cross-section into fiber elements.
6. Calculate the area of the fiber elements and the distance from the centroid of the composite section to the each fiber element's center point.
7. Impose the initial lateral buckling displacement δ_{mi} at the mid-height of the column by an increment of $\Delta\delta_{mi}$.
8. Use the Equation 5.3 to determine the mid-height curvature ϕ_{mi} from the imposed lateral buckling displacement δ_{mi} at the mid-height of the column.

9. Choose the initial guessing values of the neutral axis depth $d_{n,1}, d_{n,2}, d_{n,3}$ as $D/4, D/2, 2D/3$ respectively. However, these initial values will be chosen using the adaptive technique as explained earlier in the Müller's numerical method.
10. Using the chosen initial values of the neutral axis depth $d_{n,1}, d_{n,2}, d_{n,3}$ to compute the fiber strains of each material.
11. Calculate the fiber stresses of the unconfined concrete, partially confined concrete, highly confined concrete, structural steel, and reinforcement bar from the uniaxial stress-strain relationships accordingly.
12. Calculate the internal axial force P and the internal bending moment M_{mi} carried by the composite column, and the external bending moment $M_{e,mi}$ corresponding to the initial guessing values.
13. Determine the Müller's function of the residual moments $f_{m,1}, f_{m,2}, f_{m,3}$ at the mid-height of the composite column corresponding to the initial values of the neutral axis depths $d_{n,1}, d_{n,2}, d_{n,3}$.
14. Compute the coefficients A, B, C and the adjusted neutral axis depth $d_{n,4}$ using Müller's numerical method.
15. Compute the strains and stresses of the each fiber element corresponding to the adjusted neutral axis depth $d_{n,4}$ from the material uniaxial stress-strain relationships.
16. Calculate the internal axial force P and the internal bending moment M_{mi} carried by the composite column, and the external bending moment $M_{e,mi}$ corresponding to the adjusted neutral axis depth $d_{n,4}$.

17. Calculate the residual moment $f_{m,4}$ of the Müller's function.
18. Check the conditions using Equations 5.10-5.11 for the interchanged values of $d_{n,1}, d_{n,2}, d_{n,3}$ along with the corresponding residual moments $f_{m,1}, f_{m,2}, f_{m,3}$.
19. Check the convergence condition $|f_m| \leq \varepsilon_{tol}$. If the convergence condition is satisfied, proceed to the next step. Otherwise, repeat from step (14) to (18).
20. Increase the mid-height lateral buckling displacement, $\delta_{mi} = \delta_{mi} + \Delta\delta_{mi}$. Repeat from step (8) to (19) until the imposed stopping criteria in step (3) is reached.
21. Generate the load-axial strain ($P - \varepsilon$) response curve.



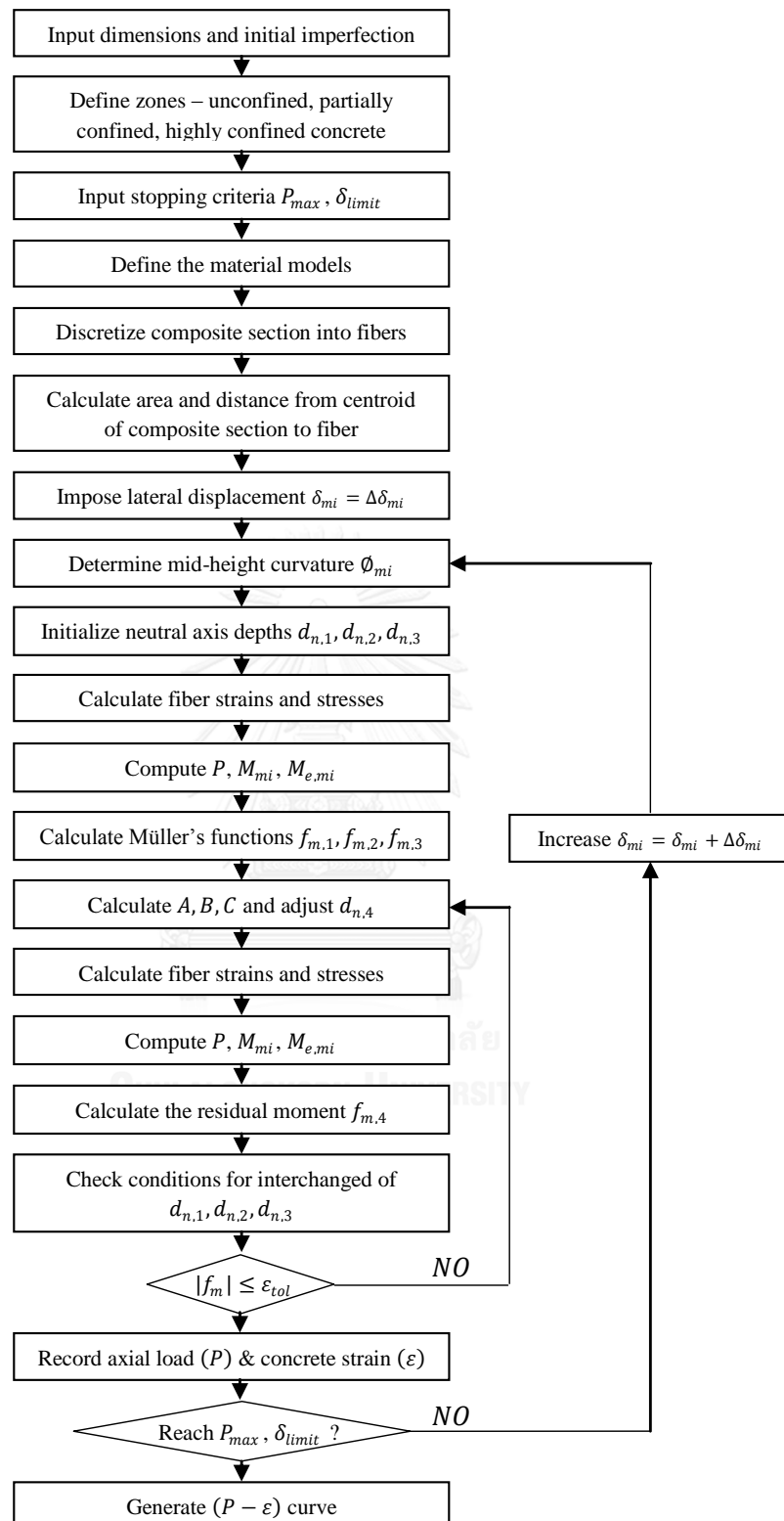


Figure 5.2: Flowchart summarizing the analysis procedures to obtain axial load and strain responses of concrete encased steel composite columns.

5.3 Validation of the Numerical Approach

5.3.1 Summary of Relevant Experimental Tests

The present work employs five experimental studies from Anslijn and Janss (1974), Matsui (1979), Chen and Yeh (1996), Tsai et al. (1996) and Zhao et al. (2005). The column specimens were pin-ended concrete encased steel composite columns under a concentrically applied axial force. Tables 5.1 and 5.2 detail the dimensions, material properties, and cross-sectional configurations (i.e. H-, I-, Cross-encased steel shaped) of all the composite column specimens involved. A total of thirty-three full-scale stub and slender CES column specimens are used for validating the proposed nonlinear numerical approach.

Table 5.1: Dimensions, steel sections, and material strength of CES column specimens

| Specimen ID | Dimensions | | | Structural steel sections | | Material strength | | | References |
|-------------|------------|----------|-----------|---------------------------|---|-------------------|-------------|-------------|---------------------|
| | B (mm) | D (mm) | kL (mm) | Shape | $b \times d \times t_w \times t_f$ (mm) | Concrete (MPa) | Steel (MPa) | Rebar (MPa) | |
| C1 | 280 | 280 | 1200 | H | $150 \times 150 \times 7 \times 10$ | 29.5** | 296 | 350 | Chen and Yeh (1996) |
| C2 | 280 | 280 | 1200 | H | $150 \times 150 \times 7 \times 10$ | 28.1** | 296 | 350 | |
| C3 | 280 | 280 | 1200 | H | $150 \times 150 \times 7 \times 10$ | 29.8** | 296 | 350 | |
| C4 | 280 | 280 | 1200 | I | $75 \times 150 \times 5 \times 7$ | 28.1** | 303 | 350 | |
| C5 | 280 | 280 | 1200 | I | $75 \times 150 \times 5 \times 7$ | 26.4** | 303 | 350 | |
| C6 | 280 | 280 | 1200 | I | $75 \times 150 \times 5 \times 7$ | 28.1** | 303 | 350 | |
| C7 | 280 | 280 | 1200 | I | $75 \times 150 \times 5 \times 7$ | 29.8** | 303 | 350 | |
| C8 | 280 | 280 | 1200 | Cross | $2 (90 \times 175 \times 5 \times 8)$ | 29.8** | 345 | 350 | |
| C9 | 280 | 280 | 1200 | Cross | $2 (90 \times 175 \times 5 \times 8)$ | 29.8** | 345 | 350 | |
| C10 | 280 | 280 | 1200 | Cross | $2 (90 \times 175 \times 5 \times 8)$ | 29.5** | 345 | 350 | |
| C11 | 160 | 160 | 924 | H | $100 \times 100 \times 6 \times 8$ | 18.5* | 306 | 376 | Matsui (1979) |
| C12 | 160 | 160 | 2309 | H | $100 \times 100 \times 6 \times 8$ | 21.4* | 298 | 376 | |
| C13 | 160 | 160 | 3464 | H | $100 \times 100 \times 6 \times 8$ | 22.5* | 304 | 376 | |

| | | | | | | | | | |
|-----|-----|-----|------|-------|--------------------------|--------|-----|-----|----------------------------|
| C14 | 240 | 240 | 4280 | H | 140 × 140 × 7 × 12 | 38* | 285 | - | Anslin and Janss (1974) |
| C15 | 240 | 240 | 3486 | H | 140 × 140 × 7 × 12 | 33.6* | 293 | - | |
| C16 | 240 | 240 | 2490 | H | 140 × 140 × 7 × 12 | 37.6* | 276 | - | |
| C17 | 240 | 240 | 2488 | H | 140 × 140 × 7 × 12 | 33.6* | 276 | - | |
| C18 | 240 | 240 | 1288 | H | 140 × 140 × 7 × 12 | 33.6* | 276 | - | |
| C19 | 240 | 240 | 1253 | H | 140 × 140 × 7 × 12 | 35.4* | 276 | - | |
| C20 | 160 | 180 | 2800 | I | 68 × 100 × 4.5 × 7.6 | 59.8* | 379 | 358 | Zhao et al. (2005) |
| C21 | 160 | 180 | 3500 | I | 68 × 100 × 4.5 × 7.6 | 55.7* | 379 | 358 | |
| C22 | 160 | 180 | 3500 | I | 68 × 100 × 4.5 × 7.6 | 50.7* | 379 | 358 | |
| C23 | 160 | 180 | 4100 | I | 68 × 100 × 4.5 × 7.6 | 67* | 379 | 358 | |
| C24 | 280 | 280 | 1200 | Cross | 2 (90×175 × 5 × 8) | 23.9** | 274 | 453 | Tsai et al. (1996) |
| C25 | 280 | 280 | 1200 | Cross | 2 (90×175 × 5 × 8) | 23.5** | 274 | 453 | |
| C26 | 280 | 280 | 1200 | Cross | 2 (90×175 × 5 × 8) | 21.8** | 274 | 453 | |
| C27 | 280 | 280 | 1200 | Cross | 2 (90×175 × 5 × 8) | 25.3** | 274 | 453 | |
| C28 | 280 | 280 | 1200 | Cross | 2 (50 × 160 × 3.2 × 4.5) | 26.0** | 271 | 453 | |
| C29 | 280 | 280 | 1200 | Cross | 2 (50 × 160 × 3.2 × 4.5) | 26.3** | 271 | 453 | |
| C30 | 280 | 280 | 1200 | Cross | 2 (50 × 160 × 3.2 × 4.5) | 25.0** | 271 | 453 | |
| C31 | 280 | 280 | 1200 | Cross | 2 (50 × 160 × 3.2 × 4.5) | 26.6** | 271 | 453 | |
| C32 | 280 | 280 | 1200 | Cross | 2 (50 × 160 × 3.2 × 4.5) | 24.6** | 271 | 453 | |
| C33 | 280 | 280 | 1200 | Cross | 2 (50 × 160 × 3.2 × 4.5) | 24.3** | 271 | 453 | |

* Concrete cube strength

** Concrete cylinder strength

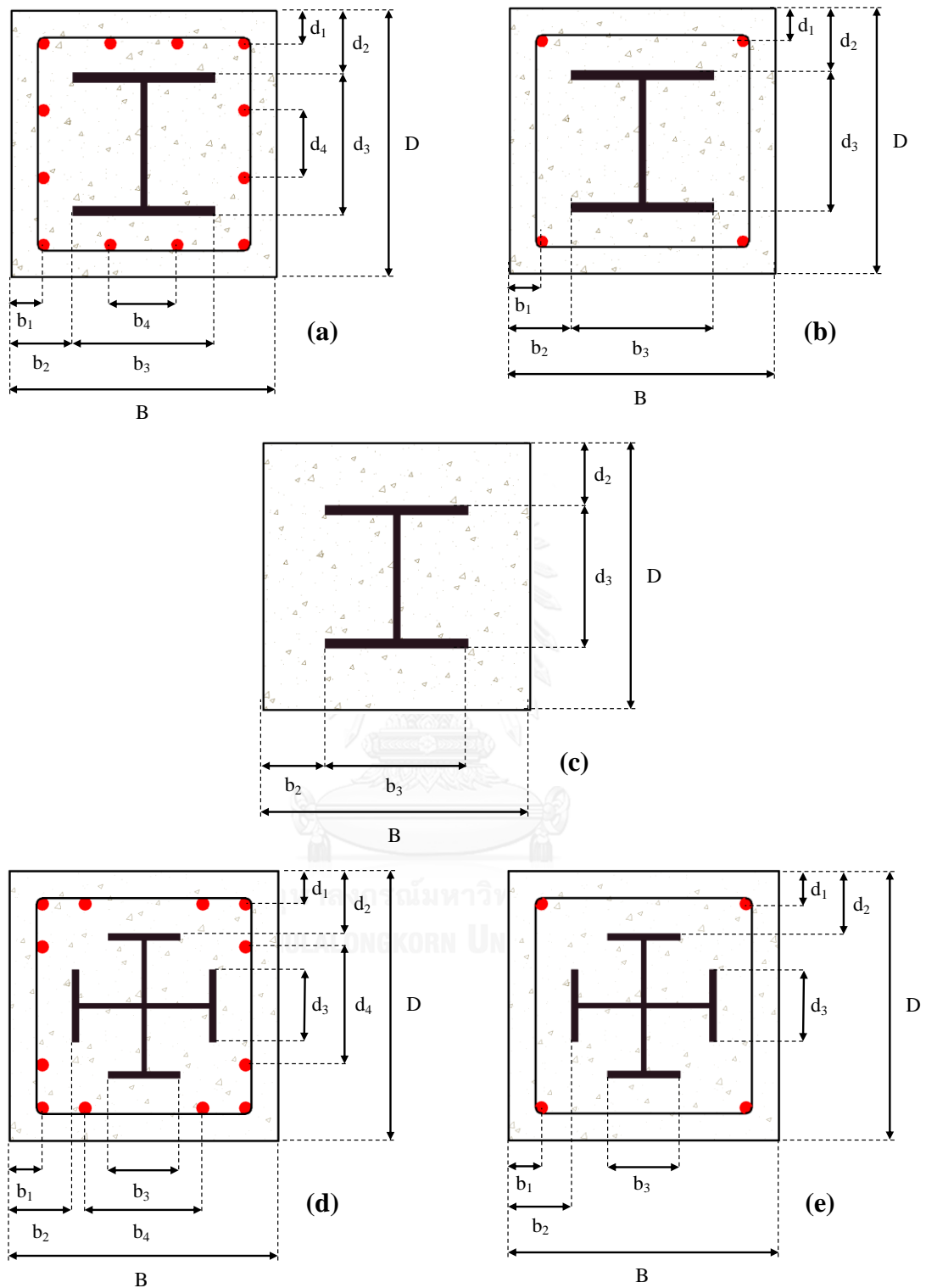


Figure 5.3: Cross-section configurations of CES columns (a) H-, I-shaped with distributed rebar, (b) H-, I-shaped with corner rebar, (c) H-, I-shaped without rebar, (d) Cross-shaped with distributed rebar, and (e) Cross-shaped with corner rebar.

Table 5.2: Reinforcement bar and structural steel details of CES column specimens

| Specimen ID | Concrete Encased Steel Composite Dimensions | | | | | | | | Reinforcements | | | |
|-------------|---|---------------|---------------|---------------|---------------|---------------|---------------|---------------|----------------|------|---------|---|
| | b_1 (mm) | b_2 (mm) | b_3 (mm) | b_4 (mm) | d_1 (mm) | d_2 (mm) | d_3 (mm) | d_4 (mm) | Main bar | | Stirrup | |
| | | | | | | | | | Number | Ø | Spacing | Ø |
| C1 | 34 | 65 | 150 | 70.7 | 34 | 65 | 150 | 70.7 | 12 | 15.9 | 140 | 8 |
| C2 | 34 | 65 | 150 | 70.7 | 34 | 65 | 150 | 70.7 | 12 | 15.9 | 75 | 8 |
| C3 | 34 | 65 | 150 | 70.7 | 34 | 65 | 150 | 70.7 | 12 | 15.9 | 35 | 8 |
| C4 | 34 | 65 | 75 | 70.7 | 34 | 65 | 150 | 70.7 | 12 | 15.9 | 140 | 8 |
| C5 | 34 | 65 | 75 | 70.7 | 34 | 65 | 150 | 70.7 | 12 | 15.9 | 75 | 8 |
| C6 | 34 | 65 | 75 | 70.7 | 34 | 65 | 150 | 70.7 | 12 | 15.9 | 140 | 8 |
| C7 | 34 | 65 | 75 | 70.7 | 34 | 65 | 150 | 70.7 | 12 | 15.9 | 75 | 8 |
| C8 | 34 | 52.5 | 90 | 120 | 34 | 52.5 | 90 | 120 | 12 | 15.9 | 140 | 8 |
| C9 | 34 | 52.5 | 90 | 120 | 34 | 52.5 | 90 | 120 | 12 | 15.9 | 75 | 8 |
| C10 | 34 | 52.5 | 90 | 120 | 34 | 52.5 | 90 | 120 | 12 | 15.9 | 35 | 8 |
| C11 | 19 | 30 | 100 | - | 19 | 30 | 100 | - | 4 | 6 | 75 | 4 |
| C12 | 19 | 30 | 100 | - | 19 | 30 | 100 | - | 4 | 6 | 75 | 4 |
| C13 | 19 | 30 | 100 | - | 19 | 30 | 100 | - | 4 | 6 | 75 | 4 |
| C14 | - | 50 | 140 | - | - | 50 | 140 | - | - | - | - | - |
| C15 | - | 50 | 140 | - | - | 50 | 140 | - | - | - | - | - |
| C16 | - | 50 | 140 | - | - | 50 | 140 | - | - | - | - | - |
| C17 | - | 50 | 140 | - | - | 50 | 140 | - | - | - | - | - |
| C18 | - | 50 | 140 | - | - | 50 | 140 | - | - | - | - | - |
| C19 | - | 50 | 140 | - | - | 50 | 140 | - | - | - | - | - |
| C20 | 15 | 46 | 68 | - | 15 | 40 | 100 | - | 4 | 12 | 150 | 6 |
| C21 | 15 | 46 | 68 | - | 15 | 40 | 100 | - | 4 | 12 | 150 | 6 |
| C22 | 15 | 46 | 68 | - | 15 | 40 | 100 | - | 4 | 12 | 150 | 6 |
| C23 | 15 | 46 | 68 | - | 15 | 40 | 100 | - | 4 | 12 | 150 | 6 |
| C24 | 34 | 52.5 | 90 | - | 34 | 52.5 | 90 | - | 4 | 15.9 | 140 | 8 |
| C25 | 34 | 52.5 | 90 | - | 34 | 52.5 | 90 | - | 4 | 15.9 | 100 | 8 |
| C26 | 34 | 52.5 | 90 | 120 | 34 | 52.5 | 90 | 120 | 12 | 15.9 | 100 | 8 |
| C27 | 34 | 52.5 | 90 | 120 | 34 | 52.5 | 90 | 120 | 12 | 15.9 | 100 | 8 |
| C28 | 34 | 60 | 50 | - | 34 | 60 | 50 | - | 4 | 15.9 | 190 | 8 |
| C29 | 34 | 60 | 50 | - | 34 | 60 | 50 | - | 4 | 15.9 | 140 | 8 |
| C30 | 34 | 60 | 50 | 120 | 34 | 60 | 50 | 120 | 12 | 15.9 | 140 | 8 |
| C31 | 34 | 60 | 50 | - | 34 | 60 | 50 | - | 4 | 15.9 | 100 | 8 |
| C32 | 34 | 60 | 50 | 120 | 34 | 60 | 50 | 120 | 12 | 15.9 | 100 | 8 |
| C33 | 34 | 60 | 50 | 120 | 34 | 60 | 50 | 120 | 12 | 15.9 | 100 | 8 |

In the test from Chen and Yeh (1996), the effects of different transversal reinforcement bar spacing and structural steel shapes were investigated. Seven stub concrete encased steel composite column specimens C1-C10 composing respectively of three H-shaped, four I-shaped, three Cross-shaped structural steel sections encased with 12 longitudinal reinforcement bars (see Figure 5.3a, d) are employed in this study. Furthermore, the cross-section configurations of the composite column specimens C11-C13 conducted by Matsui (1979) is represented in Figure 5.3b. Anslijn and Janss (1974) conducted a series of the tests on the stub and slender concrete encased steel composite column without longitudinal reinforcement bars (viz. specimens C14-C19 configured in Figure 5.3c). The recent experimental tests were carried out by Zhao et al. (2005) on the slender concrete encased steel composite columns under an axial load with/without eccentricity. Only four composite column specimens C20-C23 in Figure 5.3b were solely applied by a concentric axial load. Ten full-scale concrete encased Cross-shaped steel composite stub columns with longitudinal reinforcement bars (see Figure 5.3d, e) were tested by Tsai et al. (1996).

5.3.2 Comparison between the numerical and experimental results

This section illustrates comparisons of the responses and the corresponding maximum strength of the concrete encased steel composite columns obtained from the proposed numerical analysis approach and 33 available experimental results (Anslijn and Janss 1974, Matsui 1979, Chen and Yeh 1996, Tsai et al. 1996, Zhao et al. 2005). Table 5.3 summarizes the maximum load carrying capacity calculated by the present scheme (P_{Prop}) and the tests (P_{Test}).

Table 5.3: Comparisons between the numerical analyses with the test results

| Specimen ID | Test P_{Test} (kN) | Proposed method P_{Prop} (kN) | $\frac{P_{Prop}}{P_{Test}}$ | References |
|-------------|-------------------------|------------------------------------|-----------------------------|--------------------------|
| C1 | 4220 | 4174 | 0.99 | |
| C2 | 4228 | 4093 | 0.97 | |
| C3 | 4399 | 4272 | 0.97 | |
| C4 | 3788 | 3497 | 0.92 | |
| C5 | 3683 | 3398 | 0.92 | |
| C6 | 3630 | 3497 | 0.96 | Chen and Yeh (1996) |
| C7 | 3893 | 3644 | 0.94 | |
| C8 | 4441 | 4574 | 1.03 | |
| C9 | 4519 | 4609 | 1.02 | |
| C10 | 4527 | 4618 | 1.02 | |
| C11 | 996 | 1025 | 1.03 | |
| C12 | 974 | 1013 | 1.04 | Matsui (1979) |
| C13 | 874 | 857 | 0.98 | |
| C14 | 2148 | 2174 | 1.01 | |
| C15 | 2344 | 2261 | 0.97 | |
| C16 | 2628 | 2597 | 0.99 | |
| C17 | 2344 | 2432 | 1.04 | Anslijn and Janss (1974) |
| C18 | 2550 | 2544 | 1.00 | |
| C19 | 2746 | 2623 | 0.96 | |
| C20 | 1457 | 1566 | 1.07 | |
| C21 | 1270 | 1265 | 1.00 | |
| C22 | 1183 | 1180 | 1.00 | Zhao et al. (2005) |
| C23 | 1330 | 1190 | 0.90 | |
| C24 | 3602 | 3458 | 0.96 | |
| C25 | 3502 | 3467 | 0.99 | |
| C26 | 3836 | 3951 | 1.03 | |
| C27 | 3854 | 4201 | 1.09 | |
| C28 | 3063 | 2849 | 0.93 | |
| C29 | 3009 | 2919 | 0.97 | Tsai et al. (1996) |
| C30 | 3696 | 3474 | 0.94 | |
| C31 | 3088 | 2964 | 0.96 | |
| C32 | 3748 | 3448 | 0.92 | |
| C33 | 3744 | 3444 | 0.92 | |
| Average | - | - | 0.98 | |
| SD | - | - | 0.05 | |
| COV | - | - | 0.05 | |

Clearly, good agreements between P_{Prop} and P_{Test} have been evidenced, in which the average value, the standard deviation (SD) and the coefficient of variation (COV) of the P_{Prop}/P_{Test} ratio are 0.98, 0.05 and 0.05, respectively. More importantly, the proposed analysis approach is able to capture the complete axial load and strain responses of the concrete encased steel composite columns under the concentrically applied compression force. Again, good agreements between the obtained response results and the experiment data are clearly illustrated in Figure 5.4 - 5.6 for the CES specimens C2 (H-shaped steel section), C4 (I-shaped section), and C8 (Cross-shaped section), respectively.

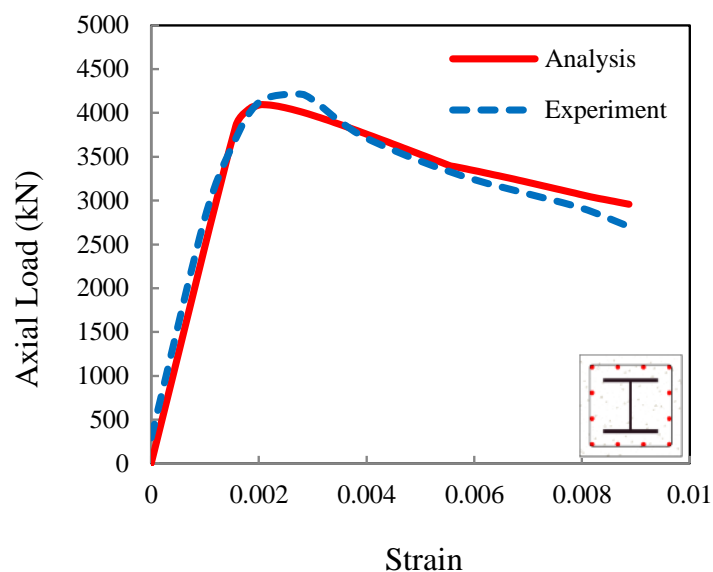


Figure 5.4: Axial load and strain response from the present analysis approach and the experiment for H-shaped encased specimen C2.

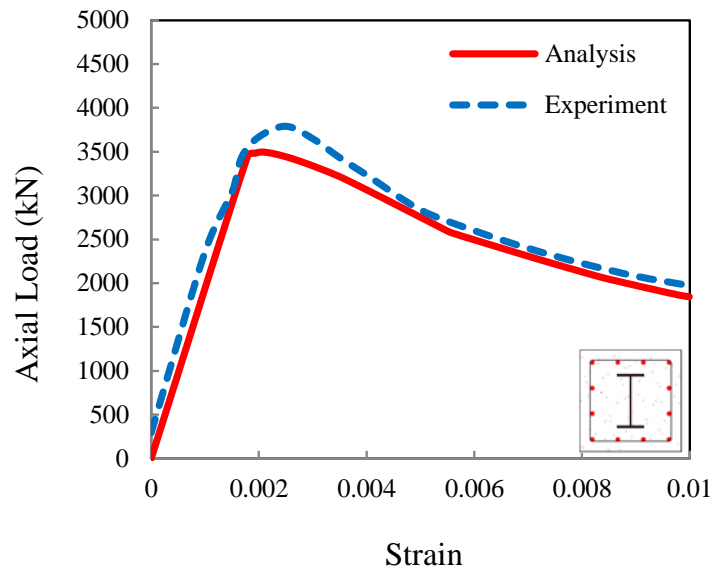


Figure 5.5: Axial load and strain response from the present analysis approach and the experiment for I-shaped encased specimen C4.

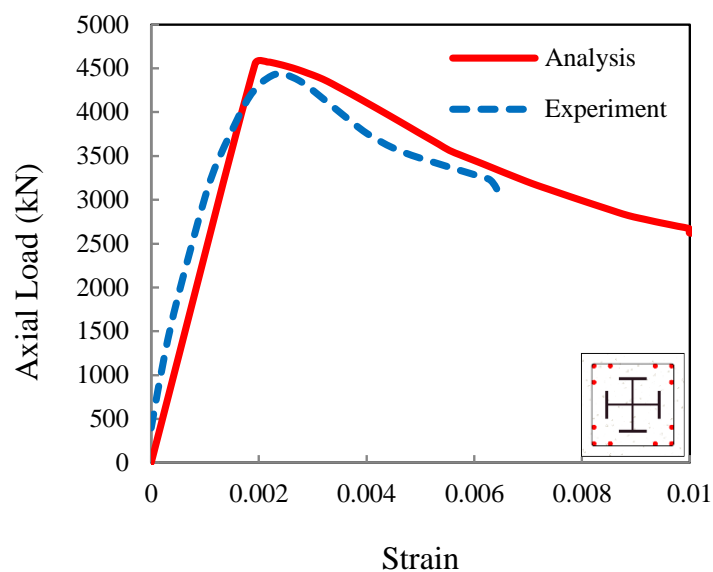


Figure 5.6: Axial load and strain response from the present analysis approach and the experiment for Cross-shaped encased specimen C8.

Not only can the pre-peak behavior be captured accurately, but also the sophisticated post-peak softening response is mapped out efficiently using the proposed nonlinear inelastic fiber element analysis procedure, which incorporates the

constitutive models of various levels of concrete confinement, stability of structural steel and reinforcement bars, simultaneously.

Furthermore, the axial load and strain relationship associated with each of the composite material components is displayed in Figure 5.7. For instance, the maximum strength capacity of the composite column is approached as when the stresses underpinning both structural steel and longitudinal reinforcement bars reach the yield stress values. Corresponding to this critical load, the unconfined concrete stress deteriorates and undergoes the softening portion. Obviously, the concrete (partial and high) confinement effects enhance the overall load carrying capacity of the composite column.

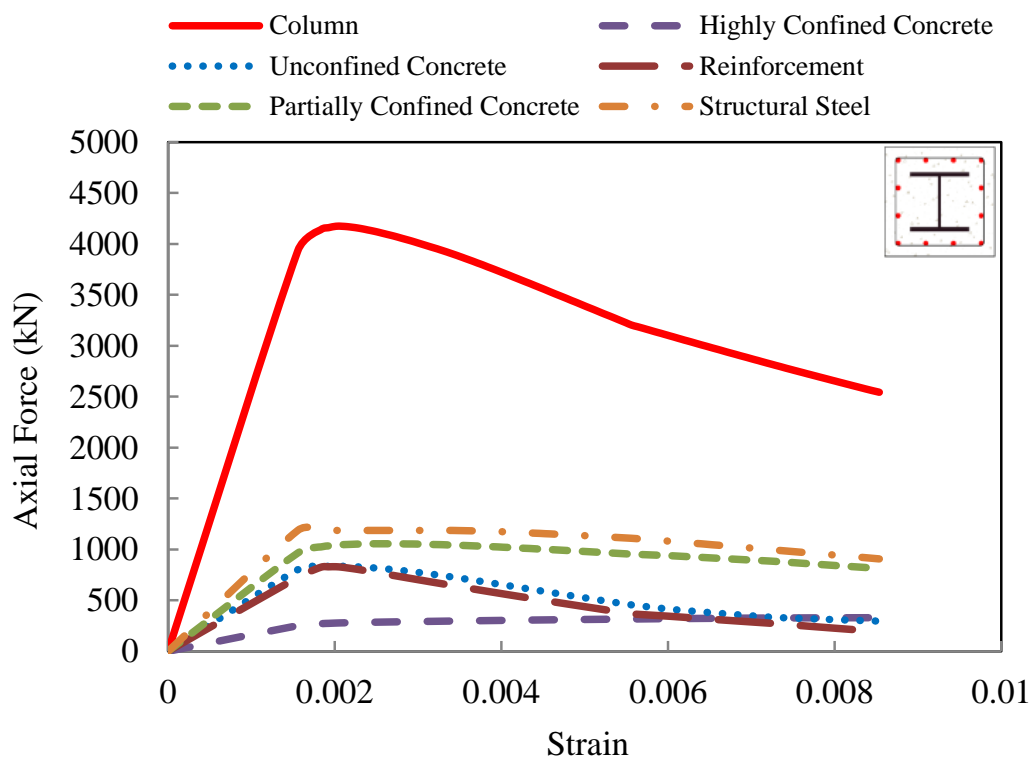


Figure 5.7: Axial load and strain responses of each composite component of specimen C1 obtained by the present analysis approach.

5.4 Parametric Sensitivity Analyses

5.4.1 Description of Parameters

This section performs the parametric study of some key parameters, namely the width-to-effective length (B/kL) ratio, transverse tie (stirrup) spacing, concrete strength and structural steel yield stress. In essence, it investigates the influences of these parameters on the overall response and maximum strength capacity of the concrete encased steel composite columns. Table 5.4 summarizes 54 parametric variations of specimen dimensions and material properties of 18 column groups (G1-G18), where the B/kL ratio is varied within the range of 0.03 and 0.16.

The specimen groups G1-G9 (previously conducted by Matsui (1979)) contain the square concrete cross-section of ($160 \times 160 \text{ mm}^2$) encasing the H-shaped structural steel ($b \times d \times t_w \times t_f = 100 \times 100 \times 6 \times 8$) with four longitudinal reinforcement bars (a diameter of 6 mm) at corners and a transverse tie diameter of 4 mm (see Figure 5.3b). The specimen groups G10-G18 (also studied by Zhao et al. (2005)) consist of a rectangular concrete cross-section ($160 \times 180 \text{ mm}^2$) encasing the I-shaped structural steel cross-section ($b \times d \times t_w \times t_f = 68 \times 100 \times 4.5 \times 7.6$) with four longitudinal reinforcement bars (a diameter of 12 mm) at corners and a stirrup diameter of 6 mm.

The column specimen groups G1-G3 and G10-G12 contain the similar concrete cube strength (f'_c), steel yield stress (f_{ys}) and reinforcement bar yield stress (f_{yr}) to those conducted by Matsui (1979) and (Zhao et al. (2005)), respectively. The present study varies the parameters, namely the B/kL ratio and transverse tie spacing. The specimen groups G4-G6 and G13-G15 (containing the same properties as the groups G1-G3 and G10-G12, respectively) vary solely the concrete strength (f'_c)

(selected from 20, 40 and 60 MPa). Finally, the groups G7-G9 and G16-G18 consider variation of the structural steel yield stress (f_{ys}) chosen from 250, 345 and 485 MPa. Both stub and slender concrete encased steel composite columns were investigated.

Table 5.4: Parametric variations of specimen dimensions and material properties of concrete encased steel composite columns

| Group | Parametric Columns | Concrete Section | Steel Section | | Effective Length | Stirrup Spacing | Concrete | Steel | Rebar |
|-------|--------------------|------------------|---------------------------------|----------------------|------------------|-----------------|----------|-------|-------|
| | | | $B \times D$ (mm ²) | Shape | | | | | |
| G1 | PC1 | 160 × 160 | H | 100 × 100 × 6 × 8 | 1000 | 35 | 22.5 | 304 | 376 |
| | PC2 | 160 × 160 | H | 100 × 100 × 6 × 8 | 1000 | 75 | 22.5 | 304 | 376 |
| | PC3 | 160 × 160 | H | 100 × 100 × 6 × 8 | 1000 | 140 | 22.5 | 304 | 376 |
| G2 | PC4 | 160 × 160 | H | 100 × 100 × 6 × 8 | 3500 | 35 | 22.5 | 304 | 376 |
| | PC5 | 160 × 160 | H | 100 × 100 × 6 × 8 | 3500 | 75 | 22.5 | 304 | 376 |
| | PC6 | 160 × 160 | H | 100 × 100 × 6 × 8 | 3500 | 140 | 22.5 | 304 | 376 |
| G3 | PC7 | 160 × 160 | H | 100 × 100 × 6 × 8 | 5000 | 35 | 22.5 | 304 | 376 |
| | PC8 | 160 × 160 | H | 100 × 100 × 6 × 8 | 5000 | 75 | 22.5 | 304 | 376 |
| | PC9 | 160 × 160 | H | 100 × 100 × 6 × 8 | 5000 | 140 | 22.5 | 304 | 376 |
| G4 | PC10 | 160 × 160 | H | 100 × 100 × 6 × 8 | 1000 | 140 | 20 | 304 | 376 |
| | PC11 | 160 × 160 | H | 100 × 100 × 6 × 8 | 1000 | 140 | 40 | 304 | 376 |
| | PC12 | 160 × 160 | H | 100 × 100 × 6 × 8 | 1000 | 140 | 60 | 304 | 376 |
| G5 | PC13 | 160 × 160 | H | 100 × 100 × 6 × 8 | 3500 | 140 | 20 | 304 | 376 |
| | PC14 | 160 × 160 | H | 100 × 100 × 6 × 8 | 3500 | 140 | 40 | 304 | 376 |
| | PC15 | 160 × 160 | H | 100 × 100 × 6 × 8 | 3500 | 140 | 60 | 304 | 376 |
| G6 | PC16 | 160 × 160 | H | 100 × 100 × 6 × 8 | 5000 | 140 | 20 | 304 | 376 |
| | PC17 | 160 × 160 | H | 100 × 100 × 6 × 8 | 5000 | 140 | 40 | 304 | 376 |
| | PC18 | 160 × 160 | H | 100 × 100 × 6 × 8 | 5000 | 140 | 60 | 304 | 376 |
| G7 | PC19 | 160 × 160 | H | 100 × 100 × 6 × 8 | 1000 | 140 | 22.5 | 250 | 376 |
| | PC20 | 160 × 160 | H | 100 × 100 × 6 × 8 | 1000 | 140 | 22.5 | 345 | 376 |
| | PC21 | 160 × 160 | H | 100 × 100 × 6 × 8 | 1000 | 140 | 22.5 | 485 | 376 |
| G8 | PC22 | 160 × 160 | H | 100 × 100 × 6 × 8 | 3500 | 140 | 22.5 | 250 | 376 |
| | PC23 | 160 × 160 | H | 100 × 100 × 6 × 8 | 3500 | 140 | 22.5 | 345 | 376 |
| | PC24 | 160 × 160 | H | 100 × 100 × 6 × 8 | 3500 | 140 | 22.5 | 485 | 376 |
| G9 | PC25 | 160 × 160 | H | 100 × 100 × 6 × 8 | 5000 | 140 | 22.5 | 250 | 376 |
| | PC26 | 160 × 160 | H | 100 × 100 × 6 × 8 | 5000 | 140 | 22.5 | 345 | 376 |
| | PC27 | 160 × 160 | H | 100 × 100 × 6 × 8 | 5000 | 140 | 22.5 | 485 | 350 |
| G10 | PC28 | 160 × 180 | I | 68 × 100 × 4.5 × 7.6 | 1000 | 35 | 55.7 | 379 | 358 |
| | PC29 | 160 × 180 | I | 68 × 100 × 4.5 × 7.6 | 1000 | 75 | 55.7 | 379 | 358 |
| | PC30 | 160 × 180 | I | 68 × 100 × 4.5 × 7.6 | 1000 | 140 | 55.7 | 379 | 358 |
| G11 | PC31 | 160 × 180 | I | 68 × 100 × 4.5 × 7.6 | 3500 | 35 | 55.7 | 379 | 358 |
| | PC32 | 160 × 180 | I | 68 × 100 × 4.5 × 7.6 | 3500 | 75 | 55.7 | 379 | 358 |
| | PC33 | 160 × 180 | I | 68 × 100 × 4.5 × 7.6 | 3500 | 140 | 55.7 | 379 | 358 |

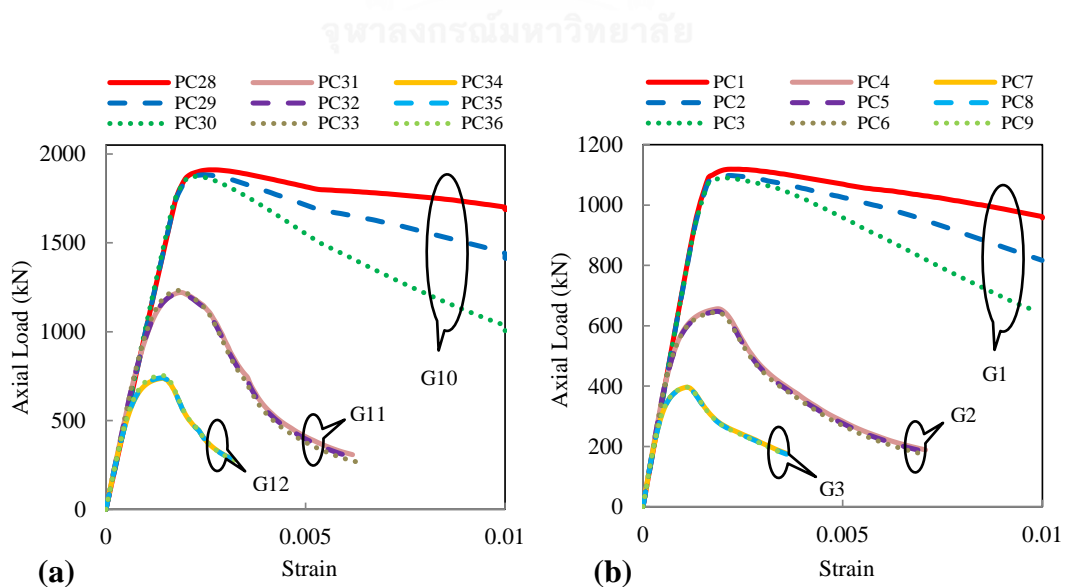
| | | | | | | | | | |
|-----|------|-----------|---|----------------------|------|-----|------|-----|-----|
| G12 | PC34 | 160 × 180 | I | 68 × 100 × 4.5 × 7.6 | 5000 | 35 | 55.7 | 379 | 358 |
| | PC35 | 160 × 180 | I | 68 × 100 × 4.5 × 7.6 | 5000 | 75 | 55.7 | 379 | 358 |
| | PC36 | 160 × 180 | I | 68 × 100 × 4.5 × 7.6 | 5000 | 140 | 55.7 | 379 | 358 |
| G13 | PC37 | 160 × 180 | I | 68 × 100 × 4.5 × 7.6 | 1000 | 150 | 20 | 379 | 358 |
| | PC38 | 160 × 180 | I | 68 × 100 × 4.5 × 7.6 | 1000 | 150 | 40 | 379 | 358 |
| | PC39 | 160 × 180 | I | 68 × 100 × 4.5 × 7.6 | 1000 | 150 | 60 | 379 | 358 |
| G14 | PC40 | 160 × 180 | I | 68 × 100 × 4.5 × 7.6 | 3500 | 150 | 20 | 379 | 358 |
| | PC41 | 160 × 180 | I | 68 × 100 × 4.5 × 7.6 | 3500 | 150 | 40 | 379 | 358 |
| | PC42 | 160 × 180 | I | 68 × 100 × 4.5 × 7.6 | 3500 | 150 | 60 | 379 | 358 |
| G15 | PC43 | 160 × 180 | I | 68 × 100 × 4.5 × 7.6 | 5000 | 150 | 20 | 379 | 358 |
| | PC44 | 160 × 180 | I | 68 × 100 × 4.5 × 7.6 | 5000 | 150 | 40 | 379 | 358 |
| | PC45 | 160 × 180 | I | 68 × 100 × 4.5 × 7.6 | 5000 | 150 | 60 | 379 | 358 |
| G16 | PC46 | 160 × 180 | I | 68 × 100 × 4.5 × 7.6 | 1000 | 150 | 55.7 | 250 | 358 |
| | PC47 | 160 × 180 | I | 68 × 100 × 4.5 × 7.6 | 1000 | 150 | 55.7 | 345 | 358 |
| | PC48 | 160 × 180 | I | 68 × 100 × 4.5 × 7.6 | 1000 | 150 | 55.7 | 485 | 358 |
| G17 | PC49 | 160 × 180 | I | 68 × 100 × 4.5 × 7.6 | 3500 | 150 | 55.7 | 250 | 358 |
| | PC50 | 160 × 180 | I | 68 × 100 × 4.5 × 7.6 | 3500 | 150 | 55.7 | 345 | 358 |
| | PC51 | 160 × 180 | I | 68 × 100 × 4.5 × 7.6 | 3500 | 150 | 55.7 | 485 | 358 |
| G18 | PC52 | 160 × 180 | I | 68 × 100 × 4.5 × 7.6 | 5000 | 150 | 55.7 | 250 | 358 |
| | PC53 | 160 × 180 | I | 68 × 100 × 4.5 × 7.6 | 5000 | 150 | 55.7 | 345 | 358 |
| | PC54 | 160 × 180 | I | 68 × 100 × 4.5 × 7.6 | 5000 | 150 | 55.7 | 485 | 358 |

5.4.2 Results and Discussions

The influences of transverse tie spacing and the B/kL ratio on the overall response of the square concrete encased H-shaped steel columns and the rectangular concrete encased I-shaped steel columns are displayed in Figure 5.8a and Figure 5.8b, respectively. As also illustrated in Table 5.5, the maximum load carrying capacity of the composite column is significantly reduced with decreasing the value of the B/kL ratio (i.e. towards the slender column). Increasing the stirrup spacing (weakening the concrete confinement) deteriorates the ductility of the stocky columns (i.e. the high value of B/kL ratio). Furthermore, the influences of the concrete confinement are less significant in the slender columns, of which the failure is governed primarily by the flexural buckling (rather than the material failure).

Table 5.5: Ultimate strength by the present analysis with parametric variations

| Group | Column (Square – H) | B/kL | Ultimate Strength (kN) | Group | Column (Rectangular – I) | B/kL | Ultimate Strength (kN) |
|-------|--------------------------|--------|---------------------------|-------|-------------------------------|--------|---------------------------|
| G1 | PC1 | 0.16 | 1119 | G10 | PC28 | 0.16 | 1911 |
| | PC2 | 0.16 | 1098 | | PC29 | 0.16 | 1883 |
| | PC3 | 0.16 | 1091 | | PC30 | 0.16 | 1873 |
| G2 | PC4 | 0.05 | 656.19 | G11 | PC31 | 0.05 | 1221 |
| | PC5 | 0.05 | 647.73 | | PC32 | 0.05 | 1217 |
| | PC6 | 0.05 | 645.56 | | PC33 | 0.05 | 1233 |
| G3 | PC7 | 0.03 | 396.37 | G12 | PC34 | 0.03 | 738.30 |
| | PC8 | 0.03 | 394.77 | | PC35 | 0.03 | 741.31 |
| | PC9 | 0.03 | 396.39 | | PC36 | 0.03 | 754.27 |
| G4 | PC10 | 0.16 | 1045 | G13 | PC37 | 0.16 | 1093 |
| | PC11 | 0.16 | 1411 | | PC38 | 0.16 | 1517 |
| | PC12 | 0.16 | 1771 | | PC39 | 0.16 | 1946 |
| G5 | PC13 | 0.05 | 608.35 | G14 | PC40 | 0.05 | 667.20 |
| | PC14 | 0.05 | 897.94 | | PC41 | 0.05 | 1000 |
| | PC15 | 0.05 | 1181 | | PC42 | 0.05 | 1337 |
| G6 | PC16 | 0.03 | 372.61 | G15 | PC43 | 0.03 | 426.97 |
| | PC17 | 0.03 | 548.89 | | PC44 | 0.03 | 634.42 |
| | PC18 | 0.03 | 697.72 | | PC45 | 0.03 | 811.38 |
| G7 | PC19 | 0.16 | 979.43 | G16 | PC46 | 0.16 | 1689 |
| | PC20 | 0.16 | 1176 | | PC47 | 0.16 | 1821 |
| | PC21 | 0.16 | 1395 | | PC48 | 0.16 | 1883 |
| G8 | PC22 | 0.05 | 636.88 | G17 | PC49 | 0.05 | 1258 |
| | PC23 | 0.05 | 645.56 | | PC50 | 0.05 | 1265 |
| | PC24 | 0.05 | 645.56 | | PC51 | 0.05 | 1265 |
| G9 | PC25 | 0.03 | 396.39 | G18 | PC52 | 0.03 | 775.86 |
| | PC26 | 0.03 | 396.39 | | PC53 | 0.03 | 775.86 |
| | PC27 | 0.03 | 396.39 | | PC54 | 0.03 | 775.86 |

**Figure 5.8:** Axial load and strain responses corresponding to variation of stirrup spacing and B/kL ratio of (a) square concrete encased H-shaped steel columns, (b) rectangular concrete encased I-shaped steel columns.

Figures 5.9a-b show the effects of concrete strength and B/kL ratio on the overall behavior of the square concrete encased H-shaped columns and the rectangular concrete encased I-shaped steel composite columns, respectively. As expected, the higher concrete strength yields the stronger load carrying capacity of the composite columns but with lower ductility.

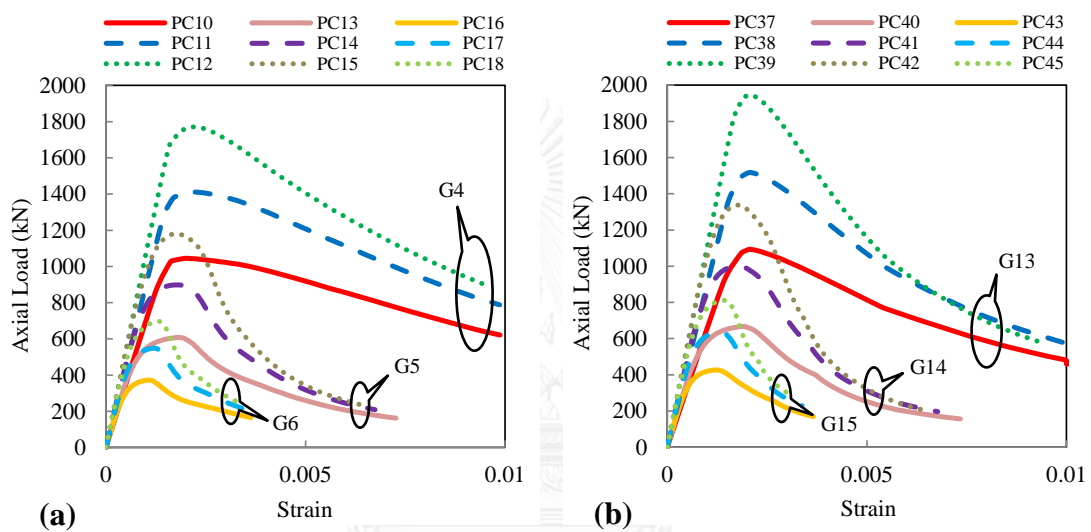


Figure 5.9: Axial load and strain responses corresponding to variation of concrete strength and B/kL ratio of (a) square concrete encased H-shaped steel columns, (b) rectangular concrete encased I-shaped steel columns.

Figures 5.10a-b consider the effects of the structural steel yield stress and the B/kL ratio for both the square concrete encased H-shaped steel columns and the rectangular concrete encased I-shaped steel columns, respectively. In particular, the higher structural steel yield stress only enhances the maximum strength capacity of the composite stub (stocky) columns (viz. containing the high value of B/kL ratio), but does not alter the overall column ductility.

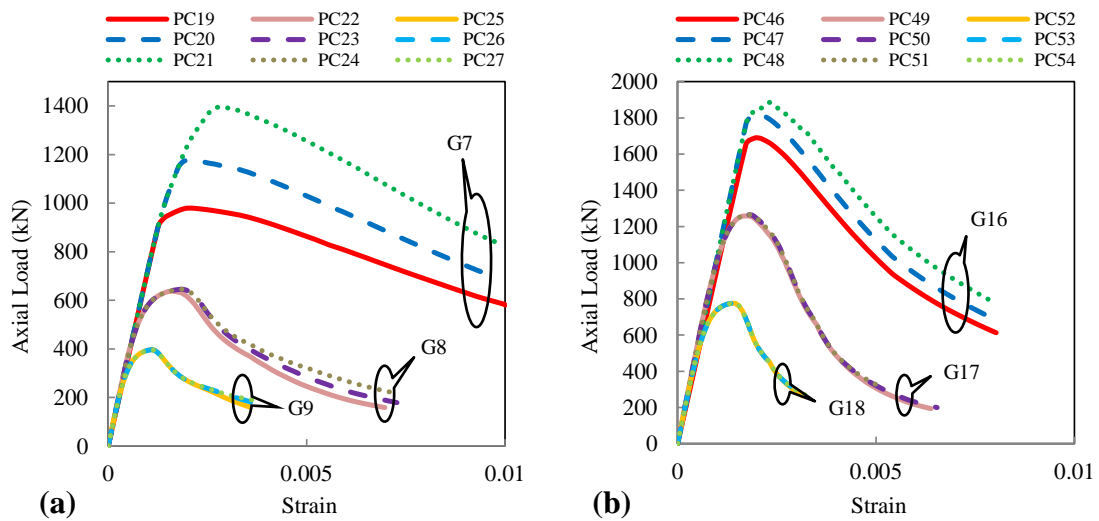


Figure 5.10: Axial load and strain responses corresponding to variation of structural steel yield stress and B/kL ratio of (a) square concrete encased H-shaped steel columns, (b) rectangular concrete encased I-shaped steel columns.

As illustrated in all Figure 5.8 to 5.10, the stub columns consisting of the high value of B/kL ratio provide the stronger capacity than the slender columns with the low value of B/kL ratio. Therefore, from this parametric study it can be summarized that the enhancement of the load carrying capacity of the concrete encased composite steel (stub and slender) columns can be achieved by increasing the concrete strength, which however deteriorates the ductility. For the stub composite columns, the reduction of the stirrup spacing enhances the concrete confinement and thus the ductility, whilst the increase of the structural steel yield stress only yields the better column strength.

5.5 Concluding Remarks

The simple inelastic analysis approach has been presented to efficiently map out the complete response of the concrete encased steel composite columns under a concentrically applied axial force. The maximum strength capacity of the columns can

be obtained as a by-product. What is important is the proposed analysis scheme is able to realistically accommodate the influences of various difficult physical and material phenomena underpinning the intrinsic behavior of the composite columns as strain hardening/softening of structural steel and concrete materials, concrete confinement, local buckling of structural steel and reinforcement bars, and initial geometric imperfection, simultaneously. Both stub and slender composite columns have been investigated.

The proposed analysis approach suitably discretizes the structural steel, reinforcement bars and concrete cross-section taking into account of three different (namely unconfined, partially confined, highly confined) confinement regions using the fiber element model. Confinement zones have been carefully defined and verified through the comparison with experimental results. The iterative Müller's method has been adopted to enforce equilibrium of the composite column, in conjunction with the additional adaptive technique proposed to enhance the solution convergence. Good agreements between the complete response (and maximum strength) obtained by the present analysis scheme and the associated 33 experimental results of the composite columns have been evidenced, and thus validate the accuracy of the proposed method.

The influences of various key parameters (e.g. width-to-effective length ratio, transverse tie spacing, concrete strength and structural steel yield stress) on the overall behavior and maximum strength of both the square concrete encased H-shaped steel columns and the rectangular concrete encased I-shaped steel columns have been studied using the proposed analysis procedure. This can be concluded as follows. Firstly, though increasing the concrete strength improves the load carrying capacity of the composite columns, it unfortunately deteriorates the column ductility. Secondly,

the slender columns (i.e. having the smaller value of the width-to-effective length ratio) are weaker than the stub columns. Thirdly, the better concrete confinement given by the closer stirrup spacing yields the more superior ductility only for the stub composite columns. Finally, the higher structural steel yield stress solely strengthens the maximum load carrying capacity of the stocky columns.



CHAPTER 6

CONCRETE ENCASED STEEL COLUMNS UNDER COMBINED AXIAL COMPRESSION AND UNIAXIAL BENDING

6.1 Introduction

Columns subjected to combined axial compression and bending are commonly known as beam-columns. The important effects in structural design, viz. steel and steel-concrete composite, involving stability problem are compulsory to be included in structural analysis and design by most specifications. Common indispensable criteria in most design codes are to account for second-order effects, geometric imperfection, and inelasticity. This chapter presents a nonlinear (viz. material and geometry) inelastic analysis of concrete encased steel beam-columns with uniaxial bending. The proposed approach accommodates various important influences, i.e. levels of concrete confinement, initial geometric imperfection, geometry nonlinearity, material nonlinearity, buckling of reinforcement bars and local buckling of structural steel, simultaneously. Both the ultimate capacity and the complete nonlinear responses of CES beam-columns can be fully simulated. The numerical scheme is capable of generating importance outputs such as the nonlinear load and deflection response including sophisticated post-peak softening, axial load and inelastic shortening response, nonlinear interaction force and bending moment diagram, and moment and curvature curve. The predicted ultimate strength as well as complete nonlinear axial load and lateral deflection response of CES beam-columns are

validated against various experimental results and also compared with previous researchers of different approaches. Finally, parametric sensitivity analyzes are performed to study various influences of key parameters such as eccentricity ratios, effective length ratio, concrete strength and structural steel yield stress on the behaviors of CES beam-columns.

6.2 Geometrically Nonlinear Analysis of CES Beam-Columns

6.2.1 Eccentric Load and Buckling Modeling of Beam-Columns

The deflection shape of a pin-ended concrete encased steel composite column subjected to eccentric load with initial geometric imperfection (see Figure 6.1) can be predicted as part of a sine wave equation (Shakir-Khalil and Zeghiche 1989) as expressed below.

$$\delta(z) = \delta_{mi} \sin\left(\frac{\pi z}{L}\right) \quad (6.1)$$

where δ is the lateral displacement at any point along the length of the column, L the effective length, δ_{mi} the lateral deflection at the column mid-height, z the longitudinal direction of the column.

The column curvature can then be determined from the lateral displacement:

$$\phi(z) = \frac{\partial^2 \delta(z)}{\partial z^2} = \left(\frac{\pi}{L}\right)^2 \delta_{mi} \sin\left(\frac{\pi z}{L}\right) \quad (6.2)$$

From which the curvature of the column at the mid-height of the column is

$$\phi_{mi} = \left(\frac{\pi}{L}\right)^2 \delta_{mi} \quad (6.3)$$

The total external bending moment at the column mid-height under axial compressive load with eccentricity and initial imperfection yields

$$M_{e,mi} = P(e + \delta_{im} + \delta_{mi}) \quad (6.4)$$

where δ_{im} is the initial geometric imperfection, and e the eccentricity of applied load.

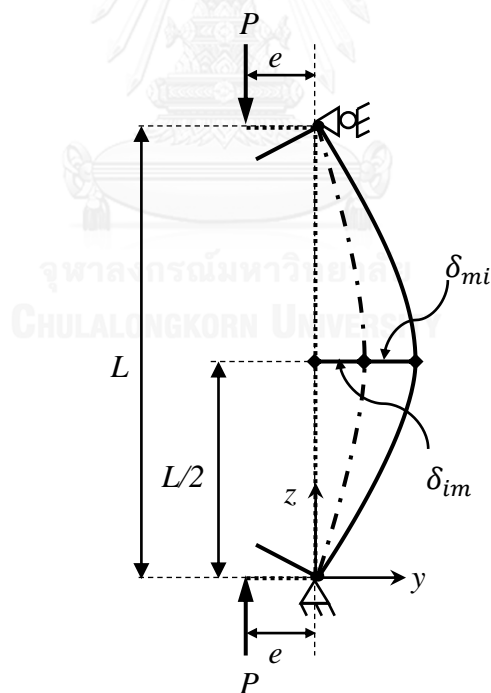


Figure 6.1: Force and deformations in pin-ended beam-column model with initial imperfection.

6.2.2 Numerical Method for Nonlinear Analysis

To solve for the neutral axis depth using fiber element analysis, many researchers adopted various numerical methods such as bisection method, quasi-Newton method (Yen 1991), quasi-Newton method within the Regular-Falsi numerical scheme (Chen et al. 2001), secant method (Liang 2009, 2011), and Müller's method (Patel et al. 2012). The bisection method has a weakness due to very slow convergence rate and hence it is not efficient. The secant method has been implemented in the performance-based analysis program to carry out the nonlinear analysis of the thin-walled concrete filled steel tube beam-columns. The Müller's method (Müller 1956), which is the generalized approach of the secant method, uses a quadratic 3-point instead of using a linear 2-point interpolation as in the secant method. The order of convergence of the Müller's method is approximately 1.84 while only 1.62 of the secant method. In the present nonlinear analysis scheme, the Müller's numerical method is implemented to solve for the neutral axis depth which satisfies the equilibriums.

The present approach requires three neutral axis depths as initial values for the Müller's method to approximate the next neutral axis depth which satisfies the equilibriums. The external moments, resulting from the initial geometric imperfection and the lateral displacement at the mid-height of the column under the axial load, must be in equilibrium with the internal moment. From a set of the initial neutral axis depths $(d_{n,1}, d_{n,2}, d_{n,3})$, the next neutral axis depth is determined by:

$$f_m = P(e + \delta_{im} + \delta_{mi}) - M_{mi} \quad (6.5)$$

$$A = \frac{(d_{n,2} - d_{n,3})(f_{m,1} - f_{m,3}) - (d_{n,1} - d_{n,3})(f_{m,2} - f_{m,3})}{(d_{n,1} - d_{n,2})(d_{n,2} - d_{n,3})(d_{n,1} - d_{n,3})} \quad (6.6)$$

$$B = \frac{(d_{n,1} - d_{n,3})^2(f_{m,2} - f_{m,3}) - (d_{n,2} - d_{n,3})^2(f_{m,1} - f_{m,3})}{(d_{n,1} - d_{n,2})(d_{n,2} - d_{n,3})(d_{n,1} - d_{n,3})} \quad (6.7)$$

$$C = f_{m,3} \quad (6.8)$$

$$d_{n,4} = d_{n,3} - \frac{2C}{B \pm \sqrt{B^2 - 4AC}} \quad (6.9)$$

where f_m is the Müller's function of the residual moment at the column mid-height, δ_{im} the initial geometric imperfection of the column, i.e. $L/2000$ (Ellobody and Young 2011, Ellobody et al. 2011), M_{mi} the internal bending moment of the composite cross-section, A, B, C the coefficients of the Müller's parabolic equation.

Equation 6.9 yields two roots which correspond to the sign \pm in the denominator. The sign of the square root is taken to be the same as the sign of B . The purpose of choosing the sign plus or minus is to obtain the result which produces the largest denominator, consequently it gives $d_{n,4}$ which is close to $d_{n,3}$. Thus, the values of $d_{n,1}, d_{n,2}, d_{n,3}$ with the corresponding functions $f_{m,1}, f_{m,2}, f_{m,3}$ need to be exchanged accordingly using Equation 5.10-5.11. The Müller's iterations are repeated until the specified tolerance (ε_{tol}) satisfies the convergence condition of $|f_m| \leq \varepsilon_{tol}$ which is set to 0.0001 in this study.

The initial guesses ($d_{n,1}, d_{n,2}, d_{n,3}$) are important to obtain the solution convergence of the numerical analysis. The adaptive technique is implemented to provide the efficient initial values of the neutral axis depth. The initial neutral axis depths are chosen as ($D/4, D/2, 2D/3$) when the neutral axis is less than 80 percent of the cross-section mid-depth, and ($D/4, D/2, D$) when the neutral axis reaches 80 percent of the cross-section mid-depth.

6.2.3 Computational Procedures for Load and Lateral Deflection Responses

To obtain the full nonlinear behavior of the concrete encased steel composite column under eccentric compressive load with initial geometric imperfection, the lateral displacement at the column mid-height is initially imposed in the nonlinear inelastic fiber element analysis. As the lateral deflection δ_{mi} at the column mid-height is incrementally increased, the curvature ϕ_{mi} of the column can then be determined. Knowing the curvature, strains at the centroid of each fiber element in the composite cross-section are calculated from Equations 4.1 and 4.4. Stresses in the unconfined, partially confined, highly confined concrete, structural steel, and reinforcement bars are determined from the uniaxial stress-strain relationships of each material accordingly. For each imposed lateral deflection, the depth of neutral axis is adjusted using the Müller's method to satisfy the moment equilibrium at the column mid-height. The analysis procedure is then repeated with the successive increment of the mid-height lateral deflection to obtain the full axial load and lateral deflection nonlinear response. Critical behaviors (e.g. initial stiffness, maximum strength capacity, post-peak softening response and ductility) of the concrete encased steel composite beam-columns under the full history of the eccentric load with the initial

geometric imperfection can be identified directly from the resulting axial load and deflection curve.

The step-by-step procedures and the flowchart (see Figure 6.2) of the nonlinear inelastic analysis program of the concrete encased steel composite beam-columns under eccentric load with initial geometric imperfection are summarized below:

1. Input the dimensions, eccentricity and the initial geometric imperfection of the concrete encased steel composite column.
2. Define the zones of the unconfined concrete, partially confined concrete, highly confined concrete.
3. Impose the stopping criteria by specifying the maximum axial load P_{max} , the limit deflection δ_{limit} , the convergence tolerances ε_{tol} , ε_d .
4. Define the material constitutive models for the unconfined concrete, partially confined concrete, highly confined concrete, structural steel, and reinforcement bar.
5. Discretize the composite cross-section into fiber elements.
6. Impose the initial lateral deflection δ_{mi} at the mid-height of the column by an increment of $\Delta\delta_{mi}$.
7. Determine the mid-height curvature ϕ_{mi} from the imposed lateral deflection δ_{mi} at the mid-height of the column.
8. Choose the initial guessing values of the neutral axis depth $d_{n,1}$, $d_{n,2}$, $d_{n,3}$ as $D/4$, $D/2$, $2D/3$, respectively. These initial values shall be chosen using the proposed adaptive technique.

9. Using the chosen initial values of the neutral axis depth $d_{n,1}, d_{n,2}, d_{n,3}$ to compute the fiber strains of each material.
10. Calculate the fiber stresses of the unconfined concrete, partially confined concrete, highly confined concrete, structural steel, and reinforcement bar from the uniaxial stress-strain relationships accordingly.
11. Calculate the internal axial force P and the internal bending moment M_{mi} carried by the composite column, and the external bending moment $M_{e,mi}$ corresponding to the initial guessing values.
12. Determine the Müller's function of the residual moments $f_{m,1}, f_{m,2}, f_{m,3}$ at the mid-height of the composite column corresponding to the initial values of the neutral axis depths $d_{n,1}, d_{n,2}, d_{n,3}$.
13. Compute the coefficients A, B, C and the adjusted neutral axis depth $d_{n,4}$ using Müller's numerical method.
14. Compute the strains and stresses of the each fiber element corresponding to the adjusted neutral axis depth $d_{n,4}$ from the material uniaxial stress-strain relationships.
15. Calculate the internal axial force P and the internal bending moment M_{mi} carried by the composite column, and the external bending moment $M_{e,mi}$ corresponding to the adjusted neutral axis depth $d_{n,4}$.
16. Calculate the residual moment $f_{m,4}$ of the Müller's function.
17. Check the conditions using Equations 5.10-5.11 for the interchanged values of $d_{n,1}, d_{n,2}, d_{n,3}$ along with the corresponding residual moments $f_{m,1}, f_{m,2}, f_{m,3}$.

18. Check the convergence condition $|f_m| \leq \varepsilon_{tot}$. If the convergence condition is satisfied, proceed to the next step. Otherwise, repeat from step (14) to (18).
 19. Increase the mid-height lateral deflection, $\delta_{mi} = \delta_{mi} + \Delta\delta_{mi}$. Repeat from step (6) to (19) until the imposed stopping criteria in step (3) is reached.
- Generate the load-deflection ($P - \delta$) curve.



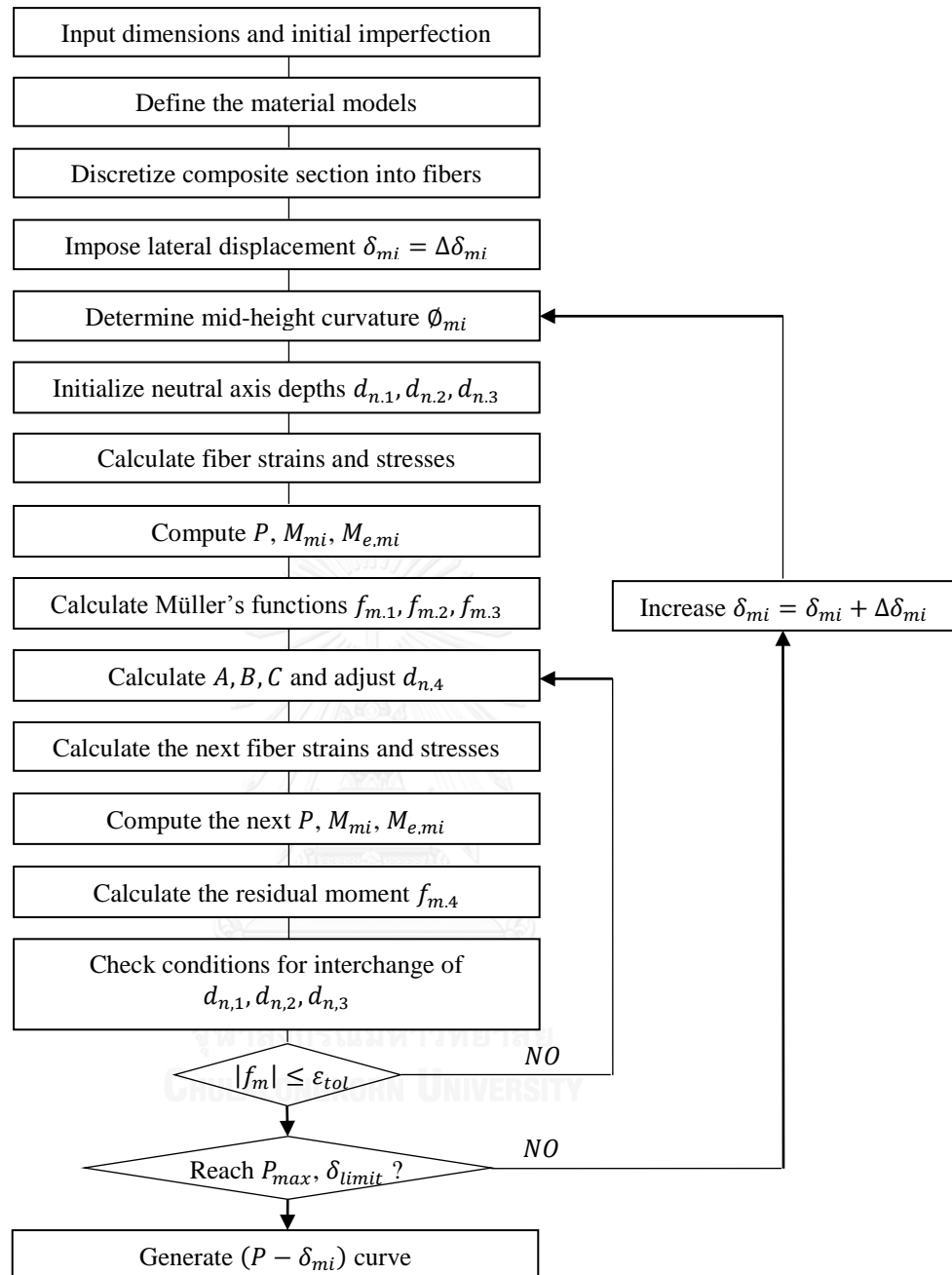


Figure 6.2: Flowchart for determining axial load and deflection responses of concrete encased steel composite beam-columns.

6.3 Validation of the Numerical Approach

6.3.1 Summary of Relevant Experimental Tests

The present numerical approach has been validated against the relevant full-scale experimental tests conducted by Morino et al. (1984), Mirza et al. (1996), Al-Shahari et al. (2003), and Zhao et al. (2005). The detail of dimensions, material properties, and cross-section configurations of all the composite column specimens used for comparison are shown in Tables 6.1 and 6.2.

Table 6.1: Specimen dimensions and material properties of CES beam-columns

| Specimen ID | Dimensions | | | Structural steel section | | e/D | Material Properties | | | Reference | |
|-------------|------------|--------|---------|--------------------------|------------------------------------|----------------------|---------------------|-------------|-------------|-----------|--------------------------|
| | B (mm) | D (mm) | kL (mm) | Shape | $b \times d \times t_w \times t_f$ | | Concrete (MPa) | Steel (MPa) | Rebar (MPa) | | |
| BC1 | 230 | 230 | 2000 | H | | 100 x 96 x 5 x 8 | 0.3 | 20.5 | 337 | 459 | Al-Shahari et al. (2003) |
| BC2 | 230 | 230 | 2000 | H | | 100 x 96 x 5 x 8 | 0.3 | 13.7 | 337 | 459 | |
| BC3 | 230 | 230 | 2000 | H | | 140 x 133 x 5 x 8 | 0.3 | 20.5 | 307 | 459 | |
| BC4 | 230 | 230 | 2000 | H | | 140 x 133 x 5 x 8 | 0.3 | 28.2 | 307 | 459 | |
| BC5 | 230 | 230 | 3000 | H | | 140 x 133 x 5 x 8 | 0.3 | 28.2 | 307 | 459 | |
| BC6 | 230 | 230 | 3000 | H | | 100 x 96 x 5 x 8 | 0.17 | 20.5 | 337 | 459 | |
| BC7 | 230 | 230 | 3000 | H | | 100 x 96 x 5 x 8 | 0.17 | 13.7 | 337 | 459 | |
| BC8 | 160 | 160 | 960 | H | | 100 x 100 x 6 x 8 | 0.25 | 21.1 | 345 | 460 | Morino et al. (1984) |
| BC9 | 160 | 160 | 2400 | H | | 100 x 100 x 6 x 8 | 0.25 | 23.4 | 345 | 460 | |
| BC10 | 160 | 160 | 3600 | H | | 100 x 100 x 6 x 8 | 0.25 | 23.3 | 345 | 460 | |
| BC11 | 240 | 240 | 4000 | H | | 100 x 96 x 5.1 x 8.6 | 0.17 | 27.4 | 311.2 | 634 | Mirza et al. (1996) |
| BC12 | 240 | 240 | 4000 | H | | 100 x 96 x 5.1 x 8.6 | 0.25 | 27.4 | 311.2 | 634 | |
| BC13 | 240 | 240 | 4000 | H | | 100 x 96 x 5.1 x 8.6 | 0.41 | 25.5 | 311.2 | 634 | |
| BC14 | 240 | 240 | 4000 | H | | 100 x 96 x 5.1 x 8.6 | 0.86 | 25.5 | 311.2 | 634 | |
| BC15 | 240 | 240 | 4000 | H | | 100 x 96 x 5.1 x 8.6 | 2.58 | 25.5 | 311.2 | 634 | |
| BC16 | 160 | 180 | 3200 | I | | 68 x 100 x 4.5 x 7.6 | 0.22 | 46.6 | 379 | 358 | Zhao et al. (2005) |
| BC17 | 160 | 180 | 3200 | I | | 68 x 100 x 4.5 x 7.6 | 0.17 | 43.3 | 379 | 358 | |

Table 6.2: Detailed section dimensions and reinforcement of CES beam-columns

| Specimen ID | Steel Concrete Composite Dimensions | | | | | | Reinforcements | | | | Reference |
|-------------|-------------------------------------|------------------------|------------------------|------------------------|------------------------|------------------------|----------------|----|---------|---|--------------------------|
| | b ₁ (mm) | b ₂ (mm) | b ₃ (mm) | d ₁ (mm) | d ₂ (mm) | d ₃ (mm) | Main bar | | Stirrup | | |
| | | | | | | | Number | Ø | Spacing | Ø | |
| BC1 | 35 | 65 | 100 | 35 | 67 | 96 | 4 | 12 | 140 | 8 | Al-Shahari et al. (2003) |
| BC2 | 35 | 65 | 100 | 35 | 67 | 96 | 4 | 12 | 140 | 8 | |
| BC3 | 35 | 45 | 140 | 35 | 48.5 | 133 | 4 | 12 | 140 | 8 | |
| BC4 | 35 | 45 | 140 | 35 | 48.5 | 133 | 4 | 12 | 140 | 8 | |
| BC5 | 35 | 45 | 140 | 35 | 48.5 | 133 | 4 | 12 | 140 | 8 | |
| BC6 | 35 | 65 | 100 | 35 | 67 | 96 | 4 | 12 | 140 | 8 | |
| BC7 | 35 | 65 | 100 | 35 | 67 | 96 | 4 | 12 | 140 | 8 | |
| BC8 | 19 | 30 | 100 | 19 | 30 | 100 | 4 | 6 | 75 | 4 | Morino et al. (1984) |
| BC9 | 19 | 30 | 100 | 19 | 30 | 100 | 4 | 6 | 75 | 4 | |
| BC10 | 19 | 30 | 100 | 19 | 30 | 100 | 4 | 6 | 75 | 4 | |
| BC11 | 38 | 70 | 96 | 38 | 72 | 100 | 4 | 10 | 150 | 6 | Mirza et al. (1996) |
| BC12 | 38 | 70 | 96 | 38 | 72 | 100 | 4 | 10 | 150 | 6 | |
| BC13 | 38 | 70 | 96 | 38 | 72 | 100 | 4 | 10 | 150 | 6 | |
| BC14 | 38 | 70 | 96 | 38 | 72 | 100 | 4 | 10 | 150 | 6 | |
| BC15 | 38 | 70 | 96 | 38 | 72 | 100 | 4 | 10 | 150 | 6 | |
| BC16 | 15 | 46 | 68 | 15 | 40 | 100 | 4 | 12 | 150 | 6 | Zhao et al. (2005) |
| BC17 | 15 | 46 | 68 | 15 | 40 | 100 | 4 | 12 | 150 | 6 | |

All the beam-column specimens were H-shaped and I-shaped steel section encased in concrete (cube strength) with four longitudinal reinforcement bars at the corners as shown in Figure 6.3. The standard cylinder concrete strength is taken as 0.8 of the standard cube strength. From the sixteen full-scale tests conducted by Al-Shahari et al. (2003), nine CES specimens in lightweight aggregate concrete, three CES specimens in normal concrete, and four bare steel columns were full-scale pin-ended beam-columns subjected to eccentric compressive load in the major axis

bending in single curvature. Seven CES beam-column specimens BC1-BC7, having H-shaped cross-sections, are employed in this study.

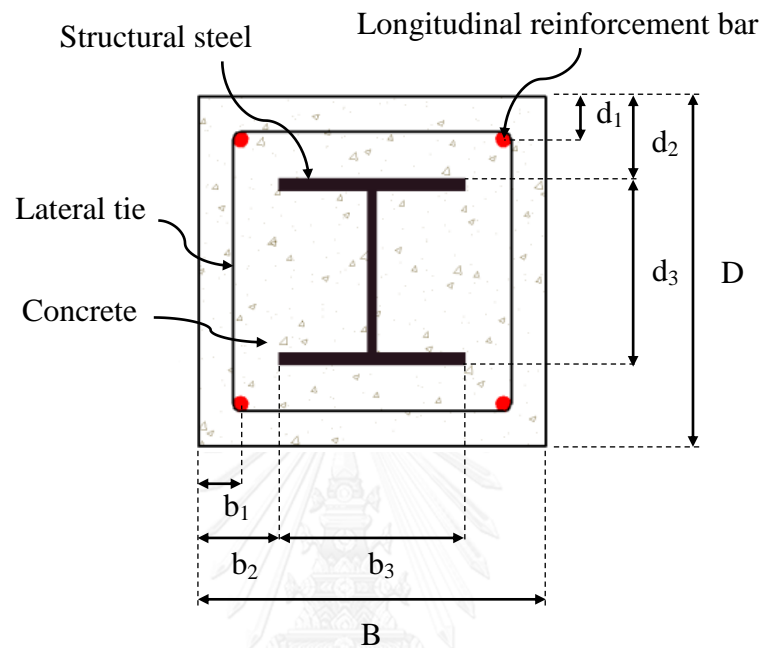


Figure 6.3: Cross-section configurations of concrete encased steel beam-columns.

Similarly, three H-shaped steel encased column specimens from Morino et al. (1984) is chosen and denoted as BC8-BC10. Furthermore, Mirza et al. (1996) conducted a series of tests on the concrete H-shaped encased steel composite beam-columns using high-strength reinforcement bars of 634 MPa, where five specimens are denoted as BC11-BC15 in this study. Finally, eight specimens in the experimental studies were performed by Zhao et al. (2005) on the slender concrete encased I-shaped steel composite columns using high-strength concrete. However, only two specimens BC16, BC17 were loaded with eccentricity; which is employed here for validation.

6.3.2 Comparison between the numerical and experimental results

The ultimate capacity as well as the load and deflection nonlinear response measured from the tests (Morino et al. 1984, Mirza et al. 1996, Al-Shahari et al. 2003, Zhao et al. 2005) are compared with those generated from the current developed numerical scheme, and at the same time shows the results from previous researchers (Mirza et al. 1996, Zhao et al. 2005, Ellobody et al. 2011). Table 6.3 summarizes the ultimate load-carrying capacity of the concrete encased steel composite columns generated from the proposed analysis approach (P_{Prop}), previous researchers ($P_{FE.1}$, $P_{FE.2}$, P_{Zhao}), and experimental tests (P_{Test}). Evidently, good agreements between P_{Prop} and P_{Test} have been achieved, in which the average value, the standard deviation (SD) and the coefficient of variation (COV) of the P_{Prop} / P_{Test} ratio are 0.95, 0.06 and 0.06, respectively.

Table 6.3: Comparison between numerical approach with tests and previous researchers

| Specimen ID | Test | FE.1 | FE.2 | (Zhao et al.) | Proposed Model | $\frac{P_{FE.1}}{P_{Test}}$ | $\frac{P_{FE.2}}{P_{Test}}$ | $\frac{P_{Zhao}}{P_{Test}}$ | $\frac{P_{Prop}}{P_{Test}}$ | Reference |
|-------------|-----------------|-----------------|-----------------|-----------------|-----------------|-----------------------------|-----------------------------|-----------------------------|-----------------------------|--------------------------|
| | P_{Test} (kN) | $P_{FE.1}$ (kN) | $P_{FE.2}$ (kN) | P_{Zhao} (kN) | P_{Prop} (kN) | | | | | |
| BC1 | 654 | 601 | - | - | 658.21 | 0.92 | - | - | 1.00 | Al-Shahari et al. (2003) |
| BC2 | 558 | 511 | - | - | 554.55 | 0.92 | - | - | 1.00 | |
| BC3 | 962 | 827 | - | - | 825.71 | 0.86 | - | - | 0.86 | |
| BC4 | 949 | 946 | - | - | 942.13 | 1.00 | - | - | 0.99 | |
| BC5 | 900 | 822 | - | - | 864.81 | 0.91 | - | - | 0.96 | |
| BC6 | 813 | 684 | - | - | 820.43 | 0.84 | - | - | 1.01 | |
| BC7 | 704 | 583 | - | - | 680.07 | 0.83 | - | - | 0.97 | |
| BC8 | 740 | 660 | - | - | 595.70 | 0.89 | - | - | 0.81 | Morino et al. (1984) |
| BC9 | 504 | 530 | - | - | 515.26 | 1.05 | - | - | 1.02 | |
| BC10 | 412 | 406 | - | - | 404.68 | 0.99 | - | - | 0.98 | |

| | | | | | | | | | | |
|---------|-----|---|-------|-----|--------|---|------|------|------|---------------------|
| BC11 | 927 | - | 980.6 | - | 912.89 | - | 1.06 | - | 0.99 | Mirza et al. (1996) |
| BC12 | 720 | - | 782.7 | - | 702.95 | - | 1.09 | - | 0.98 | |
| BC13 | 540 | - | 548.1 | - | 479.39 | - | 1.02 | - | 0.89 | |
| BC14 | 296 | - | 295.2 | - | 270.13 | - | 1.00 | - | 0.91 | |
| BC15 | 100 | - | 100.7 | - | 94.35 | - | 1.00 | - | 0.94 | |
| BC16 | 678 | - | - | 647 | 654.73 | - | - | 0.95 | 0.97 | Zhao et al. (2005) |
| BC17 | 820 | - | - | 739 | 739.99 | - | - | 0.90 | 0.90 | |
| Average | - | - | - | - | - | - | - | - | 0.95 | - |
| SD | - | - | - | - | - | - | - | - | 0.06 | - |
| COV | - | - | - | - | - | - | - | - | 0.06 | - |

Moreover, the complete nonlinear axial load and deflection responses of the concrete encased steel composite columns under eccentric compressive load have been fully traced with good agreements with experimental data plots. One of the most common issues in the numerical approach is to predict the post-peak response. Again, in the present numerical scheme, the post-peak response is well established as shown in Figures 6.4, 6.5 for the specimens BC4 and BC5, respectively.

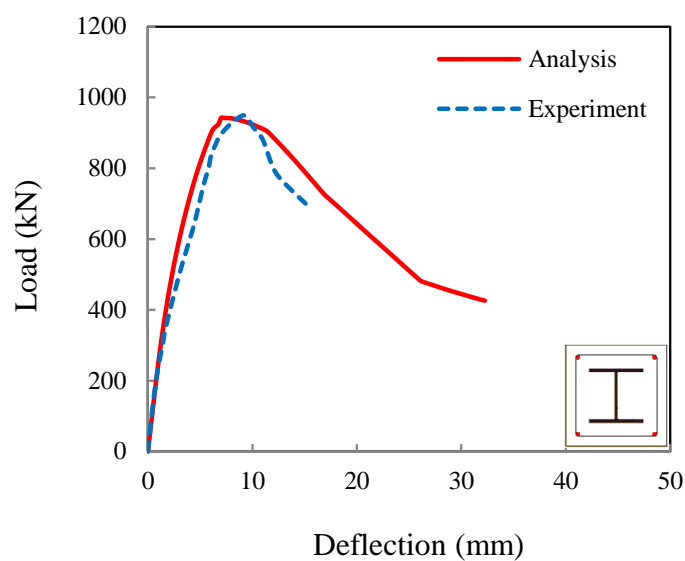


Figure 6.4: Comparison between numerical and experimental nonlinear load-deflection response for specimen BC4.

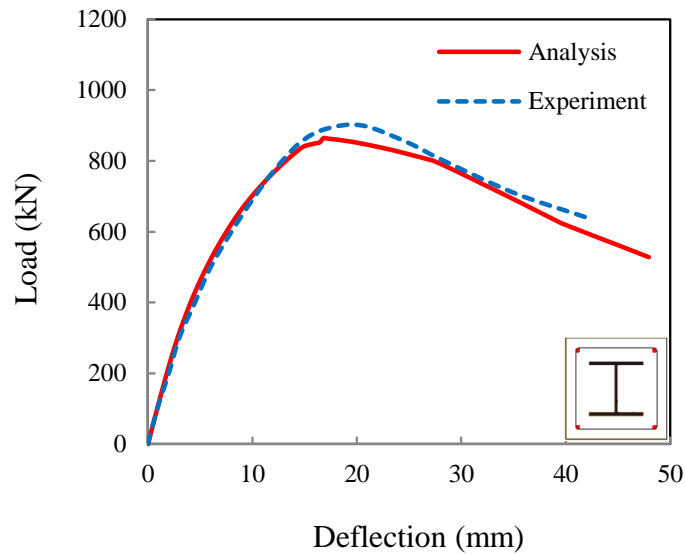


Figure 6.5: Comparison between numerical and experimental nonlinear load-deflection response for specimen BC5.

It is evident that the full deflection responses have been efficiently mapped out using the present nonlinear inelastic fiber element analysis approach, which incorporates the initial geometric imperfection, second order P-delta effect, inelastic buckling of structural steel and reinforcement bars, constitutive models of unconfined concrete, partially confined concrete, and highly confined concrete, simultaneously.

6.4 Parametric Sensitivity Analyses

6.4.1 Description of Parameters

The verified nonlinear inelastic analysis approach is used in the parametric study to investigate the influences of the eccentricity ratio (e/D), effective length ratio (D/kL), concrete strength (f'_c) and structural steel yield stress (f_{ys}) on the overall response and maximum strength of the concrete encased steel composite beam-columns. A total of 27 eccentrically loaded parametric columns are carefully selected where their dimensions and materials properties are summarized in Table 6.4. The

parametric beam-columns are divided into 9 groups (G1–G9), where the D/kL ratio is varied within the range of 0.058 to 0.23. Both stub and slender concrete encased steel composite beam-columns are thus investigated.

All specimen groups are chosen similarly to BC1, which was previously tested (Al-Shahari et al. 2003), by changing only the key parameters. The composite beam-columns have square concrete cross-section of (230×230) encasing H-shaped structural steel section (100×96×5×8) with four longitudinal reinforcement bars of 12 mm in diameter, and lateral tie diameter of 8 mm (see Figure 6.3). The column specimen groups (G1–G3) use the same concrete cube strength (f'_c), steel yield stress (f_{ys}), and reinforcement bars yield stress (f_{yr}) as in the tests [10]. And the specimen (viz. having the cross-sectional properties of BC1 with kL of 1000 mm, 2500 mm, and 4000 mm) is used to plot the interaction curves of P - M , P - e/D , and M - e/D for the study of the influence from the effective length kL . The present study varies the parameter D/kL ratio for each variation of e/D to investigate the axial load and deflection response. Again, the specimen groups (G4–G6) have the same properties as in BC1, only the concrete strengths (f'_c) are selected from 20 MPa, 40 MPa, and 60 MPa for each D/kL ratio. In essence, the beam-column BC1 of 1000 mm is used to plot the interaction curves of P - M , P - e/D , and M - e/D to illustrate the effect of concrete strength. Lastly, the groups G7-G9 consider the variation of structural steel yield stress (f_{ys}) which is chosen from 250 MPa, 345 MPa and 485 MPa for each D/kL ratio. Similarly, the specimen BC1 of 1000 mm is used to plot the interaction curves of P - M , P - e/D , and M - e/D to investigate the domination of the structural steel yield stress.

Table 6.4: Dimensions and material properties of CES parametric beam-columns.

| Group | Parametric Column | Concrete Section B x D (mm) | Steel Section | | Effective Length kL (mm) | e/D | Concrete f'_c (MPa) | Steel f_{ys} (MPa) | Rebar f_{yr} (MPa) |
|-------|-------------------|--------------------------------|---------------|------------------------------------|-----------------------------|-------|-----------------------------|----------------------------|----------------------------|
| | | | Shape | $b \times d \times t_w \times t_f$ | | | | | |
| G1 | PC1 | 230 x 230 | H | 100 x 96 x 5 x 8 | 1000 | 0.125 | 20.5 | 337 | 459 |
| | PC2 | 230 x 230 | H | 100 x 96 x 5 x 8 | 1000 | 0.25 | 20.5 | 337 | 459 |
| | PC3 | 230 x 230 | H | 100 x 96 x 5 x 8 | 1000 | 0.375 | 20.5 | 337 | 459 |
| G2 | PC4 | 230 x 230 | H | 100 x 96 x 5 x 8 | 2500 | 0.125 | 20.5 | 337 | 459 |
| | PC5 | 230 x 230 | H | 100 x 96 x 5 x 8 | 2500 | 0.25 | 20.5 | 337 | 459 |
| | PC6 | 230 x 230 | H | 100 x 96 x 5 x 8 | 2500 | 0.375 | 20.5 | 337 | 459 |
| G3 | PC7 | 230 x 230 | H | 100 x 96 x 5 x 8 | 4000 | 0.125 | 20.5 | 337 | 459 |
| | PC8 | 230 x 230 | H | 100 x 96 x 5 x 8 | 4000 | 0.25 | 20.5 | 337 | 459 |
| | PC9 | 230 x 230 | H | 100 x 96 x 5 x 8 | 4000 | 0.375 | 20.5 | 337 | 459 |
| G4 | PC10 | 230 x 230 | H | 100 x 96 x 5 x 8 | 1000 | 0.3 | 20 | 337 | 459 |
| | PC11 | 230 x 230 | H | 100 x 96 x 5 x 8 | 1000 | 0.3 | 40 | 337 | 459 |
| | PC12 | 230 x 230 | H | 100 x 96 x 5 x 8 | 1000 | 0.3 | 60 | 337 | 459 |
| G5 | PC13 | 230 x 230 | H | 100 x 96 x 5 x 8 | 2500 | 0.3 | 20 | 337 | 459 |
| | PC14 | 230 x 230 | H | 100 x 96 x 5 x 8 | 2500 | 0.3 | 40 | 337 | 459 |
| | PC15 | 230 x 230 | H | 100 x 96 x 5 x 8 | 2500 | 0.3 | 60 | 337 | 459 |
| G6 | PC16 | 230 x 230 | H | 100 x 96 x 5 x 8 | 4000 | 0.3 | 20 | 337 | 459 |
| | PC17 | 230 x 230 | H | 100 x 96 x 5 x 8 | 4000 | 0.3 | 40 | 337 | 459 |
| | PC18 | 230 x 230 | H | 100 x 96 x 5 x 8 | 4000 | 0.3 | 60 | 337 | 459 |
| G7 | PC19 | 230 x 230 | H | 100 x 96 x 5 x 8 | 1000 | 0.3 | 20.5 | 250 | 459 |
| | PC20 | 230 x 230 | H | 100 x 96 x 5 x 8 | 1000 | 0.3 | 20.5 | 345 | 459 |
| | PC21 | 230 x 230 | H | 100 x 96 x 5 x 8 | 1000 | 0.3 | 20.5 | 485 | 459 |
| G8 | PC22 | 230 x 230 | H | 100 x 96 x 5 x 8 | 2500 | 0.3 | 20.5 | 250 | 459 |
| | PC23 | 230 x 230 | H | 100 x 96 x 5 x 8 | 2500 | 0.3 | 20.5 | 345 | 459 |
| | PC24 | 230 x 230 | H | 100 x 96 x 5 x 8 | 2500 | 0.3 | 20.5 | 485 | 459 |
| G9 | PC25 | 230 x 230 | H | 100 x 96 x 5 x 8 | 4000 | 0.3 | 20.5 | 250 | 459 |
| | PC26 | 230 x 230 | H | 100 x 96 x 5 x 8 | 4000 | 0.3 | 20.5 | 345 | 459 |
| | PC27 | 230 x 230 | H | 100 x 96 x 5 x 8 | 4000 | 0.3 | 20.5 | 485 | 459 |

6.4.2 Effects of eccentricity ratios with different effective length ratios

The eccentricity ratio (e/D) provokes significant influences between the stub and slender columns on the axial load and deflection response of the concrete encased steel composite beam-columns. Thus, it is important to plot the effect of e/D ratios with D/kL ratios as shown in Figure 6.6. It can be observed that increasing the eccentricity ratio reduces the axial load capacity of the composite columns as illustrated in Table 6.5. The columns with small value of D/kL (i.e. towards the slender column) are even more ductile than those of large D/kL (i.e. towards the stocky column). Similarly, the columns subjected to large e/D ratios are more ductile than those with small e/D ratios. Figure 6.7 shows the interaction diagram of the axial and the flexural strength of the composite beam-columns. Again, the capacity of the columns reduces significantly as the decreasing of D/kL . It is worth noticing that the axial force in the stub column helps increasing the maximum bending resistance (which is greater than the pure bending moment resistance) at the early existence of the axial force application. In the contrary, the increasing of the axial force in the slender column will not help increase but instead reduce the moment resistance due to the additional bending moment created by the P-delta effect. The pure bending moment resistance remains the same despite the column length since the composite columns now depict the behavior of the composite beams. As also illustrated in Figure 6.9, the D/kL mainly influences the flexural capacity of the beam-columns at the early increasing of e/D but this effect fades away as e/D becomes large. It is also observed that there is a drop of the bending capacity for the columns with large D/kL before the moment becomes constant. Furthermore, the axial capacity of the stub columns reduces at faster rate than that of the slender columns when the eccentricity lies within

the half of the cross-section as shown in Figure 6.8. And after increasing e/D more than 0.5, the axial load-carrying capacity drops almost at the same rate.

Table 6.5: Results of the verified numerical approach for parametric study.

| Group | Parametric Column (Square – H) | e/D | D/kL | Ultimate Strength (kN) |
|-------|----------------------------------|-------|-------|------------------------|
| G1 | PC1 | 0.125 | 0.23 | 1146 |
| | PC2 | 0.25 | 0.23 | 801 |
| | PC3 | 0.375 | 0.23 | 608 |
| G2 | PC4 | 0.125 | 0.092 | 1034 |
| | PC5 | 0.25 | 0.092 | 698 |
| | PC6 | 0.375 | 0.092 | 534 |
| G3 | PC7 | 0.125 | 0.058 | 799 |
| | PC8 | 0.25 | 0.058 | 543 |
| | PC9 | 0.375 | 0.058 | 424 |
| G4 | PC10 | 0.3 | 0.23 | 702 |
| | PC11 | 0.3 | 0.23 | 1009 |
| | PC12 | 0.3 | 0.23 | 1259 |
| G5 | PC13 | 0.3 | 0.092 | 612 |
| | PC14 | 0.3 | 0.092 | 859 |
| | PC15 | 0.3 | 0.092 | 1084 |
| G6 | PC16 | 0.3 | 0.058 | 481 |
| | PC17 | 0.3 | 0.058 | 672 |
| | PC18 | 0.3 | 0.058 | 828 |
| G7 | PC19 | 0.3 | 0.23 | 663 |
| | PC20 | 0.3 | 0.23 | 715 |
| | PC21 | 0.3 | 0.23 | 775 |
| G8 | PC22 | 0.3 | 0.092 | 594 |
| | PC23 | 0.3 | 0.092 | 621 |
| | PC24 | 0.3 | 0.092 | 640 |
| G9 | PC25 | 0.3 | 0.058 | 486 |
| | PC26 | 0.3 | 0.058 | 486 |
| | PC27 | 0.3 | 0.058 | 486 |

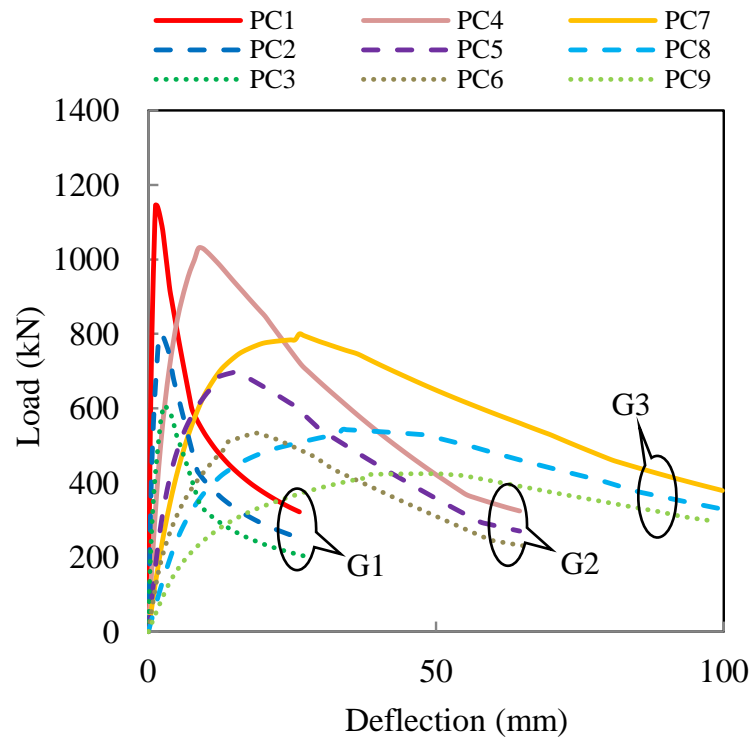


Figure 6.6: Effects of eccentricity and column effective length on nonlinear load and deflection responses.

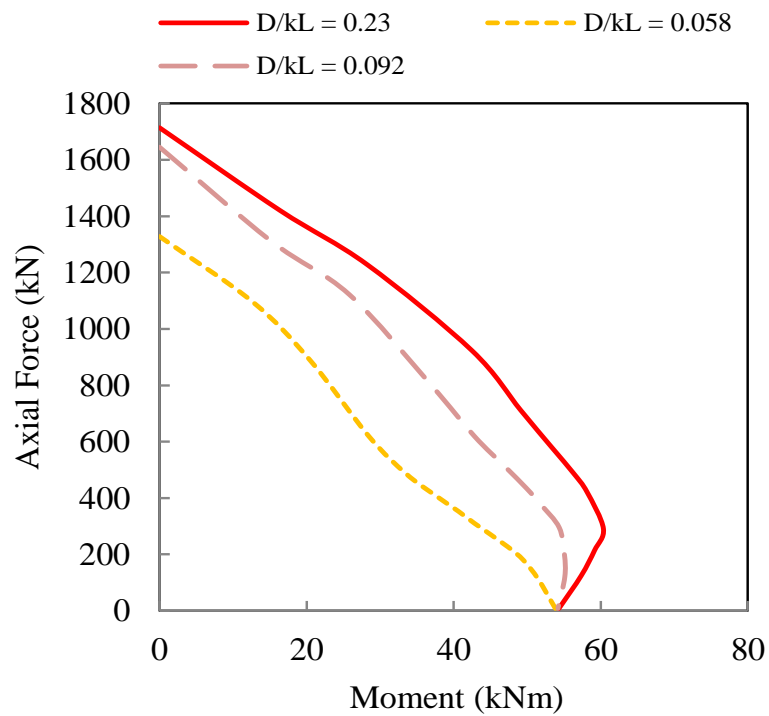


Figure 6.7: Effects of column effective length on force and moment interaction diagrams.

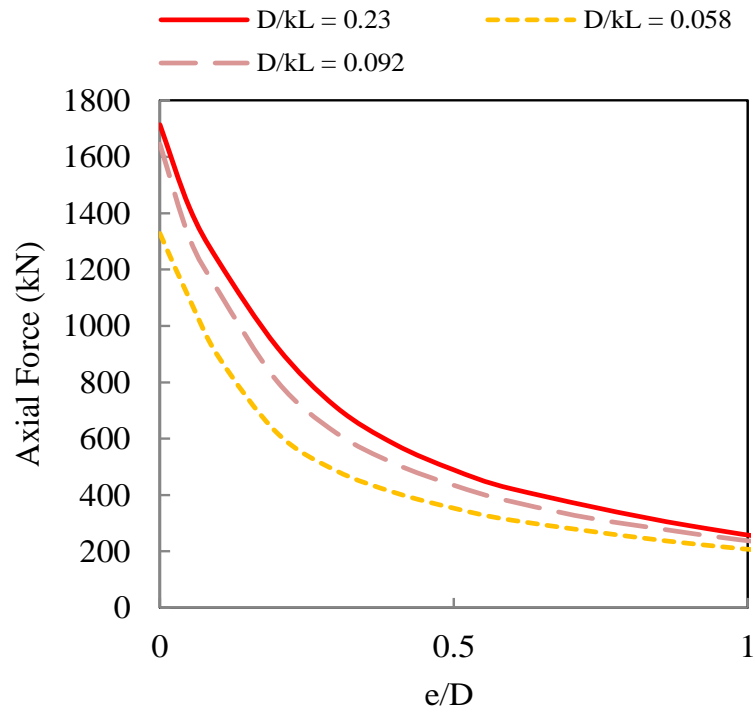


Figure 6.8: Effects of eccentricity and column effective length on axial force.

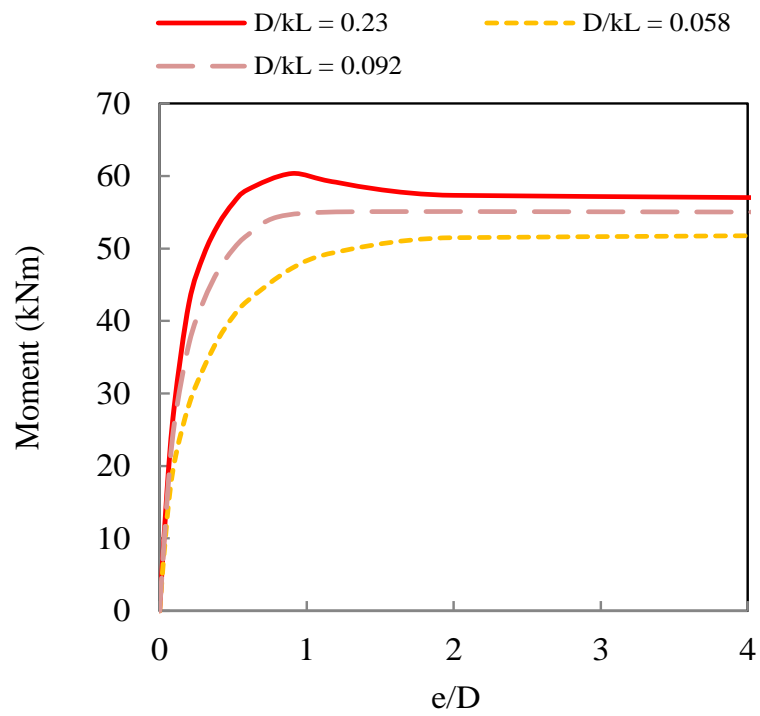


Figure 6.9: Effects of eccentricity and column effective length on bending moment.

6.4.3 Effects of concrete strength with different effective length ratios

The effects of concrete strength and D/kL ratio on the overall behavior of the concrete encased steel composite beam-columns are shown in Figure 6.10. It is observed that increasing the concrete strength enhances the ultimate axial capacity of the composite beam-columns, but with lower ductility. The less the effective length ratio becomes, the less influence the concrete strength has on the axial capacity of the columns. Furthermore, the axial force-moment interaction diagram in Figure 6.11 shows that increasing the concrete strength will increase the axial capacity significantly only before reaching the maximum bending moment resistance, and becomes less significant as the beam-columns behave as pure bending. The decreasing rate of the axial capacity of the composite beam-columns due to eccentricity ratios for different concrete strength can be observed from Figure 6.12. Obviously, the concrete strength reduces the axial capacity of the beam-columns significantly only when the e/D lies probably within 0.5 of the section depth. When e/D becomes larger, increasing the concrete strength is not a good decision for engineers. However, it still can enhance the moment capacity of the composite beam-columns (as shown in Figure 6.13) although its influence is less significant when e/D is larger than 0.5.

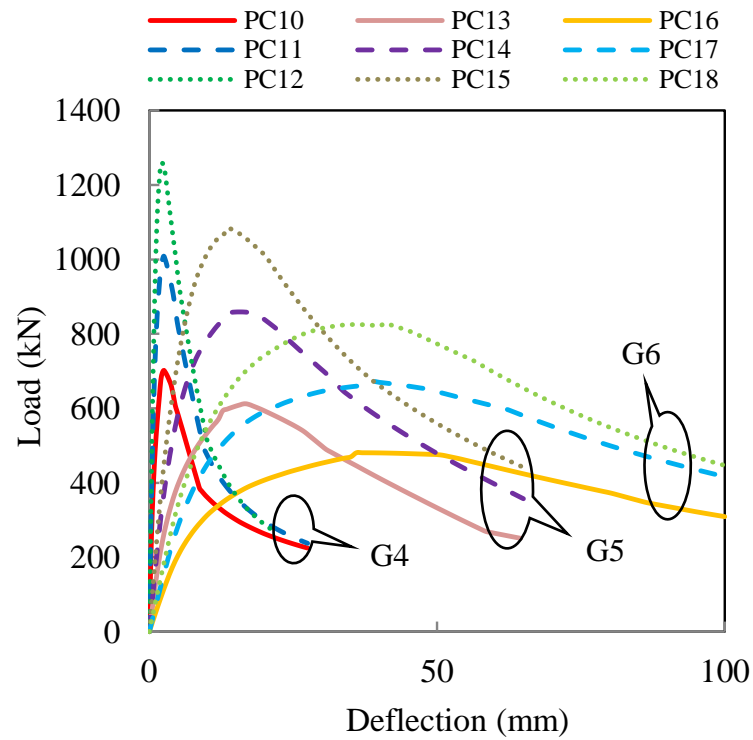


Figure 6.10: Effects of concrete strength and column effective length on nonlinear load and deflection responses.

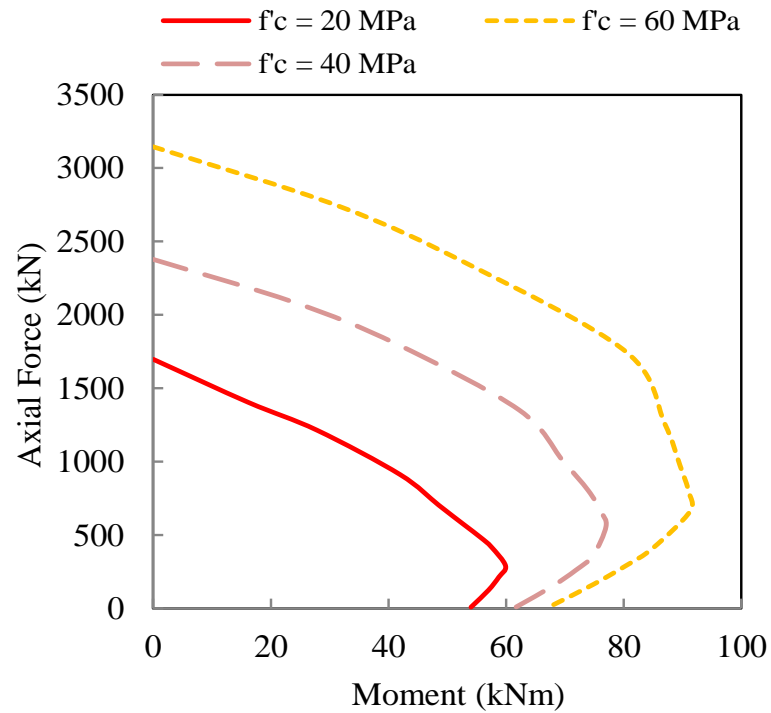


Figure 6.11: Effects of concrete strength on force and moment interaction diagrams.

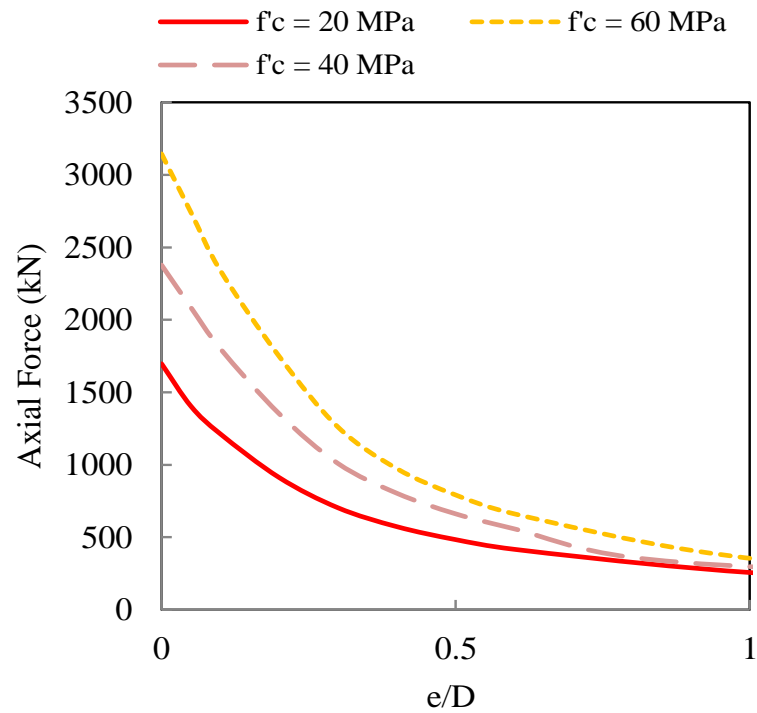


Figure 6.12: Effects of concrete strength on axial force and eccentricity curves.

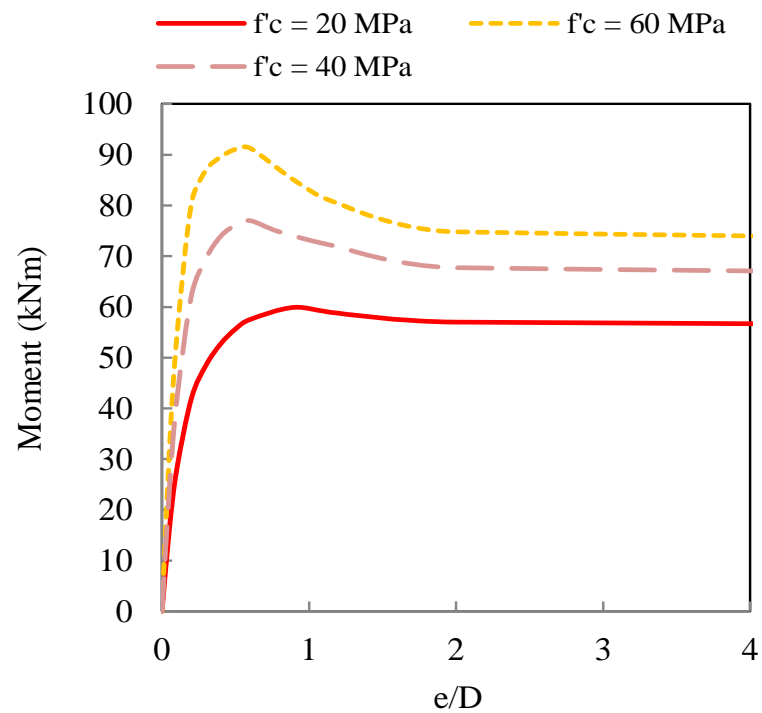


Figure 6.13: Effects of concrete strength on moment and eccentricity curves.

6.4.4 Effects of steel strength with different effective length ratios

Figure 6.14 illustrates the influences of the structural steel yield strength and the D/kL ratio on the load-deflection responses of the concrete encased steel composite beam-columns. It is found that increasing the steel strength increases mainly the column ultimate strength of the stocky columns, but does not the ductility. Moreover, it increases the axial load capacity of the stub columns more significantly than that of the slender columns. However, it is observed that the more slender the columns are, the less effective the structural steel strength becomes on the axial capacity of the columns.

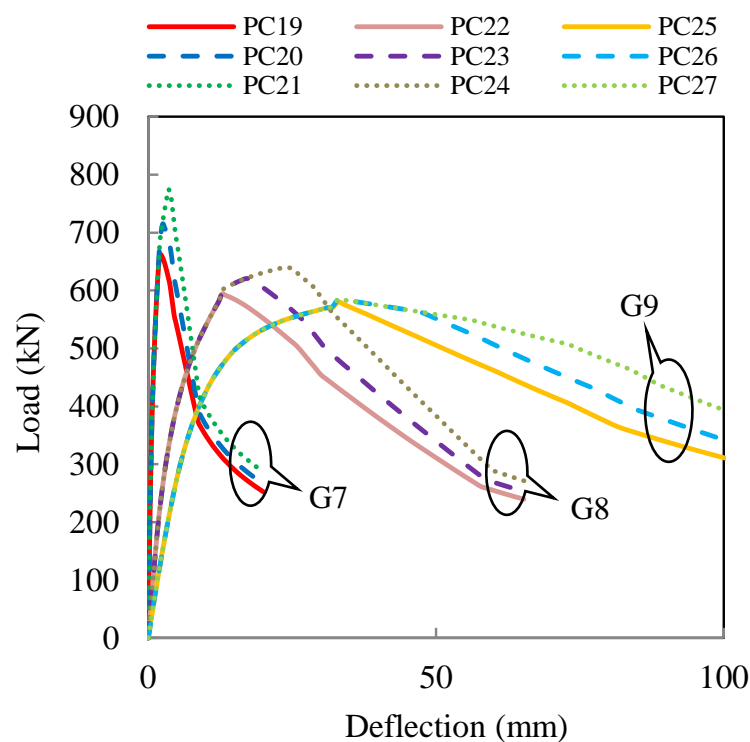


Figure 6.14: Effects of steel strength and column effective length on nonlinear load and deflection responses.

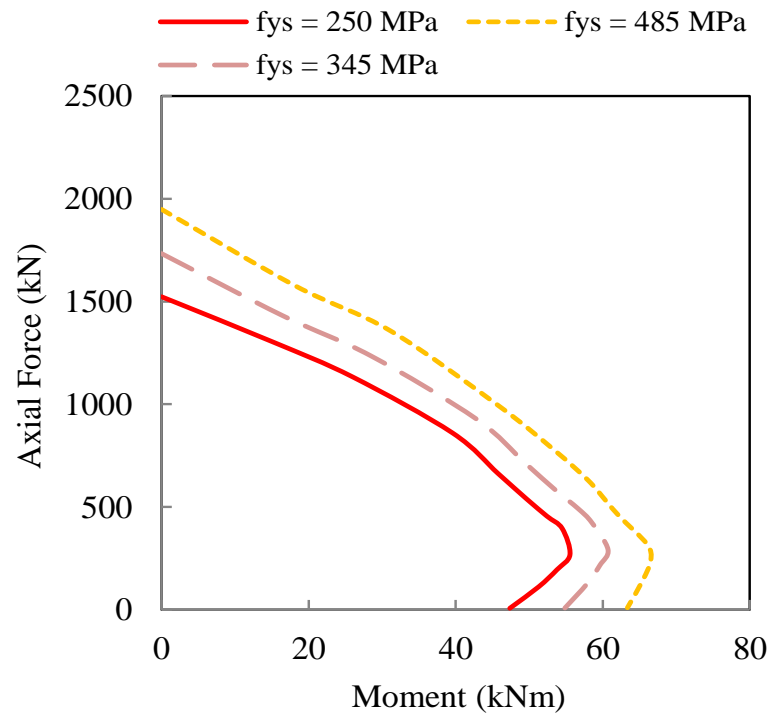


Figure 6.15: Effects of steel strength on force and moment interaction diagrams.

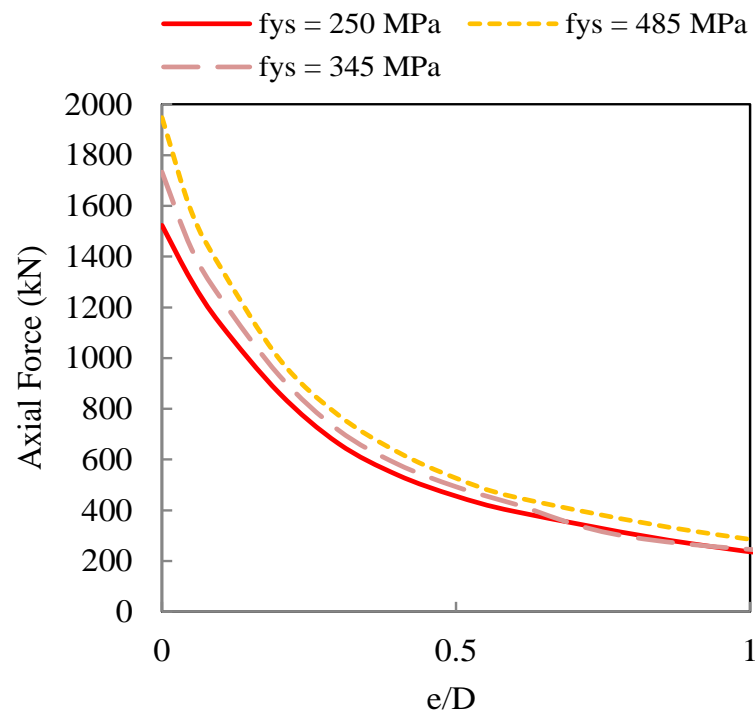


Figure 6.16: Effects of steel strength on axial force and eccentricity curves.

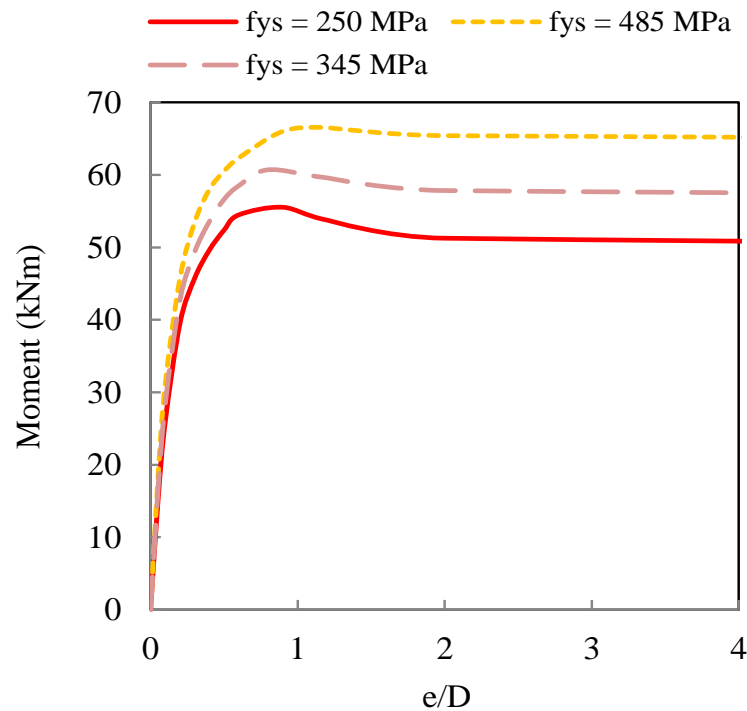


Figure 6.17: Effects of steel strength on moment and eccentricity curves.

The interaction diagram for different steel strengths in Figure 6.15 shows that higher steel strength will increase the bending capacity of the composite beam-columns and even more after the maximum moment resistance since the structural steel is less sensitive to buckling under bending. Figure 6.16 shows the decreasing rate of the axial capacity of the composite columns with the increasing of e/D ratios for different steel strength. It is observed that the steel strength is effective for the composite beam-columns under small eccentricity. The larger e/D becomes, the less influence the steel strength has on the axial column capacity. Despite, it still enhances the bending capacity of the composite beam-columns as also illustrated in Figure 6.17.

6.5 Concluding Remarks

The ultimate strength capacity and full structural response of the stub and slender concrete encased steel composite columns subjected to eccentric compressive load have been investigated using the sophisticated nonlinear inelastic numerical approach. The numerical scheme has carefully taken into account of the nonlinearity of material behaviors such as the strain hardening and softening, local buckling of the structural steel, the confinement effects from the structural steel and reinforcement bars, and the buckling of the longitudinal reinforcement bars. The initial geometric imperfection and P-delta effect are cooperated directly into the numerical analysis. The numerical approach for pin-ended composite beam-columns is developed based on the fiber element formulation using lateral displacement control. Good agreements between the numerical results with experiments has proved that the proposed numerical scheme is very efficient for predicting both the ultimate strength and the axial load and deflection response of the stub and slender concrete encased steel composite beam-columns.

The validated numerical approach is used in the parametric studies to extend the investigation of the concrete encased steel composite beam-columns behaviors due to the changes in the column effective length ratios, eccentricity ratios, concrete strength, and structural steel yield stress. It is concluded that slender beam-columns (i.e. having small depth-to-effective length ratio) are more ductile than stocky ones (i.e. having large depth-to-effective length ratio). The effective length mainly affects the flexural capacity of the beam-columns at the early increasing of e/D but its effect become less when e/D is large. Similarly, the columns subjected to large eccentricity ratios are more ductile than that those with small eccentricity ratios. Increasing the

concrete strength enhances the ultimate axial strength, but with lower ductility. And when e/D becomes larger, increasing the concrete strength does not significantly increase the axial capacity of the beam-columns. Furthermore, increasing the steel strength improves mainly the stocky column ultimate strength but not the ductility. High steel strength enhances the axial capacity of the stub columns more significantly than the slender columns.



CHAPTER 7

PERFORMANCE ASSESSMENT OF CES STRUCTURES AND STRENGTHENING WITH STEEL BRACING SYSTEMS

7.1 Introduction

Steel–concrete composite frame systems can consist of many combinations of structural steel members and reinforced concrete members. For instance, the composite structures comprised of concrete encased steel (CES) columns and steel beams are commonly found in typical high-rise building constructions. This chapter aims to investigate such composite structures by introducing a simplified yet efficient approach with practical application. From a mesoscale simulation of CES members, a piecewise yield function as well as a softening rule have been proposed and implemented in a stepwise holonomic approach to analyze the CES composite structures. The proposed analysis approach has been validated by comparing with the experimental tests. The complete structural responses of such composite structures along with the plastic formations and developments can be illustrated event-by-event for further investigation. After being able to assess and understand the performance of CES structures, the structural retrofitting by means of conventional steel bracing system can be carried out. By comparing the responses of various steel bracing systems, recommendations can be made to select a suitable type of bracing configurations for performance and economical view point.

7.2 Mathematical Programming Tools

Mathematical programming (MP) has been used extensively almost in every field, not to mention only Engineering. In broad terms, MP can be defined as a mathematical model to assist the decision-making with the best possible allocation of scarce resources. In other words, MP is a set of mathematical equations. When the mathematical model composes of linear functions, it is called a linear-programming (LP) model. Researchers in the past recognized the power of MP as a theoretical and computational tool for finding extensive structural plasticity problems, such as limit analysis, elastoplastic deformation analysis, unilateral contact, and dynamic plasticity. The algebraic modeling languages are generally accepted as the best way to solve mathematical programming problems. Mathematical programming approaches and extended limit analysis incorporated with General Algebraic Modeling System (GAMS) has been extensively used with steel frame structures problems concerning with strain softening, nonlinear performance, safety assessment, and optimization (Tangaramvong and Tin-Loi 2007, 2008, 2009, 2011, Tangaramvong et al. 2014).

Particularly in the current work of this thesis, GAMS is used to solve MP problems related to the simulation of composite frames. Various MP solvers are available within this platform. The input generations are performed within MATLAB, which then GAMS is called to solve MP problems, and the solutions are then returned within MATLAB. The connection tasks between MATLAB and GAMS are done through an interfacing software known as MATLAB/GAMS link, which was developed by Ferris (1998).

GAMS (Brook et al. 1988) was initially developed by the Development Research Committee, under the support of The World Bank in Washington, DC, to produce the high-level programming languages for large and complex MP problems. Models in GAMS can be made changes easily and safely. It allows clear algebraic relationships for coding without the complexity of the algorithm programming language. And it permits model descriptions that are independent of solution algorithms.

Multiple model types are available in GAMS such as: Linear Programming (LP), Mixed Integer Programming (MIP), Nonlinear Programming (NLP), Mixed Complementarity Programming (MCP), Mixed Integer Nonlinear Programming (MINLP), NLP with Complementarity Constraints (MPEC), General Equilibrium Models (MPSGE), and Stochastic Optimization. The supported built-in solvers are briefly described below:

- BDMLP: LP solver that comes with any GAMS system
- CONOPT: Large scale NLP solver from ARKI Consulting and Development
- CPLEX: High-performance LP/MIP solver from Ilog
- DECIS: Large scale stochastic programming solver from Standard University
- DICOPT: Framework for solving MINLP models.
- MILES: MCP solver from University of Colorado
- MINOS: NLP solver form Stanford University
- MPSGE: Modeling environment for CGE models from University of Colorado
- OSL: High performance LP/MIP solver from IBM
- OSLSE: OSL Stochastic Extension for solving stochastic models
- PATH: Large scale MCP solver from University of Wisconsin at Madison

- SBB: Branch-and-Bound algorithm from ARKI Consulting and Development for solving MINLP models
- SNOPT: Large scale SQP based NLP solver from Stanford University
- XA: Large scale LP/MIP system from Sunset Software
- XPRESS: High performance LP/MIP solver from Dash

7.3 Plasticity Model

7.3.1 Review of Yield Criterion

In the theory of plasticity, there are three main components, i.e. a yield criterion or yield function, a flow rule, and a hardening/softening rule. A yield criterion defines the initial state of material inelastic response. A flow rule associates the relations between the plastic strain increments and the stress increments after initiation of the inelastic response. A hardening/softening rule determines the changes of the yield surface due to the plastic deformation. Generally, the yield surface, i.e. a geometrical representation of a yield function, is a continuous nonlinear surface which poses big computational challenges to large size numerical problems. Simplified piecewise linearization of yield surface was successfully adopted by Maier and his team (Maier 1970, 1971, De Donato and Maier 1972, Maier et al. 1972, Maier 1976). An approximation of a nonlinear yield locus, for combined generalized stresses s_1^i and s_2^i in a hinge a of a frame element i , using piecewise linear yield hyperplanes is illustrated in Figure 7.1.

The yield function is usually expressed in mathematical expression as:

$$\omega^a(S^a, P^a, H^a) \leq 0 \quad (7.1)$$

where ω^a denotes the yield function, S^a the multiple stresses, P^a the plastic strains, and H^a the hardening/softening parameters.

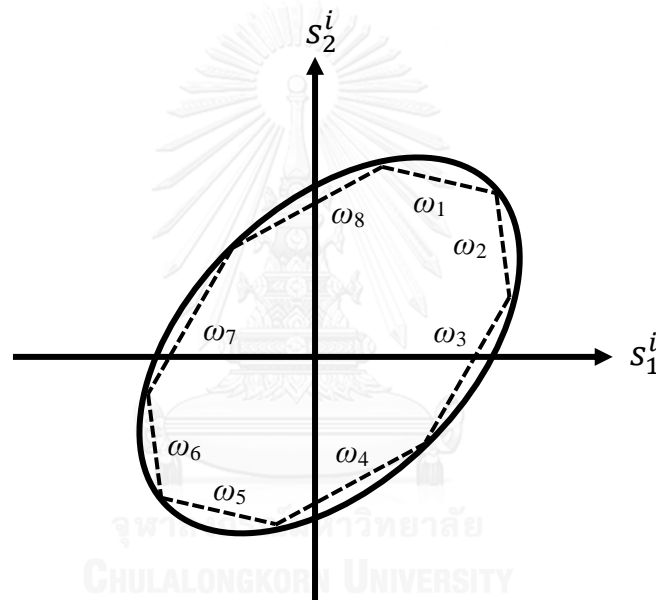


Figure 7.1: Simplified yield surface by piecewise linear yield hyperplanes.

Some typical piecewise linear hyperplanes are illustrated in Figure 7.2, the axes represent the dimensionless bending moment s_2^i/s_{2u} and axial force s_1^i/s_{1u} where s_{2u} and s_{1u} are the corresponding yield capacities, respectively. When yielding is governed by only a single stress, the yield surface consists of two straight parallel lines running perpendicular to the governing stress (see Figure 7.2a-b). For yielding governed by combined stresses, the yield surface is formed by the interaction of those stresses (i.e. Figure 7.2c-f). The shape of the yield surface depends on the cross-

section and material of the element. A good piecewise yield hyperplane for an I-shaped steel section is best represented by the hexagonal shape (Massonnet and Save 1965, Cohn and Rafay 1974) and was successfully used in corporation with GAMS (Tangaramvong and Tin-Loi 2007, 2008, 2009, 2011). Grierson and Abdel-Baset (1977) adopted the octagonal stress interaction yield hyperplanes for a solid rectangular cross-section to frame members.

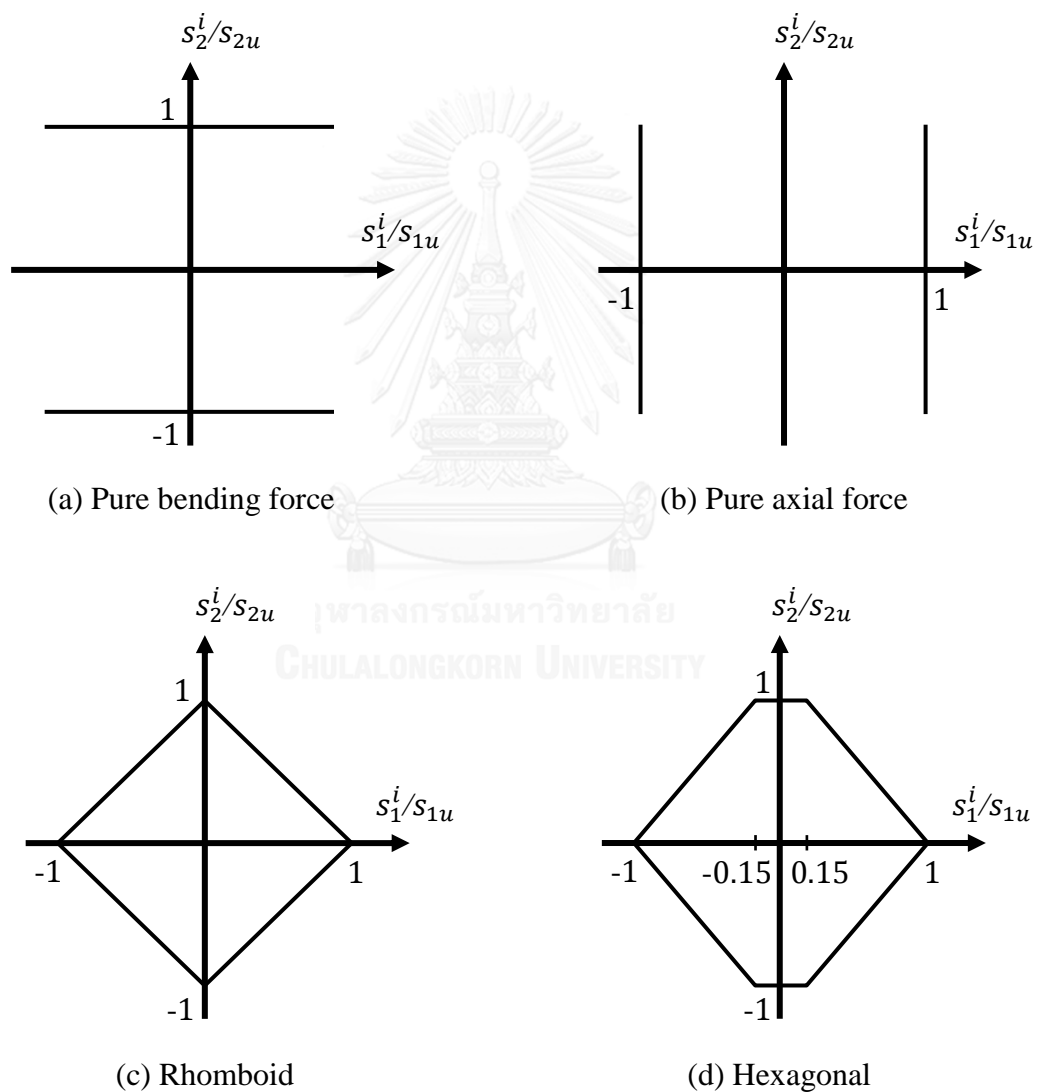


Figure 7.2: Types of piecewise linear yield hyperplanes.

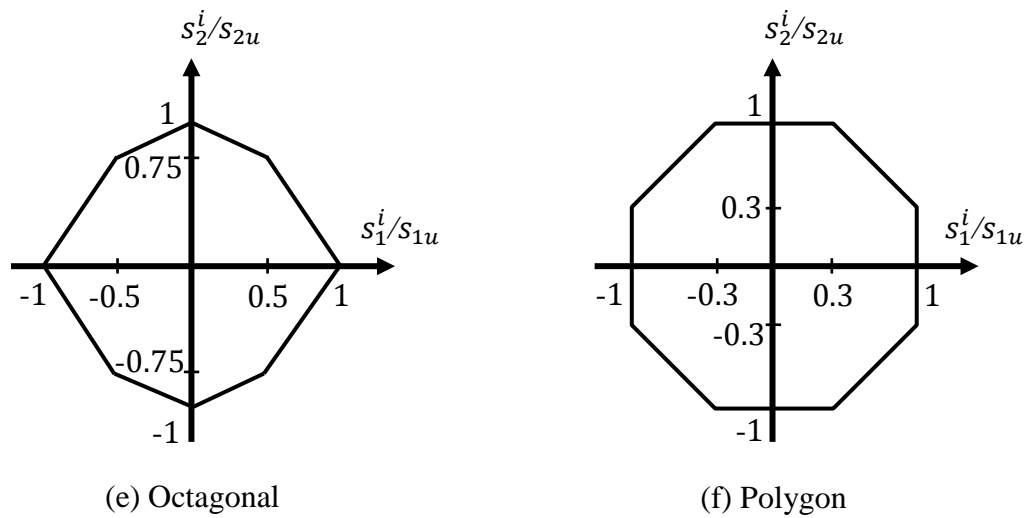
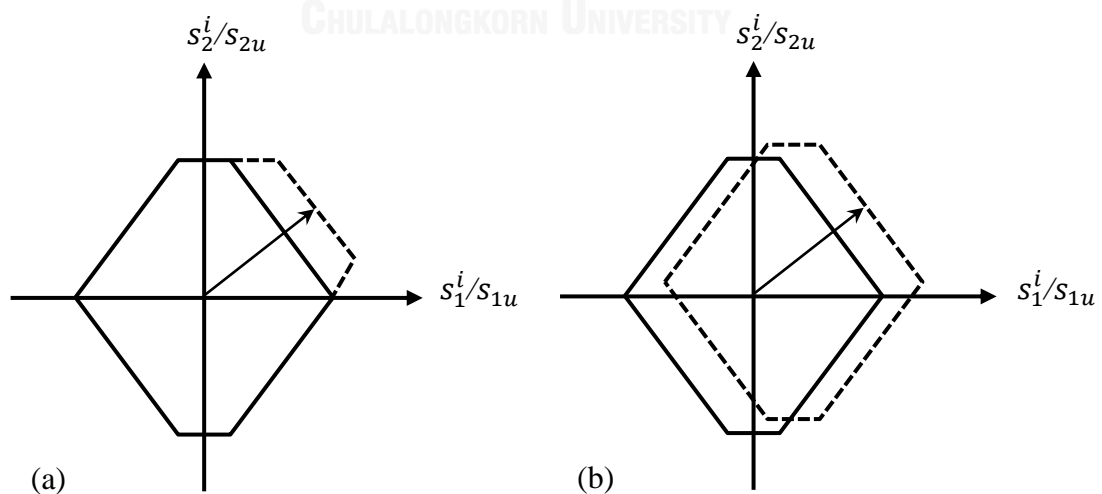


Figure 7.2: Types of piecewise linear yield hyperplanes – *Cont.*

Some examples of conventional hardening rules, e.g. Koiter's noninteracting hardening, Prager's kinematic hardening, and isotropic hardening, were provided by Maier (1970) as illustrated in Figure 7.3. It is worth mentioning that the softening rule can be similarly defined by using negative hardening parameters.



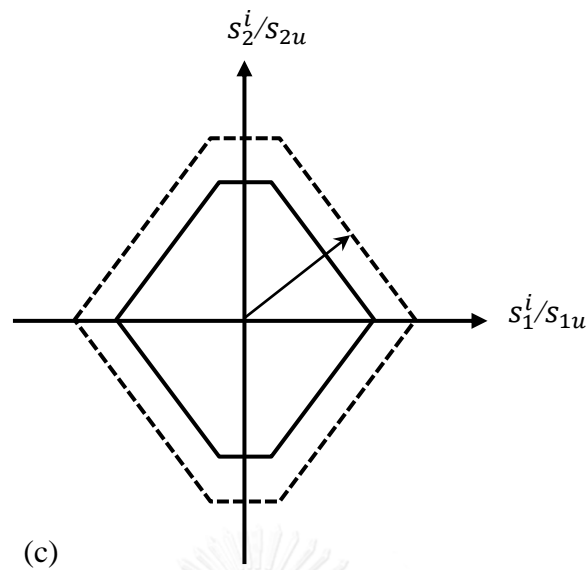


Figure 7.3: Hardening rules (a) Koiter's noninteracting hardening, (b) Prager's kinematic hardening, (c) Isotropic hardening.

A well-known mathematical representation of the yield criterion for all hyperplanes was given by Maier (1970) as follow:

$$\omega^a = N^{aT} S^a - H^a \lambda^a - R^a \leq 0 \quad (7.2)$$

where N^a is the normality matrix of each yield hyperplanes, S^a the multiple stresses, H^a the hardening/softening parameters, λ^a the non-negative plastic multiplier rate vector, and R^a the vector of residual constants.

An extensive description and summary of piecewise linear yield functions for single stress and combined stress models in terms of perfect plasticity, softening, and hardening can be found in the work of Tangaramvong (2007). For an I-shaped steel section under combined axial force and bending moment, the hexagonal piecewise linear yield hyperplanes is commonly recommended (Massonnet and Save 1965).

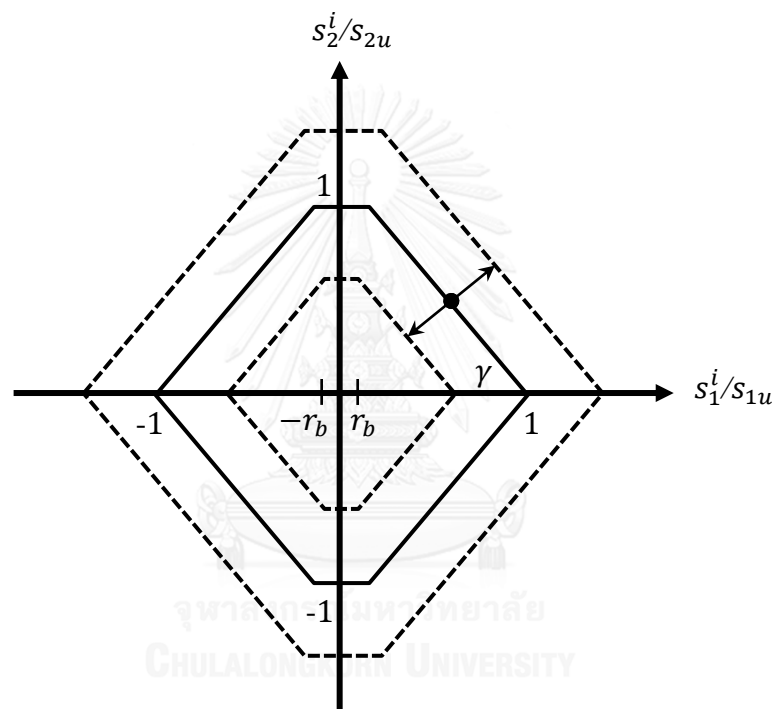


Figure 7.4: Hexagonal piecewise linear yield surface.

The yield surface in Figure 7.4 defines the properties of a hinge a of the element i with the isotropic hardening/softening rule, where γ is an inclined angle of the yield hyperplanes and r_b is a reduction factor for pure bending capacity (i.e. commonly taken as 0.15). The development of isotropic hardening or softening hyperplanes is described by the material constitutive laws (Cocchetti et al. 2001). The isotropic hardening and softening, as indicated by the outer and inner dashed line in

Figure 7.4, is characterized by expanding and shrinking the yield surface uniformly without changing the locus shape.

For the case of hexagonal piecewise linear yield functions with isotropic softening law, the interaction between dimensionless bending ratio s_2^i/s_{2u} and axial force s_1^i/s_{1u} is represented by Figure 7.5. The mathematical representations of the yield surface are as follows:

$$\omega^{aT} = [\omega_1 \quad \omega_2 \quad \omega_3 \quad \omega_4 \quad \omega_5 \quad \omega_6 \quad \omega_7] \quad (7.3)$$

$$S^{aT} = [s_1^i \quad s_2^i]$$

$$\lambda^{aT} = [\lambda_1 \quad \lambda_2 \quad \lambda_3 \quad \lambda_4 \quad \lambda_5 \quad \lambda_6 \quad \lambda_7]$$

$$N^a = \begin{bmatrix} 0 & n \tan \gamma & n \tan \gamma & 0 & -n \tan \gamma & -n \tan \gamma & 0 \\ 1 & 1 & -1 & -1 & -1 & 1 & 0 \end{bmatrix}$$

$$H^a = h \begin{bmatrix} a_1 & a_2 & a_3 & a_4 & a_5 & a_6 & -1 \\ \tau a_1 & \tau a_2 & \tau a_3 & \tau a_4 & \tau a_5 & \tau a_6 & -\tau \\ \tau a_1 & \tau a_2 & \tau a_3 & \tau a_4 & \tau a_5 & \tau a_6 & -\tau \\ a_1 & a_2 & a_3 & a_4 & a_5 & a_6 & -1 \\ \tau a_1 & \tau a_2 & \tau a_3 & \tau a_4 & \tau a_5 & \tau a_6 & -\tau \\ \tau a_1 & \tau a_2 & \tau a_3 & \tau a_4 & \tau a_5 & \tau a_6 & -\tau \\ \frac{a_1}{s_{2u}} & \frac{a_2}{s_{2u}} & \frac{a_3}{s_{2u}} & \frac{a_4}{s_{2u}} & \frac{a_5}{s_{2u}} & \frac{a_6}{s_{2u}} & \frac{-1}{s_{2u}} \end{bmatrix}$$

$$R^{aT} = [s_{2u} \quad \tau s_{2u} \quad \tau s_{2u} \quad s_{2u} \quad \tau s_{2u} \quad \tau s_{2u} \quad 1 - r_r]$$

where

$$n = s_{2u}/s_{1u}$$

$$h = -s_{2u}(1 - r_r)/p_c$$

$$\tau = 1 + r_b \tan \gamma$$

$$a_j = p_c/|p_{cj}|, j = 1 \dots 6$$

where ω^a denotes the yield function, S^a the multiple stresses, λ^a the non-negative plastic multiplier rate vector, N^a the normality matrix of each yield hyperplanes, H^a the hardening/softening parameters, and R^a the vector of residual constants.

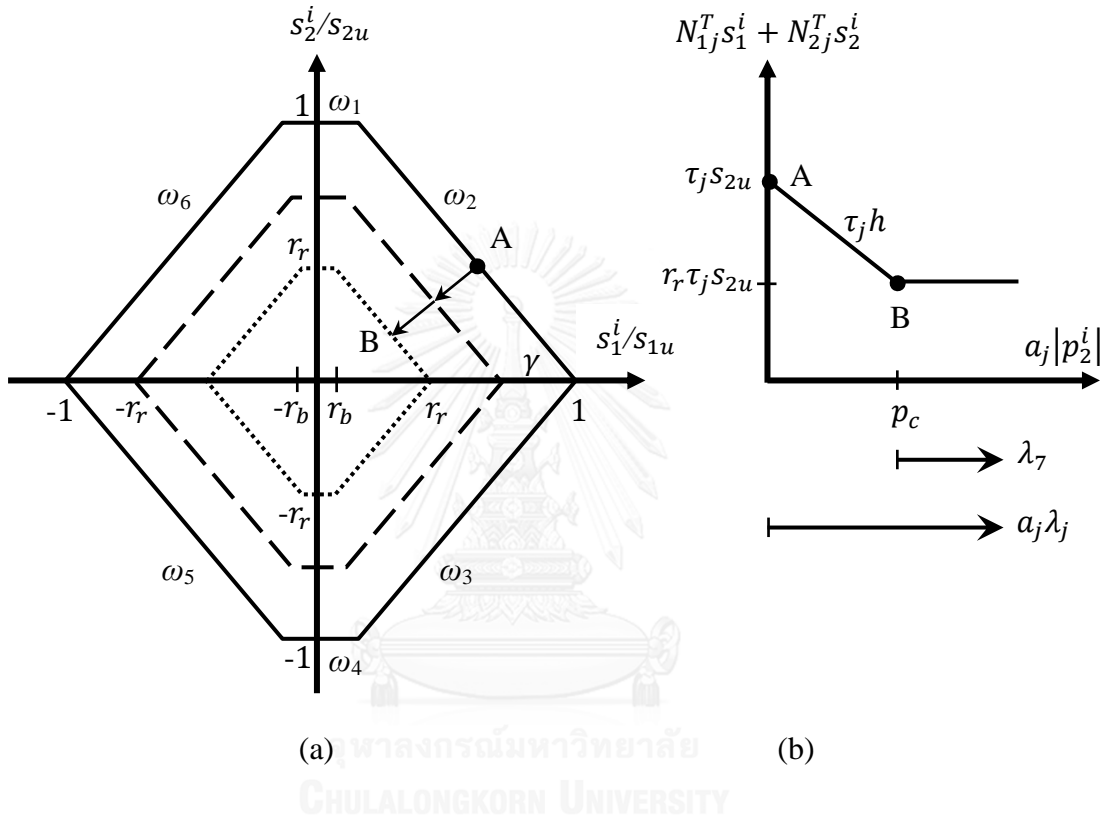


Figure 7.5: Piecewise linear (a) hexagonal yield surface (b) softening law for plane j .

More explicitly, the yield functions ω_1 to ω_6 identify the softening transition of their hyperplanes 1 to 6, respectively, which correspond to the middle dashed line in Figure 7.5a. The softening behavior of typical piecewise yield hyperplanes is plotted in terms of the combined stresses $(N_{1j}^T s_1^i + N_{2j}^T s_2^i)$ and plastic strain $|p_2^i|$, where N_{1j}^T and N_{2j}^T are normal projections on s_1^i and s_2^i axes, respectively. It is worth noting that an additional yield function ω_7 is to capture the movement of a yielding point on the residual branch which corresponds to the smallest dashed line of yield

surface in Figure 7.5a. As the stress point starts moving along the inclined softening branches, the corresponding yield hyperplane will shrink to accommodate the softening behavior. At the same time, the rest of hyperplanes also shrink while keeping the same shape due to the assumption of isotropic softening law.

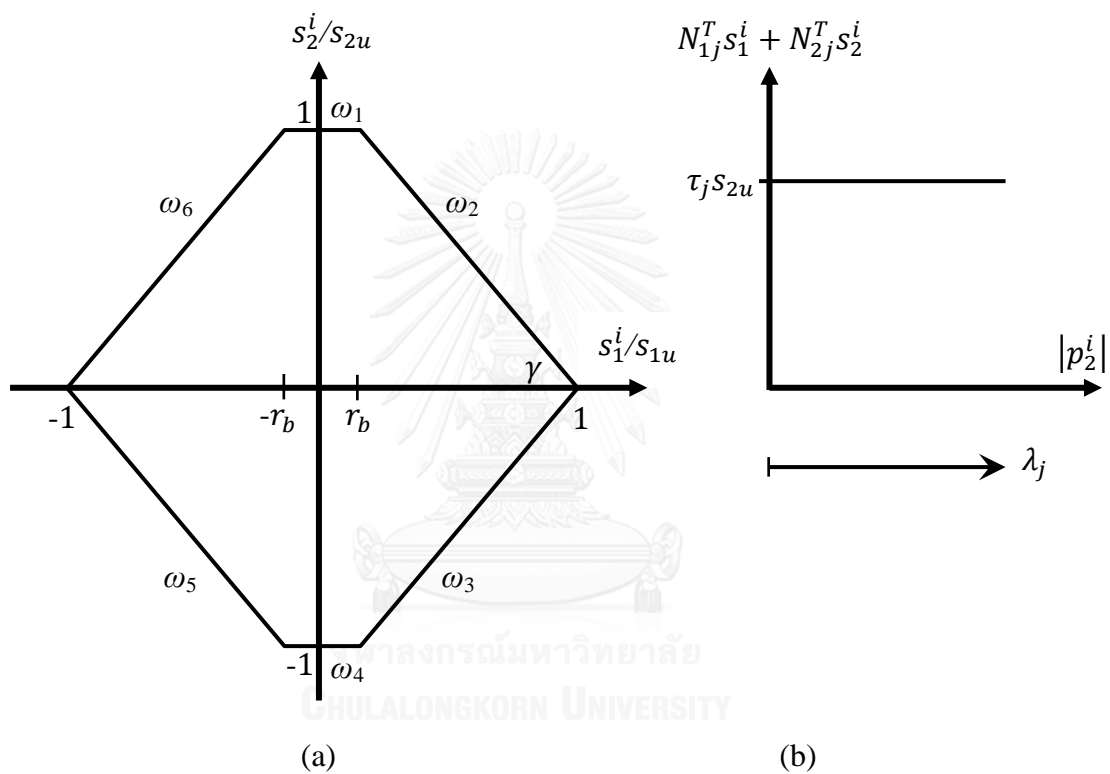


Figure 7.6: Piecewise linear (a) hexagonal yield surface (b) perfectly plastic law for plane j .

Similarly, the mathematical representations for the hexagonal piecewise linear yield functions with perfectly plastic law as shown in Figure 7.6 can be simply expressed by removing the softening parameters as well as an additional yield function for residual hyperplane. The mathematical representations of the yield surface become:

$$\omega^{aT} = [\omega_1 \quad \omega_2 \quad \omega_3 \quad \omega_4 \quad \omega_5 \quad \omega_6] \quad (7.4)$$

$$S^{aT} = [s_1^i \quad s_2^i]$$

$$\lambda^{aT} = [\lambda_1 \quad \lambda_2 \quad \lambda_3 \quad \lambda_4 \quad \lambda_5 \quad \lambda_6]$$

$$N^a = \begin{bmatrix} 0 & n \tan \gamma & n \tan \gamma & 0 & -n \tan \gamma & -n \tan \gamma \\ 1 & 1 & -1 & -1 & -1 & 1 \end{bmatrix}$$

$$H^a = 0$$

$$R^{aT} = [s_{2u} \quad \tau s_{2u} \quad \tau s_{2u} \quad s_{2u} \quad \tau s_{2u} \quad \tau s_{2u}]$$

where

$$n = s_{2u}/s_{1u}$$

$$\tau = 1 + r_b \tan \gamma$$

7.3.2 Yield Criterion and Softening Rule for CES sections

Despite many previous researches, there is no unified yield criterion or softening laws that has been established to accurately predict the yielding of all materials. A novel piecewise linear yield model of softening material properties underpinning concrete encased steel sections has been proposed to fully capture the nonlinear inelastic response with sophisticated post-peak softening behavior. The proposed yield surface for CES sections under combined stresses is singly symmetric about s_1^i/s_{1u} axis as illustrated in Figure 7.7. It is comprised of six piecewise linear

hyperplanes (i.e. ω_1 to ω_6). The softening rule is defined as that the hyperplanes ω_1 , ω_2 , ω_5 , and ω_6 shrink uniformly while retaining the original shape of the yield surface. The associated softening behavior is described by three plastic softening portions under compression (i.e. two softening and one residual portions), and a perfectly plastic under tension (where s_{1t} is the maximum tensile yielding capacity) is assumed as indicated in Figure 7.8. As the stress point moves along the first softening portion, the interaction between the bending moment s_2^i/s_{2u} and axial force s_1^i/s_{1u} will reduce to represent the softened yield surface following the proposed softening rule.

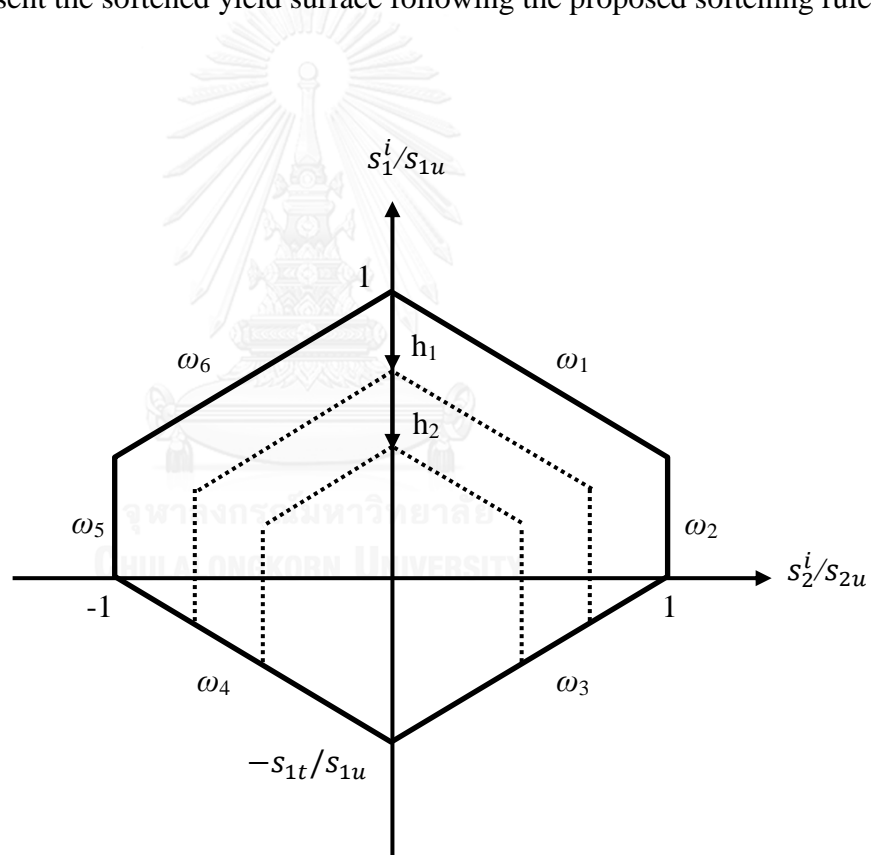


Figure 7.7: Piecewise linear yield surface for CES section.

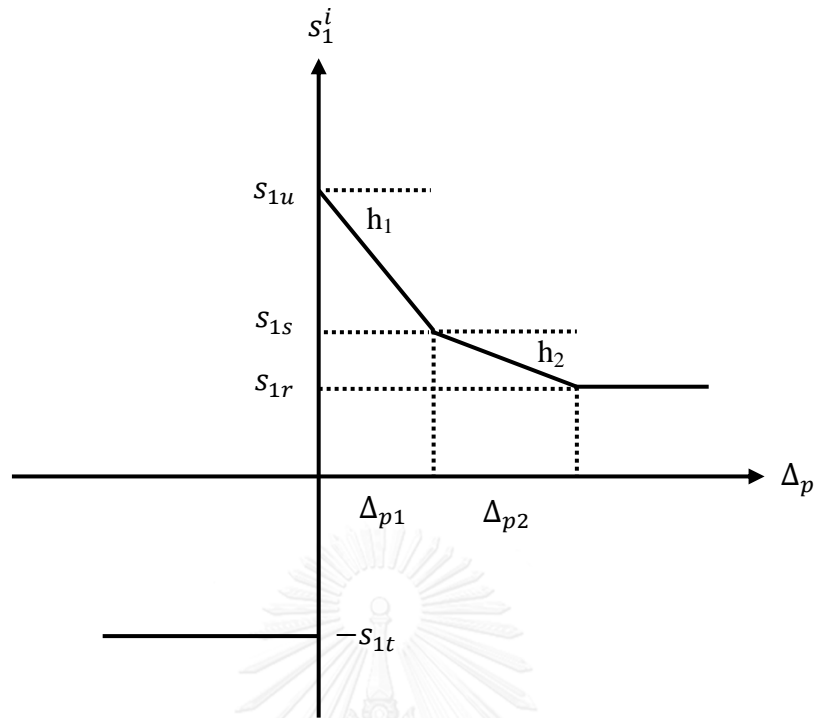


Figure 7.8: Piecewise linear softening rule for CES section.

In order to derive the mathematical representation of the proposed yield function, consider the normality directions N_1 to N_6 on the each hyperplane ω_1 to ω_6 , respectively (see Figure 7.9). The stress point is projected to all the normality directions, where the yield function for the elastic limit condition under combined stresses can be established. The angle γ is denoted as an inclined angle of the top yield hyperplanes, and β is an angle of the bottom yield hyperplanes.

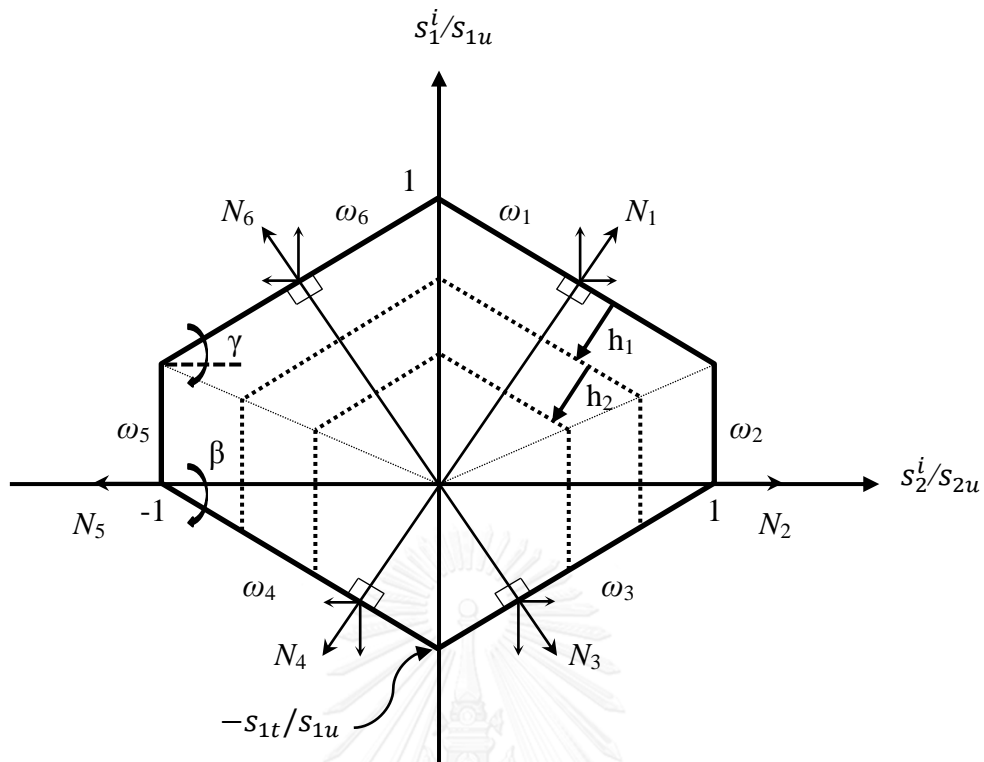


Figure 7.9: Key parameters of piecewise linear yield surface for CES section.

In case of elastic under combined stresses:

$$\omega_1 = \cos \gamma \cdot \left(\frac{s_1^i}{s_{1u}} \right) + \sin \gamma \cdot \left(\frac{s_2^i}{s_{2u}} \right) - \cos \gamma \leq 0$$

$$\omega_2 = \left(\frac{s_2^i}{s_{2u}} \right) - 1 \leq 0$$

$$\omega_3 = -\cos \beta \cdot \left(\frac{s_1^i}{s_{1u}} \right) + \sin \beta \cdot \left(\frac{s_2^i}{s_{2u}} \right) - \cos \beta \leq 0$$

$$\omega_4 = -\cos \beta \cdot \left(\frac{s_1^i}{s_{1u}} \right) - \sin \beta \cdot \left(\frac{s_2^i}{s_{2u}} \right) - \cos \beta \leq 0$$

$$\omega_5 = -\left(\frac{s_2^i}{s_{2u}} \right) - 1 \leq 0$$

$$\omega_6 = \cos \gamma \cdot \left(\frac{s_1^i}{s_{1u}} \right) - \sin \gamma \cdot \left(\frac{s_2^i}{s_{2u}} \right) - \cos \gamma \leq 0$$

$$\begin{bmatrix} \omega_1 \\ \omega_2 \\ \omega_3 \\ \omega_4 \\ \omega_5 \\ \omega_6 \end{bmatrix} = \begin{bmatrix} \cos \gamma & \sin \gamma \\ 0 & 1 \\ -\cos \beta & \sin \beta \\ -\cos \beta & -\sin \beta \\ 0 & -1 \\ \cos \gamma & -\sin \gamma \end{bmatrix} \begin{bmatrix} s_1^i / s_{1u} \\ s_2^i / s_{2u} \end{bmatrix} - \begin{bmatrix} \cos \gamma \\ 1 \\ \cos \beta \\ \cos \beta \\ 1 \\ \cos \gamma \end{bmatrix} \leq 0$$

$$\omega_1 = \left(\frac{s_1^i}{s_{1u}} \right) + \tan \gamma \cdot \left(\frac{s_2^i}{s_{2u}} \right) - 1 \leq 0$$

$$\omega_1 = s_1^i + \tan \gamma \cdot \left(\frac{s_{1u}}{s_{2u}} \right) s_2^i - s_{1u} \leq 0$$

$$\omega_2 = \left(\frac{s_2^i}{s_{2u}} \right) - 1 \leq 0$$

$$\omega_2 = s_2^i - s_{2u} \leq 0$$

Similarly, for $\omega_3, \omega_4, \omega_5,$ and $\omega_6,$ we obtain:

$$\omega_3 = -s_1^i + \tan \beta \cdot \left(\frac{s_{1u}}{s_{2u}} \right) s_2^i - s_{1u} \leq 0$$

$$\omega_4 = -s_1^i - \tan \beta \cdot \left(\frac{s_{1u}}{s_{2u}} \right) s_2^i - s_{1u} \leq 0$$

$$\omega_5 = -s_2^i - s_{2u} \leq 0$$

$$\omega_6 = s_1^i - \tan \gamma \cdot \left(\frac{s_{1u}}{s_{2u}} \right) s_2^i - s_{1u} \leq 0$$

Let $\tau = \frac{s_{2u}}{s_{1u}}$

$$\text{Hence, } \begin{bmatrix} \omega_1 \\ \omega_2 \\ \omega_3 \\ \omega_4 \\ \omega_5 \\ \omega_6 \end{bmatrix} = \begin{bmatrix} 1 & \tan \gamma / \tau \\ 0 & 1 \\ -1 & \tan \beta / \tau \\ -1 & -\tan \beta / \tau \\ 0 & -1 \\ 1 & -\tan \gamma / \tau \end{bmatrix} \begin{bmatrix} s_1^i \\ s_2^i \end{bmatrix} - \begin{bmatrix} s_{1u} \\ s_{2u} \\ s_{1u} \\ s_{1u} \\ s_{2u} \\ s_{1u} \end{bmatrix} \leq 0$$

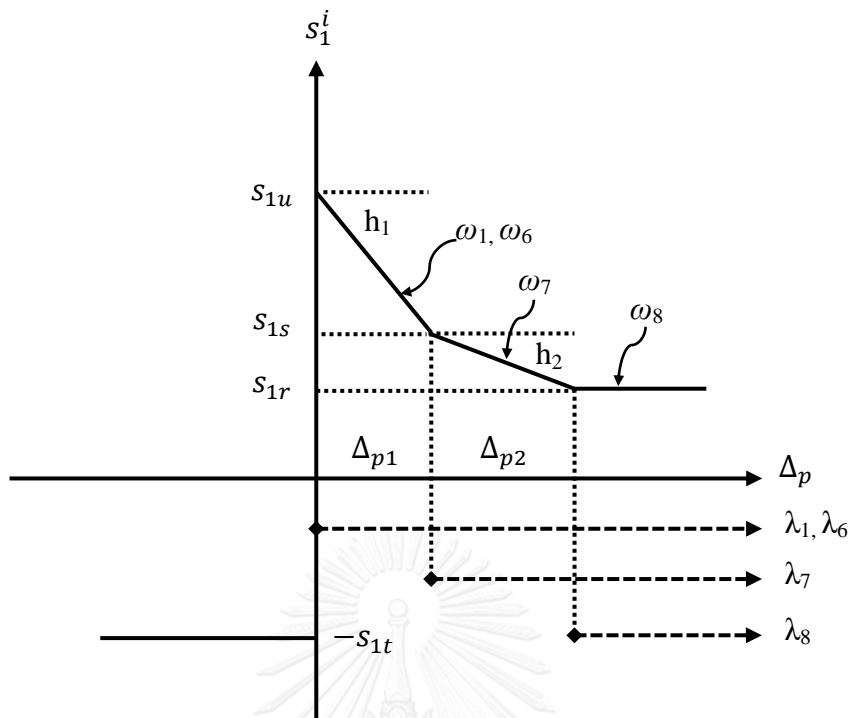


Figure 7.10: Key parameters of piecewise linear softening rule for CES section.

In case of softening under pure axial force:

From elastic limit: $\omega_1 \leq 0$ (Also, for ω_6)

$$\omega_1 = s_1^i - h_1(\lambda_1 - \lambda_7) - h_2(\lambda_7 - \lambda_8) - h_3(\lambda_8) - s_{1u} \leq 0$$

$$\omega_1 = s_1^i - (h_1)\lambda_1 - (h_2 - h_1)\lambda_7 - (h_3 - h_2)\lambda_8 - s_{1u} \leq 0$$

For the first softening branch: $\omega_1 = 0$; $\omega_7 \leq 0$

$$\omega_7 = s_1^i - h_2(\lambda_7 - \lambda_8) - h_3(\lambda_8) - s_{1s} \geq 0$$

$$\omega_7 = -s_1^i + h_2(\lambda_7 - \lambda_8) + h_3(\lambda_8) + s_{1s} \leq 0$$

$$\omega_7 + \omega_1 = [-s_1^i + h_2(\lambda_7 - \lambda_8) + h_3(\lambda_8) + s_{1s}]$$

$$+ [s_1^i - (h_1)\lambda_1 - (h_2 - h_1)\lambda_7 - (h_3 - h_2)\lambda_8 - s_{1u}] \leq 0$$

$$\omega_7 + \omega_1 = -(h_1)\lambda_1 - (-h_1)\lambda_7 - (s_{1u} - s_{1s}) \leq 0$$

$$\omega_7 = -(h_1)\lambda_1 - (-h_1)\lambda_7 - (s_{1u} - s_{1s}) \leq 0$$

For the second softening branch: $\omega_1 = 0$; $\omega_7 = 0$; $\omega_8 \leq 0$

$$\omega_8 = s_1^i - h_3(\lambda_8) - s_{1r} \geq 0$$

$$\omega_8 = -s_1^i + h_3(\lambda_8) + s_{1r} \leq 0$$

$$\omega_8 - \omega_7 = -s_1^i - (h_1)\lambda_7 + (h_1)\lambda_1 + h_3(\lambda_8) + s_{1r} + s_{1u} - s_{1s} \leq 0$$

$$\omega_8 - \omega_7 + \omega_1 = -(h_2)\lambda_7 - (-h_2)\lambda_8 - (s_{1s} - s_{1r}) \leq 0$$

$$\omega_8 = -(h_2)\lambda_7 - (-h_2)\lambda_8 - (s_{1s} - s_{1r}) \leq 0$$

$$\text{Hence, } \begin{bmatrix} \omega_1 \\ \omega_7 \\ \omega_8 \end{bmatrix} = \begin{bmatrix} 1 \\ 0 \\ 0 \end{bmatrix} s_1^i - \begin{bmatrix} h_1 & (h_2 - h_1) & (h_3 - h_2) \\ h_1 & (-h_1) & 0 \\ 0 & h_2 & (-h_2) \end{bmatrix} \begin{bmatrix} \lambda_1 \\ \lambda_7 \\ \lambda_8 \end{bmatrix} - \begin{bmatrix} s_{1u} \\ (s_{1u} - s_{1s}) \\ (s_{1s} - s_{1r}) \end{bmatrix} \leq 0$$

Combining all yield functions, we obtain:

$$\begin{bmatrix} \omega_1 \\ \omega_2 \\ \omega_3 \\ \omega_4 \\ \omega_5 \\ \omega_6 \\ \omega_7 \\ \omega_8 \end{bmatrix} = \begin{bmatrix} 1 & \tan \gamma / \tau \\ 0 & 1 \\ -1 & \tan \beta / \tau \\ -1 & -\tan \beta / \tau \\ 0 & -1 \\ 1 & -\tan \gamma / \tau \\ 0 & 0 \\ 0 & 0 \end{bmatrix} \begin{bmatrix} s_1^i \\ s_2^i \end{bmatrix} - \begin{bmatrix} h_1 & h_1 & 0 & 0 & h_1 & h_1 & h_2 - h_1 & -h_2 \\ \tau h_1 & \tau h_1 & 0 & 0 & \tau h_1 & \tau h_1 & \tau(h_2 - h_1) & -\tau h_2 \\ 0 & 0 & 0 & 0 & 0 & 0 & 0 & 0 \\ 0 & 0 & 0 & 0 & 0 & 0 & 0 & 0 \\ \tau h_1 & \tau h_1 & 0 & 0 & \tau h_1 & \tau h_1 & \tau(h_2 - h_1) & -\tau h_2 \\ h_1 & h_1 & 0 & 0 & h_1 & h_1 & h_2 - h_1 & -h_2 \\ h_1 & h_1 & 0 & 0 & h_1 & h_1 & -h_1 & 0 \\ 0 & 0 & 0 & 0 & 0 & 0 & h_2 & -h_2 \end{bmatrix} \begin{bmatrix} \lambda_1 \\ \lambda_2 \\ \lambda_3 \\ \lambda_4 \\ \lambda_5 \\ \lambda_6 \\ \lambda_7 \\ \lambda_8 \end{bmatrix} - \begin{bmatrix} s_{1u} \\ s_{2u} \\ s_{1u} \\ s_{1u} \\ s_{2u} \\ s_{1u} \\ s_{1u} - s_{1s} \\ s_{1s} - s_{1r} \end{bmatrix} \leq 0$$

We can decompose as follows:

$$\omega^{aT} = [\omega_1 \quad \omega_2 \quad \omega_3 \quad \omega_4 \quad \omega_5 \quad \omega_6 \quad \omega_7 \quad \omega_8] \quad (7.5)$$

$$s^{aT} = [s_1^i \quad s_2^i]$$

$$\lambda^{aT} = [\lambda_1 \quad \lambda_2 \quad \lambda_3 \quad \lambda_4 \quad \lambda_5 \quad \lambda_6 \quad \lambda_7 \quad \lambda_8]$$

$$N^a = \begin{bmatrix} \tan \gamma / \tau & 1 & \tan \beta / \tau & -\tan \beta / \tau & -1 & -\tan \gamma / \tau & 0 & 0 \\ 1 & 0 & -1 & -1 & 0 & 1 & 0 & 0 \end{bmatrix}$$

$$H^a = \begin{bmatrix} h_1 & h_1 & 0 & 0 & h_1 & h_1 & h_2 - h_1 & -h_2 \\ \tau h_1 & \tau h_1 & 0 & 0 & \tau h_1 & \tau h_1 & \tau(h_2 - h_1) & -\tau h_2 \\ 0 & 0 & 0 & 0 & 0 & 0 & 0 & 0 \\ 0 & 0 & 0 & 0 & 0 & 0 & 0 & 0 \\ \tau h_1 & \tau h_1 & 0 & 0 & \tau h_1 & \tau h_1 & \tau(h_2 - h_1) & -\tau h_2 \\ h_1 & h_1 & 0 & 0 & h_1 & h_1 & h_2 - h_1 & -h_2 \\ h_1 & h_1 & 0 & 0 & h_1 & h_1 & -h_1 & 0 \\ 0 & 0 & 0 & 0 & 0 & 0 & h_2 & -h_2 \end{bmatrix}$$

$$R^{aT} = [s_{1u} \quad s_{2u} \quad s_{1u} \quad s_{1u} \quad s_{2u} \quad s_{1u} \quad (s_{1u} - s_{1s}) \quad (s_{1s} - s_{1r})]$$

where

$$\tau = \frac{s_{2u}}{s_{1u}}$$

$$h_1 = -\left(\frac{s_{1u} - s_{1s}}{\Delta_{p1}} \right)$$

$$h_2 = -\left(\frac{s_{1s} - s_{1r}}{\Delta_{p2} - \Delta_{p1}} \right)$$

7.4 Validation of Proposed Plasticity Components with Experimental Tests

The proposed piecewise yield function and softening rule have been implemented in a stepwise holonomic analysis approach (Tangaramvong and Tin-Loi 2010) with large scale MCP solver – GAMS/PATH (Dirkse and Ferris 1995). The stepwise holonomic scheme, which allows the approximation of plastic loading and elastic unloading of stresses, can predict the realistic path-dependent behaviors of structures. Both geometric and material nonlinearity were included in the analysis of CES structures. As mentioned earlier, the MATLAB-GAMS software link (Ferris 2005) has been used throughout this thesis to enable MATLAB software to assess all

the built-in solvers from GAMS as well as to visualize the models directly within MATLAB interface. Two CES column specimens C2 and C4 from Chen and Yeh (1996), and two CES beam-columns BC4 and BC5 from Al-Shahari et al. (2003) were employed for validation purpose. The accuracy of the proposed piecewise yield function as well as the softening rule have been evidenced through comparisons with relevant full-scaled concrete encased steel columns and beam-columns. The full description and structural detailing of the CES columns (C2, C4) and beam-columns (BC4, BC5) specimens can be found in Chapter 5 and 6, respectively.

Comparisons between full structural responses from the present analyses and the experimental tests for concrete encased steel columns and beam-columns were illustrated in Figures 7.11-7.14. Load and axial shortening responses for CES columns under axial compression for specimens C2 and C4 were shown in Figures 7.11-7.12, where P_{Prop} / P_{Test} ratios are 0.97 and 0.92, respectively. For CES beam-columns BC4 and BC5 under eccentric loadings, load and lateral deflection at mid-height were plotted for comparisons in Figures 7.13-7.14, where P_{Prop} / P_{Test} ratios are 0.93 and 0.90, respectively. It can be observed from Figures 7.13-7.14 which are the cases of beam-columns that the structural performances from the proposed analysis approach behave softer than those from the experimental tests. This might be resulted from the fact that the plasticity of the element was lumped to the hinges at each node which eventually forms the mechanism. However, such influence can be eliminated for columns having large depth to effective length ratio (D/kL) as for the cases of C2 and C4 in Figures 7.13-7.14. It is admitted that actual nonlinear responses with softening behavior are very challenging tasks for researchers to trace using simplified approaches. In general, the proposed simplified piecewise linear yield hyperplanes

and softening rule implemented in the stepwise holonomic analysis can predict the CES structural responses with sufficient accuracy, but with much less computational effort and time.

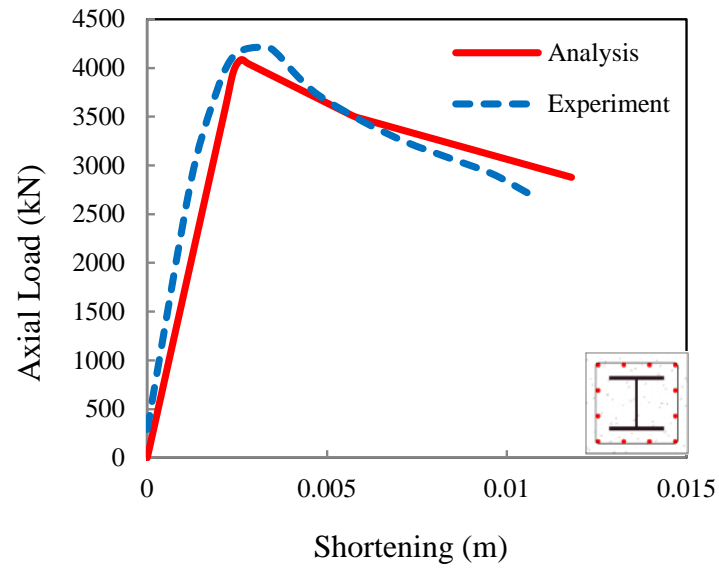


Figure 7.11: Load and axial shortening response from the present analysis and the experiment for H-shaped encased column specimen C2.

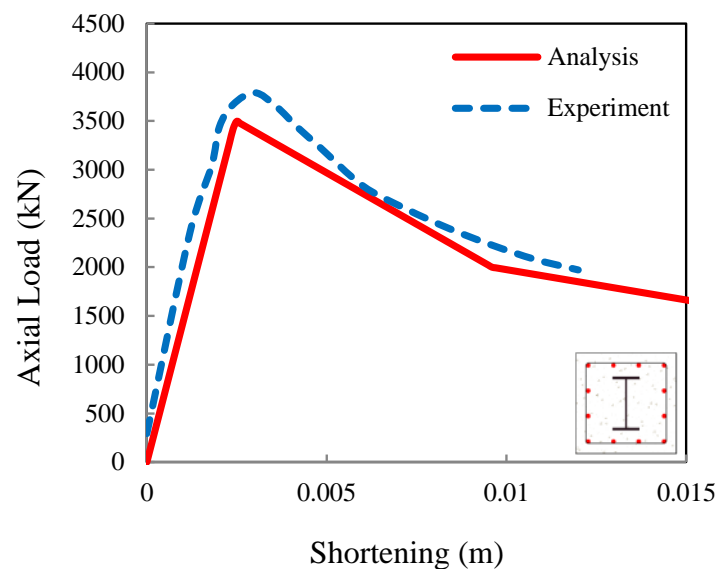


Figure 7.12: Load and axial shortening response from the present analysis and the experiment for I-shaped encased column specimen C4.

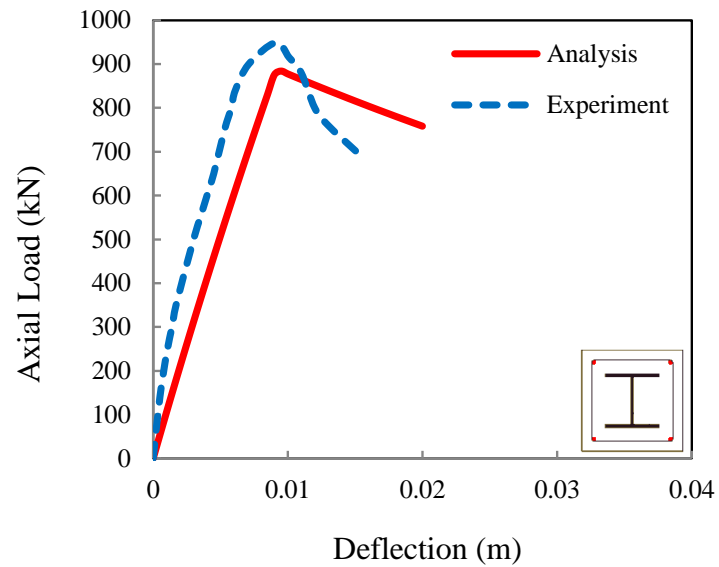


Figure 7.13: Load and lateral deflection response from the present analysis and the experiment for H-shaped encased beam-column specimen BC4.

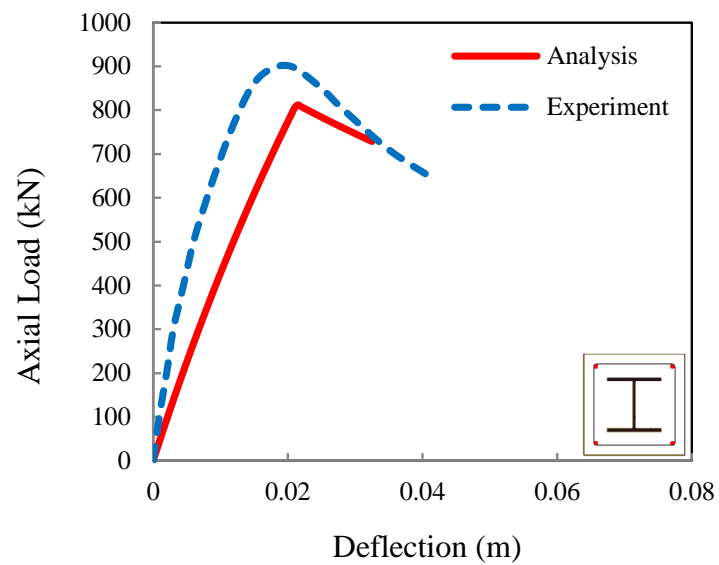


Figure 7.14: Load and lateral deflection response from the present analysis and the experiment for H-shaped encased beam-column specimen BC5.

7.5 Performance Assessment of CES Structures

7.5.1 Description of Illustrative Examples

This section aims to demonstrate the practical application of the proposed numerical approach to robustly assess the performance of CES composite structures. The nonlinear analyses have been performed using the novel piecewise linear yield function and softening rule implemented in the stepwise holonomic analysis method (Tangaramvong and Tin-Loi 2010) in corporation with GAMS/PATH (Dirkse and Ferris 1995). It should be worth mentioning that the global analyses begin with mesoscale simulation of composite cross-sections (i.e. under combined axial compression and bending moment) which act as vital elements to accurately predict the challenging softening behavior of CES composite structures. The appropriate attributes including the piecewise linear yield function and the softening rule have been set up using MATLAB Code.

Three examples have been carefully chosen to illustrate the overall behavior of CES composite structures, covering practical buildings such as low-rise and wide span, medium-rise, and slender. More importantly, in order to demonstrate the indispensable influence of softening simulation, two cases (i.e. Case A: perfectly plasticity model, and Case B: softening model) for columns have been carried out for each example. For all steel beams, pure bending model with perfectly plastic were assumed. The complete structural performance of CES structures have been traced and discussed along with the illustrations of event-by-event hinges formations. The full panoramas of the plastic hinge evolution have been illustrated for better understanding of the structural responses.

7.5.2 Example 1: Three-bay, two-story rigid frame

This first example considers a three-bay, two-story composite frame which consists of concrete encased steel columns and steel beams as shown in Figure 7.15. It is subjected to the increasing applied gravity loads and lateral loads (kN) by load multiplier α , and the top right sway displacement v (m) is recorded.

The gravity loads were applied at equal intervals of values 60 kN and 120 kN for exterior and interior, respectively. The lateral loads of 5 kN were applied at the nodes for each story. The properties exterior and interior CES columns are detailed in Table 7.1. For all steel beams, Young's modulus of 200 GPa and yield strength of 275 MPa were assumed. Steel profiles IPE400 and IPE600 were used respectively for exterior and interior beams, which corresponded to $S_{2u} = 327$ kNm and $S_{2u} = 878$ kNm.

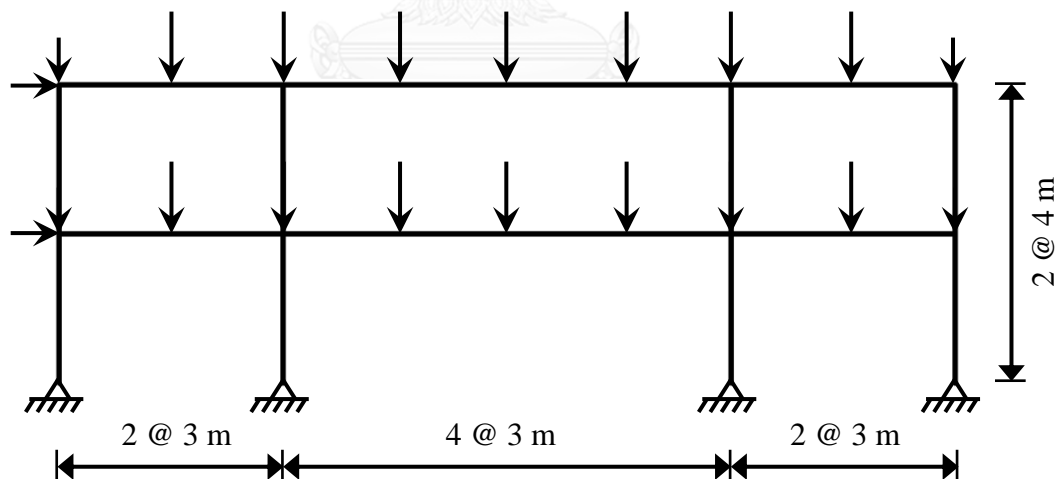
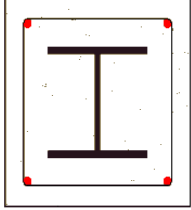
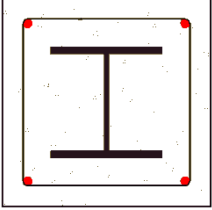
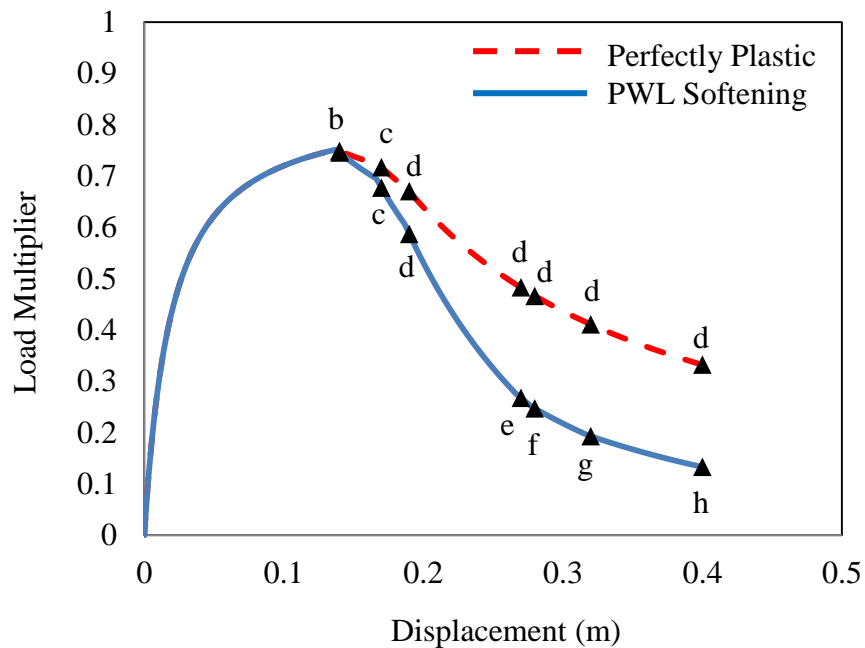


Figure 7.15: Example 1: Three-bay, two-story rigid frame.

Table 7.1: Properties of CES composite columns for example 1.

| Exterior Columns | | Interior Columns | |
|---|--|---|--|
|  | |  | |
| Concrete | 160 x 180 ($f'_c = 30$ MPa) | Concrete | 230 x 230 ($f'_c = 30$ MPa) |
| Steel | 68 x 100 x 4.5 x 7.6 ($f_{ys} = 355$ MPa) | Steel | 140 x 133 x 5 x 8 ($f_{ys} = 355$ MPa) |
| Rebar | 4 Ø12 ($f_{yr} = 400$ MPa) | Rebar | 4 Ø12 ($f_{yr} = 400$ MPa) |
| Stirrup | Ø8 @ 75 | Stirrup | Ø8 @ 75 |
| Capacity | $S_{Iu} = 1507$ kN, $S_{Is} = 834$ kN, $S_{Iv} = 697.6$ kN, $S_{Ii} = -683.352$ kN $S_{2u} = 42.627$ kNm | Capacity | $S_{Iu} = 2696$ kN, $S_{Is} = 1270$ kN, $S_{Iv} = 921.151$ kN, $S_{Ii} = -1205$ kN $S_{2u} = 90.737$ kNm |
| Softening | $h_1 = -12254.83$ kNm, $h_2 = -5595.16$ kNm | Softening | $h_1 = -27350.89$ kNm, $h_2 = -7387.58$ kNm |

**Figure 7.16:** Example 1: Responses of CES composite structures.

Nonlinear responses of CES composite structures for two cases, i.e. Case A: perfectly plastic with combined stresses (dash line) and Case B: piecewise linear softening with combined stresses (solid line), are compared in Figure 7.16. As expected, the difference between the two cases is the response after peak, which illustrates the significance of softening simulation.

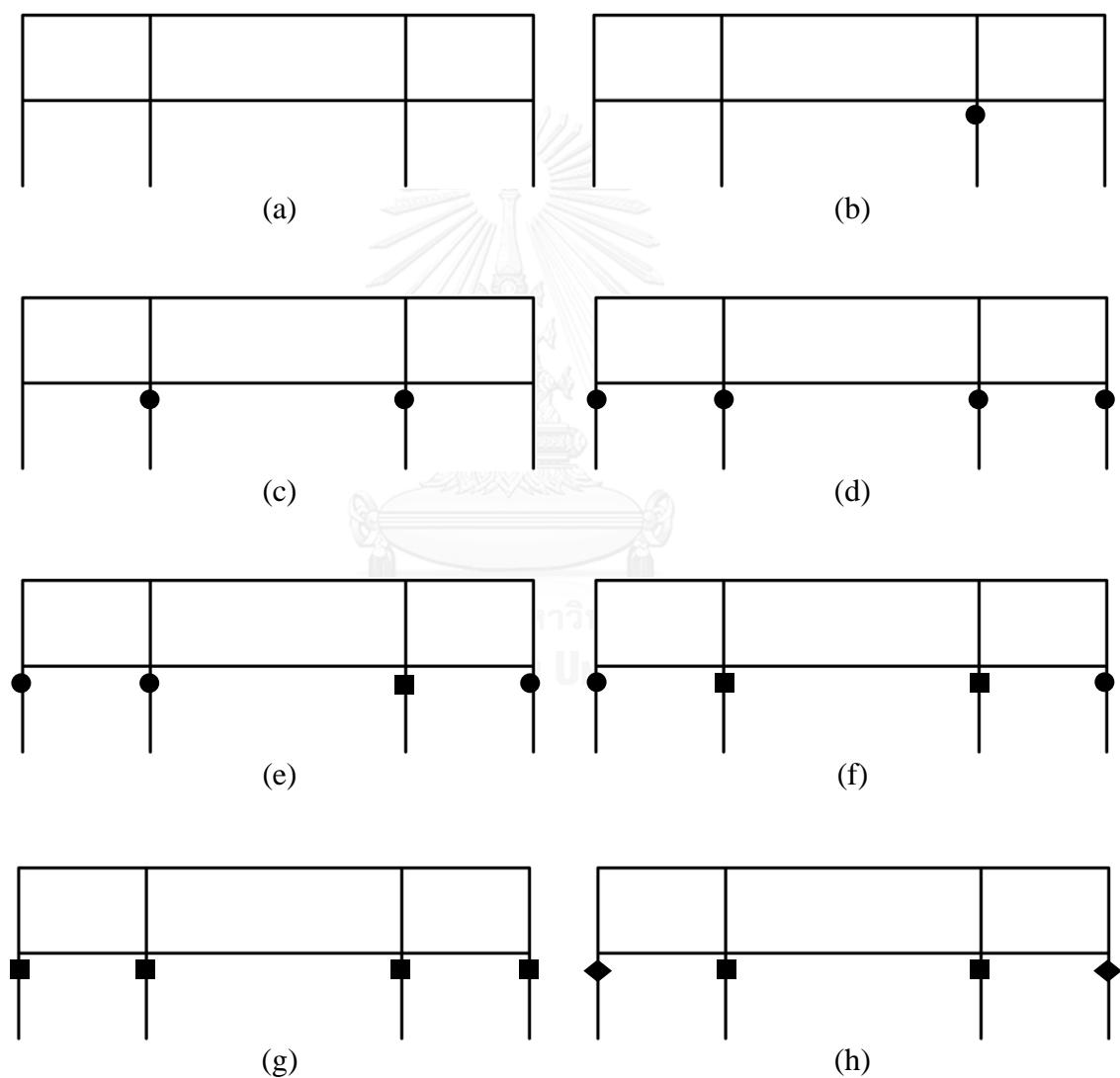


Figure 7.17: Examples 1: Hinge developments (● denotes hinge on perfectly plastic or 1st softening branch; ■, ♦ denote respectively hinge on 2nd, 3rd softening branch).

The formations and developments of hinges for both cases with perfectly plastic and with softening assumptions have been illustrated in Figure 7.17, where the labels (i.e. a to h) correspond to the states of structural performance in Figure 7.16. For Case A with the assumption of perfectly plastic, the hinge formations and developments are the same as Case B up to the state (d) and remain unchanged since there is no softening simulation included. From Figure 7.16 and Figure 7.17d-e, the difference became more significant when the softening of the hinge started to occur on the second softening branch for Case B, while the hinge in Case A still remain on the perfectly plastic portion. The peak load occurred at $\alpha = 0.75$ for $v = 0.14$ m although no hinge was formed yet (see Figure 7.17a). Slightly after attaining the maximum load, the first hinge occurred at the base column at $\alpha = 0.72$ for $v = 0.17$ m (i.e. Figure 7.17b).

7.5.3 Example 2: Five-bay, five-story rigid frame

The second example concerns a five-bay, five-story composite frame which consists of concrete encased steel columns and steel beams as shown in Figure 7.18. It is subjected to the increasing applied gravity loads and lateral loads (kN) by load multiplier α , and the top right sway displacement v (m) is recorded.

The gravity loads were applied at equal intervals of values 60 kN and 120 kN for exterior and interior, respectively. The lateral loads of 3 kN, 6 kN, 9 kN, 12 kN, and 15 kN were applied respectively at the nodes for each story. The properties all CES columns are detailed in Table 7.2. For all steel beams, Young's modulus of 200 GPa and yield strength of 275 MPa were assumed. Steel profiles IPE400 was used for all beams, which corresponded to $S_{2u} = 327$ kNm.

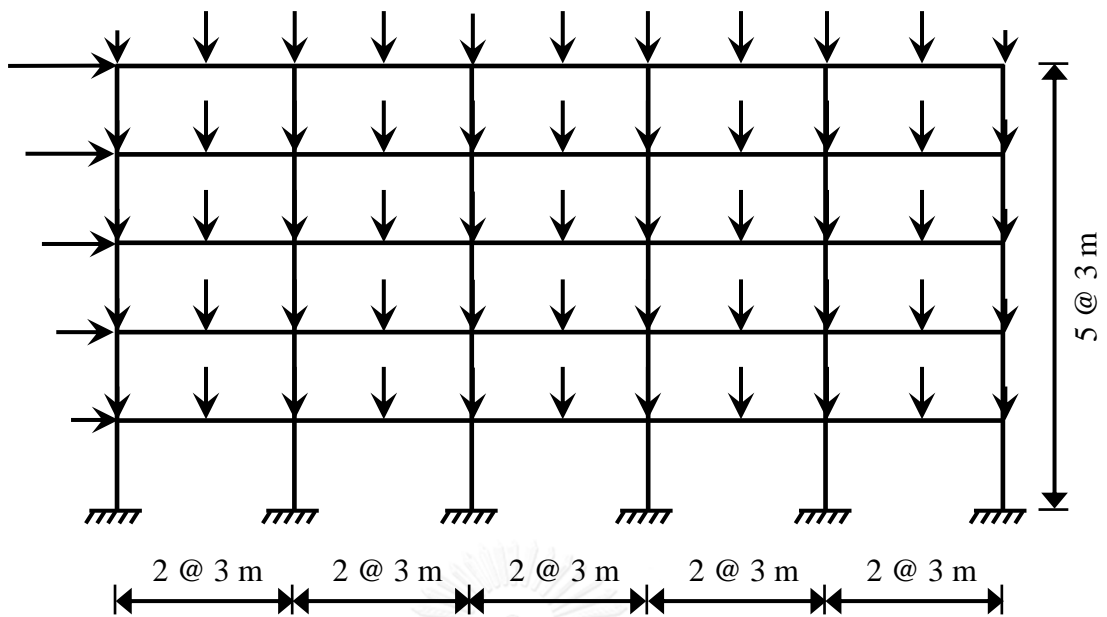


Figure 7.18: Examples 2: Five-bay, five-story rigid frame.

Table 7.2: Properties of CES composite columns for example 2.

| All Columns | |
|-------------|--|
| | |
| Concrete | 280 x 280 ($f'_c = 30$ MPa) |
| Steel | 75 x 150 x 5 x 7 ($f_{ys} = 355$ MPa) |
| Rebar | 12 $\text{Ø}15.9$ ($f_{yr} = 400$ MPa) |
| Stirrup | $\text{Ø}8 @ 75$ |
| Capacity | $S_{1u} = 3895$ kN, $S_{1s} = 3050$ kN, $S_{1r} = 1950$ kN, $S_{1t} = -1595$ kN $S_{2u} = 148.952$ kNm |
| Softening | $h_1 = -69051.59$ kNm, $h_2 = -33380.08$ kNm |

Figure 7.19 presents the comparison between two nonlinear responses of composite structures based on the assumptions of perfectly plastic with combined stresses (dash line) and piecewise linear softening with combined stresses (solid line). Again, only the post-peak responses show the differences which confirm the importance of softening behavior. For a better understanding, a series of hinge formations and evolutions have been displayed in Figure 7.20 for both Cases A and B.

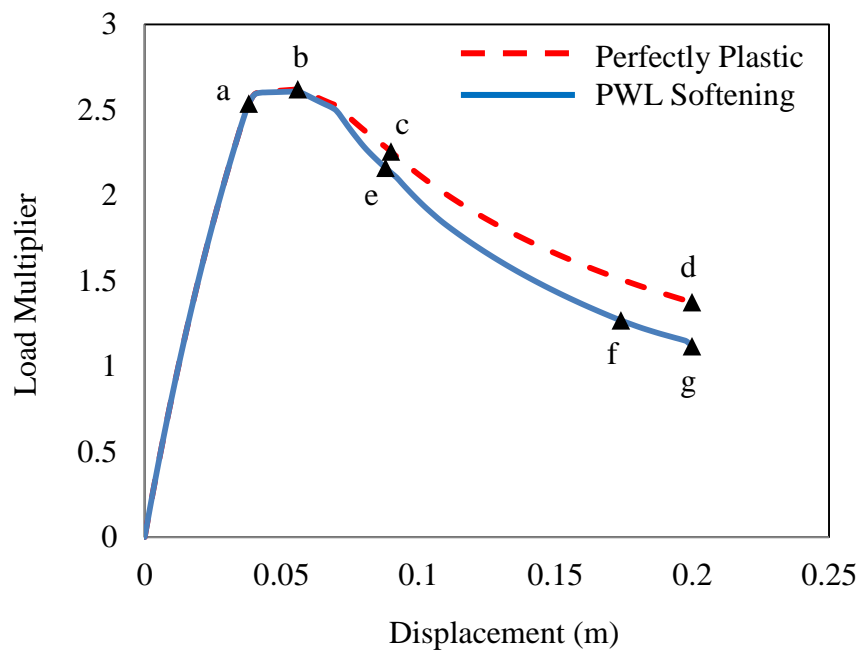


Figure 7.19: Examples 2: Responses of CES composite structures.

The labels on the response curves in Figure 7.19 correspond to the critical states of hinge formation and development for Cases A and B in Figure 7.20. The computations have shown that for both cases the first yielding hinges occurred in a base column at $\alpha = 2.54$ for $v = 0.038$ m (see Figure 7.20a), and the state of hinge dispositions when reaching the peak load is presented in Figure 7.20b which corresponds to $\alpha = 2.61$ for $v = 0.054$ m. For Case A, a steel beam in story 1 of first

bay started to yield at $\alpha = 2.57$ for $v = 0.064$ m, and the unload event occurred at $\alpha = 2.5$ for $v = 0.072$ m (see Figure 7.20c).

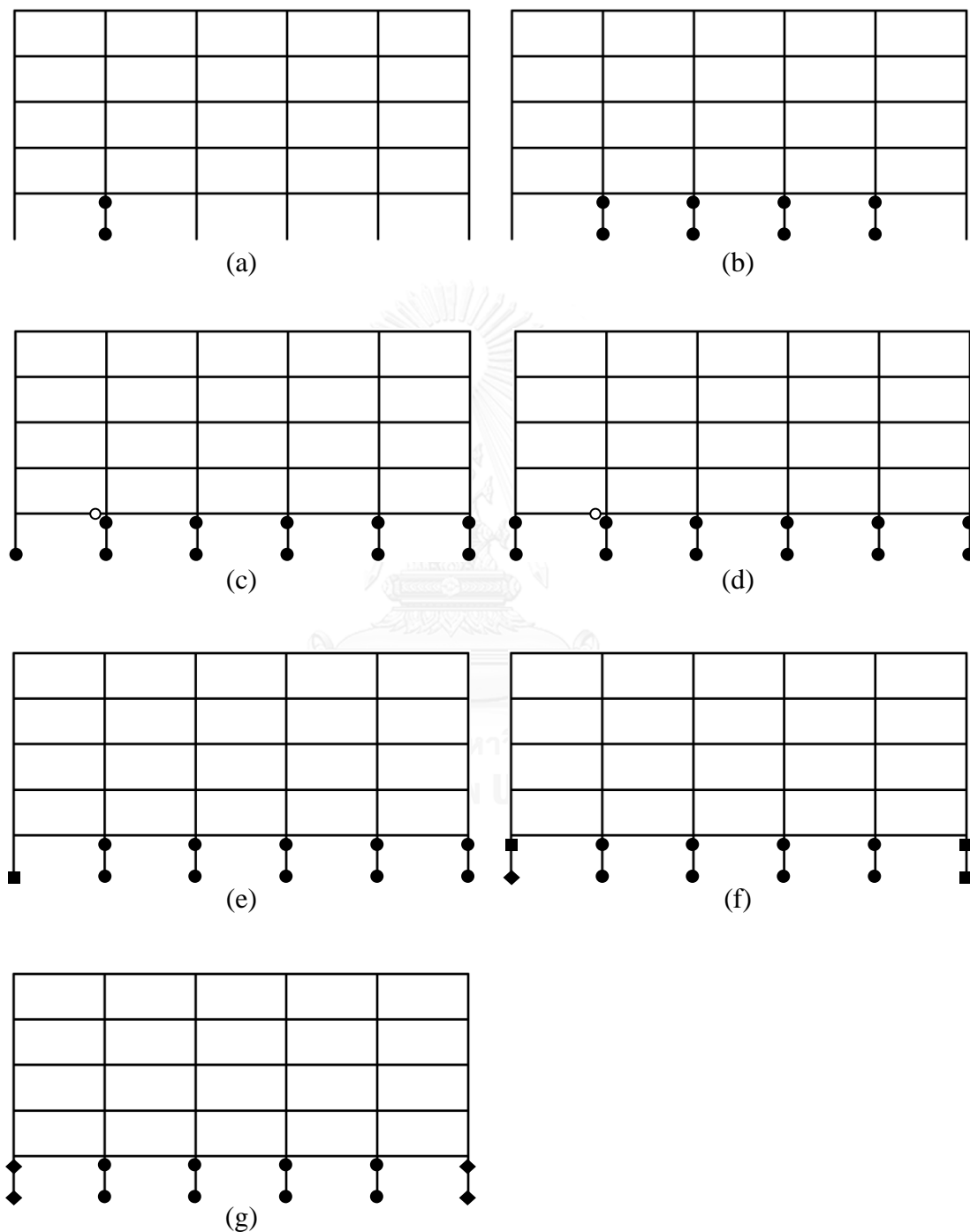


Figure 7.20: Examples 2: Hinge developments (● denotes hinge on perfectly plastic or 1st softening branch; ■, ◆ denote respectively hinge on 2nd, 3rd softening branch; and ○ denotes unloading hinge).

Figure 7.20d illustrates the final state of hinge dispositions for Case A (i.e. perfectly plastic) corresponding to $\alpha = 1.37$ for $v = 0.2$ m. When softening behavior is taken into account, the second softening branch was activated (Figure 7.20e) at $\alpha = 2.16$ for $v = 0.088$ m on the intersection of yield hyperplane 1 and 2 for a base column at the first grid. In Figure 7.20f, the third piecewise linear softening branch was further developed at $\alpha = 1.27$ for $v = 0.174$ m from the previous second portion location. The final event of hinge formations for Case B is displayed in Figure 7.20g at $\alpha = 1.12$ for $v = 0.2$ m.

7.5.4 Example 3: Three-bay, twelve-story rigid frame

This three-bay, twelve-story frame is a practical example of a CES composite building which is composed of concrete encased steel columns and steel beams as shown in Figure 7.21. It is subjected to the increasing applied gravity loads and lateral loads (kN) by load multiplier α , and the top right sway displacement v (m) is recorded.

The gravity loads were applied at equal intervals of 5 kN. The lateral loads were divided into three groups for every four stories. They were applied respectively at each node of the groups with magnitudes of 1 kN, 2 kN, and 3 kN. The columns were categorized into two types, i.e. lower columns from first to sixth floor, and upper columns from seventh to twelfth floor. The properties of all CES composite columns are detailed in Table 7.3. For all steel beams, Young's modulus of 200 GPa and yield strength of 275 MPa were assumed. Steel profiles IPE400 was used for all beams, which corresponded to $S_{2u} = 327$ kNm.

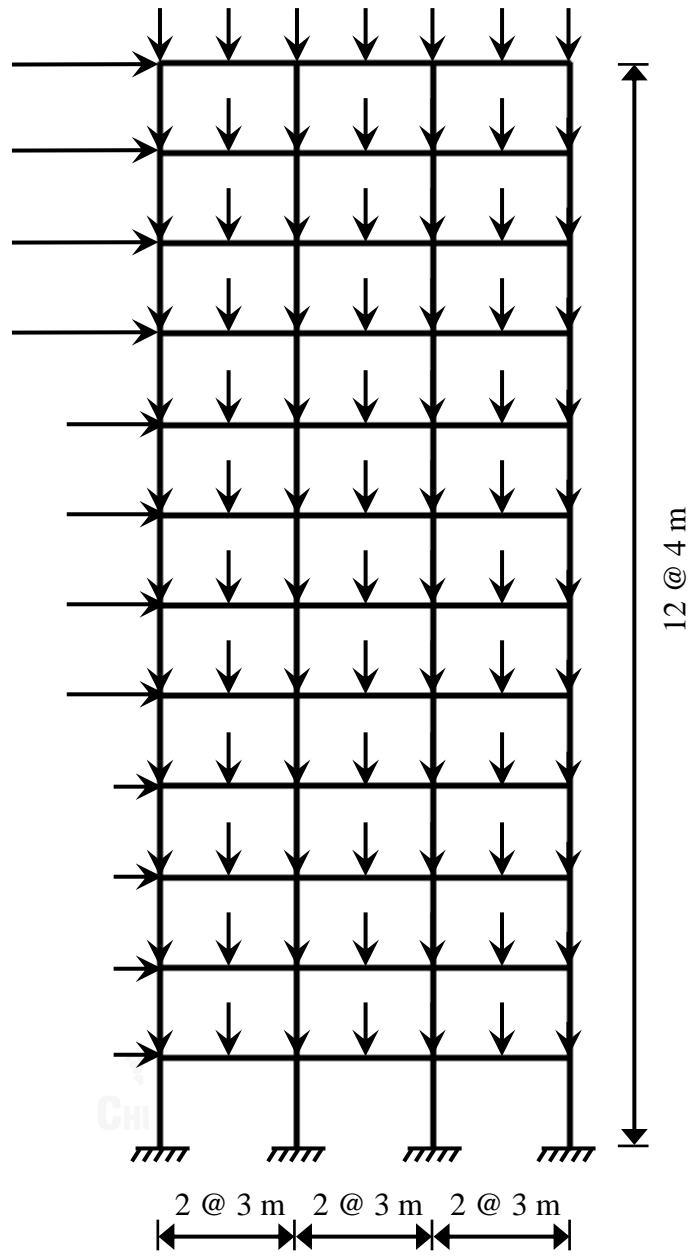
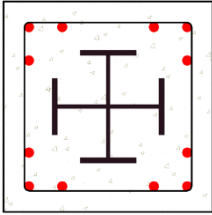
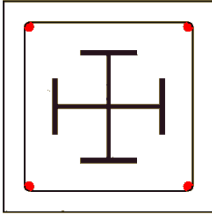


Figure 7.21: Examples 3: Three-bay, twelve-story rigid frame.

Table 7.3: Properties of CES composite columns for example 3.

| Columns for floors 1 – 6 | | Columns for floors 7 – 12 | |
|---|---|---|---|
|  | |  | |
| Concrete | 280 x 280 ($f'_c = 50$ MPa) | Concrete | 280 x 280 ($f'_c = 30$ MPa) |
| Steel | (2) 175 x 90 x 5 x 8 ($f_{ys} = 460$ MPa) | Steel | (2) 175 x 90 x 5 x 8 ($f_{ys} = 355$ MPa) |
| Rebar | 12 Ø15.9 ($f_{yr} = 400$ MPa) | Rebar | 4 Ø15.9 ($f_{yr} = 400$ MPa) |
| Stirrup | Ø8 @ 35 | Stirrup | Ø8 @ 35 |
| Capacity | $S_{Iu} = 6543$ kN, $S_{Is} = 5712$ kN, $S_{Ir} = 5586$ kN, $S_{It} = -2998$ kN $S_{2u} = 229.51$ kNm | Capacity | $S_{Iu} = 4324$ kN, $S_{Is} = 4100$ kN, $S_{Ir} = 3302$ kN, $S_{It} = -1945$ kN $S_{2u} = 154.33$ kNm |
| Softening | $h_1 = -67100.88$ kNm, $h_2 = -8758.73$ kNm | Softening | $h_1 = -19924.96$ kNm, $h_2 = -15039.50$ kNm |

For clarity, various critical events of hinge evolutions have been drawn in Figure 7.22 for the cases of perfectly plastic and piecewise linear softening assumptions under combined stresses. These hinge illustrations are very informative to help understand the behavior of CES structure under loadings in each incremental step, and to picture the overall structural performance as well. The complete nonlinear responses of composite frame have been successfully traced and compared in Figure 7.23, even though the challenging snap-back response exists. Only the post-peak responses are different due to assumption of softening laws. The labels on the response curves in Figure 7.23 correspond to the critical events of hinge formations and developments as presented in Figure 7.22. The hinge evolutions for Case A started from Figures 7.22 (a – d), and for Case B started from Figures 7.22 (a, e – i).

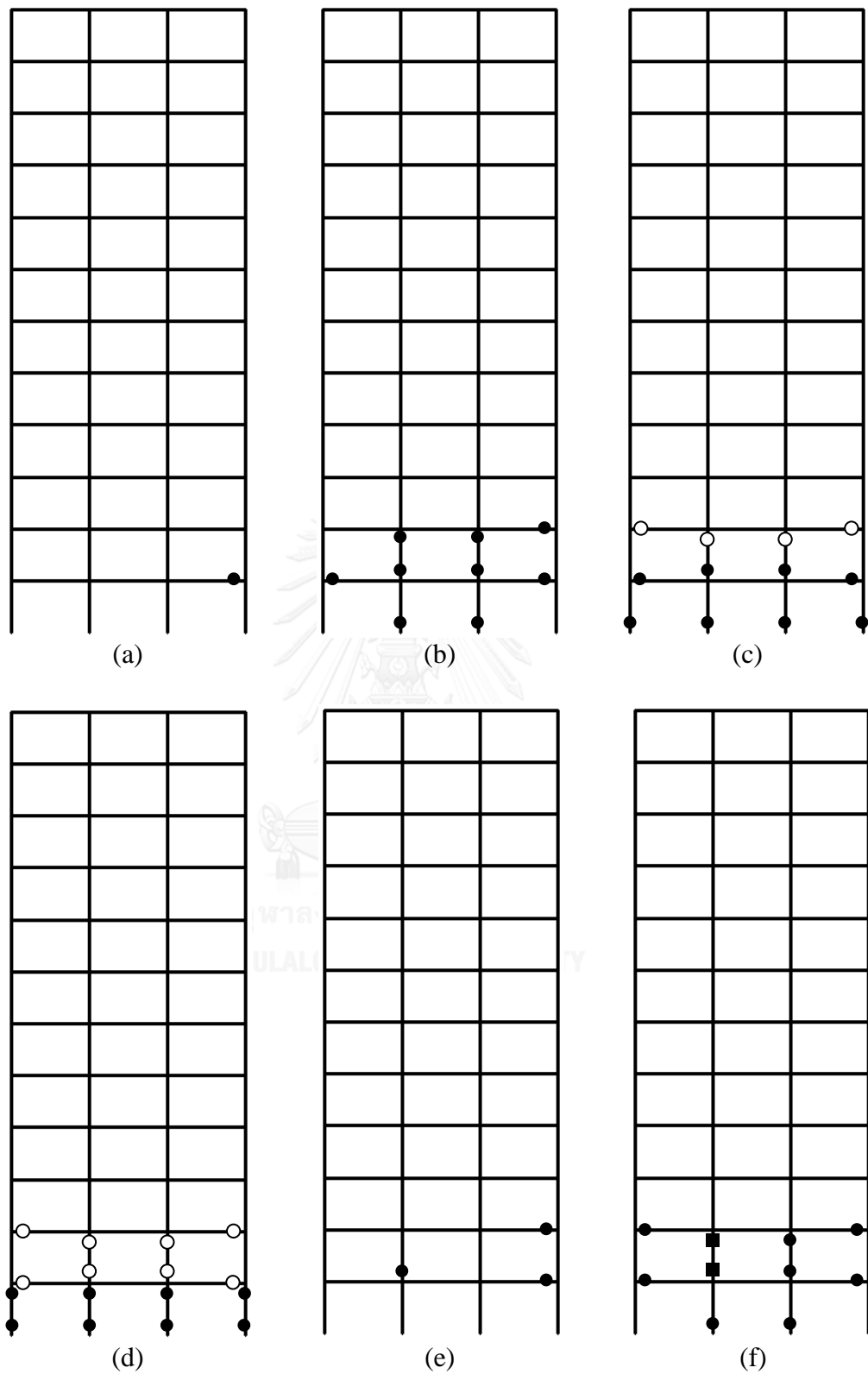


Figure 7.22: Examples 3: Hinge developments (\bullet denotes hinge on perfectly plastic or 1st softening branch; \blacksquare , \blacklozenge denote respectively hinge on 2nd, 3rd softening branch; and \circ denotes unloading hinge)

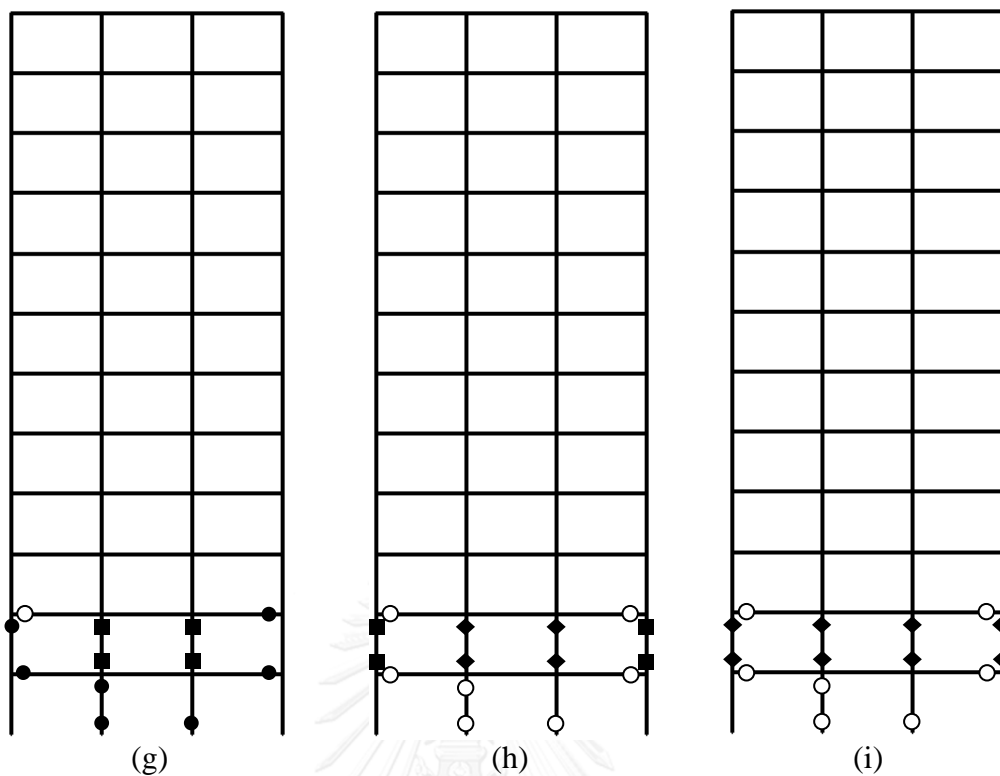


Figure 7.22: Examples 3: Hinge developments (● denotes hinge on perfectly plastic or 1st softening branch; ■, ◆ denote respectively hinge on 2nd, 3rd softening branch; and ○ denotes unloading hinge) – *Cont.*

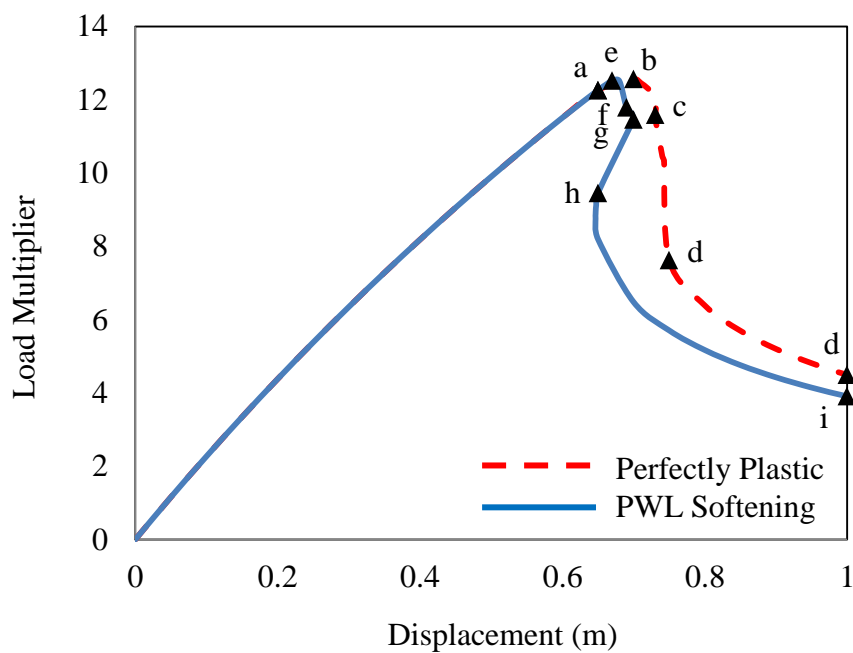


Figure 7.23: Examples 3: Responses of CES composite structures.

In Case A, a plastic hinge was firstly formed in a steel beam section at $\alpha = 12.26$ for $v = 0.65$ m (Figure 7.22a). When attaining the limit load level $\alpha = 12.57$ for $v = 0.7$ m (Figure 7.22b), more plastic hinges spread to other beam locations and the composite columns started to soften under combined stresses following the first softening path. As the load factor kept increasing, the unloading hinges occurred in steel beams and composite columns as shown in Figure 7.22c at $\alpha = 11.59$ for $v = 0.73$ m in order to maintain equilibriums. After unloading hinges were formed at many locations of both beams and columns, the structure became susceptible to sudden loss of strength and stability. It is best to mention that with the small increasing of displacement (i.e. from $v = 0.73$ m to 0.75m), the load multiplication factor α dropped significantly from 11.59 to 7.63. This phenomenon can be illustrated from Figure 7.22c and Figure 7.23. The computation terminated at $\alpha = 4.49$ for $v = 1$ m which was considered to violate the small deflection assumption, and the corresponding event was displayed in Figure 7.22d.

In Case B, the first plastic hinge also occurred at the same location and load factor as in Case A. The maximum load limit in this softening case was attained at $\alpha = 12.52$ for $v = 0.67$ m and the corresponding hinge formation is presented in Figure 7.22e which shows more plastic formation in steel beams and first slope of plastic softening in composite column. The load factor decreased to $\alpha = 11.79$ for $v = 0.69$ m as a composite column in the second floor underwent softening along the second branch (see Figure 7.22f). The unloading hinge in steel beam started to form at $\alpha = 11.46$ for $v = 0.7$ m as in Figure 7.22g, while more composite columns exhibited more softening hinges. The snap-back response occurred when there were many unloading

hinges formed at critical beam sections as the composite columns became very soft (viz. in the third residual softening branch). This phenomenon has been clearly illustrated by observing Figure 7.22h and Figure 7.23 at load level $\alpha = 9.46$ for $\nu = 0.65$ m. The final state of hinge evolution, chosen to be at $\alpha = 3.91$ for $\nu = 1$ m, has been plotted in Figure 7.22i which also shows the critical soft story when the hinge attain its residual softening stage in all composite columns.

7.6 Strengthening of CES Structures with Common Steel Bracings

7.6.1 Description of Retrofitted Structures

The performance of concrete encased steel composite frames has been fully traced and investigated using the proposed numerical approach. This section aims to retrofit the composite structures used in the previous section by means of steel bracings and compare their efficiency. Common steel bracing systems have been carefully selected to reflect the practical design applications. In order to compare various bracing configurations fair and square, the steel profile for bracing members were selected so that the total weight of each bracing systems are marginally equal. The bracing configurations in this study include the followings: X-type, V-type, Inverted V-type, Eccentrically Inverted V-type, and Mega X-type. It should be noted that all properties (including materials, loadings, boundary conditions, analysis approach,...etc.) used in the original CES frames from Example 1 to 3 remains unchanged, only steel braces have been added to the existing structures. For all analyses, CES columns were simulated using the proposed combined stresses model with piecewise linear softening law, and the perfectly plastic assumption were assumed for all bracing members.

7.6.2 Example 4: Strengthening a three-bay, two-story rigid frame

This example considers three types of bracing configurations to strengthen the existing CES frame in example 1. Typical bracing systems were carefully selected, viz. inverted V-bracing (Figure 7.24), eccentrically inverted V-bracing (Figure 7.25), and mega X-bracing (Figure 7.26). The steel profiles HEAA180, HEA200, and HEAA180 were employed respectively for inverted V-bracing, eccentrically inverted V-bracing, and mega X-bracing. The difference in steel weight between bracing configurations is minimal, i.e. 2.2%. Steel Young's modulus of 200 GPa and yield strength of 275 MPa were assumed. The corresponding capacities for HEAA180 are $S_{1u} = 913$ kN, $S_{2u} = 58.9$ kNm; and $S_{1u} = 1346$ kN, $S_{2u} = 107$ kNm for HEA200.

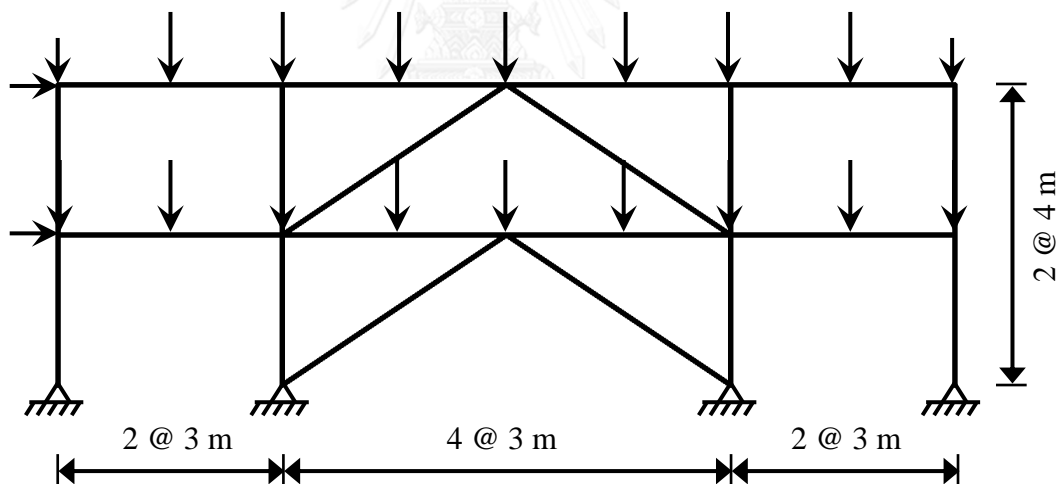


Figure 7.24: Examples 4: Inverted V-bracing.

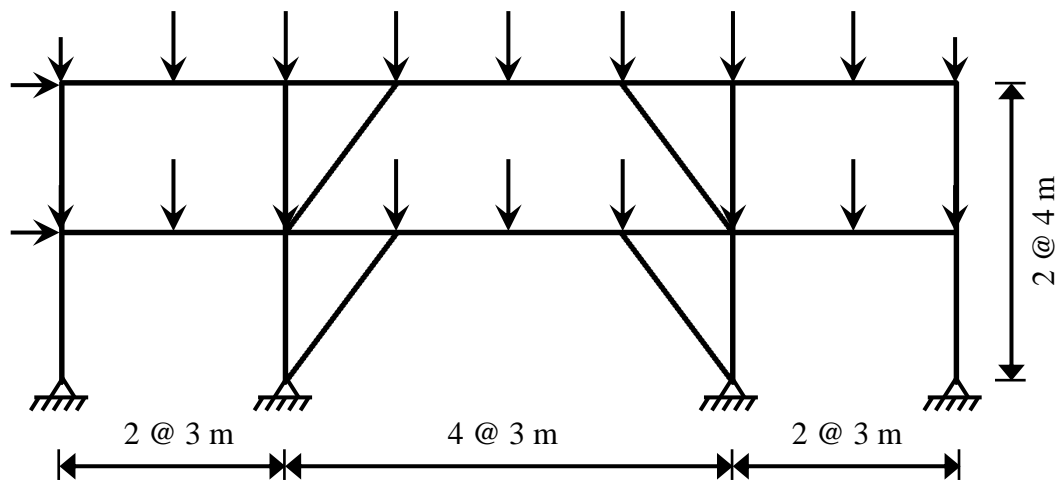


Figure 7.25: Examples 4: Eccentrically Inverted V-bracing.

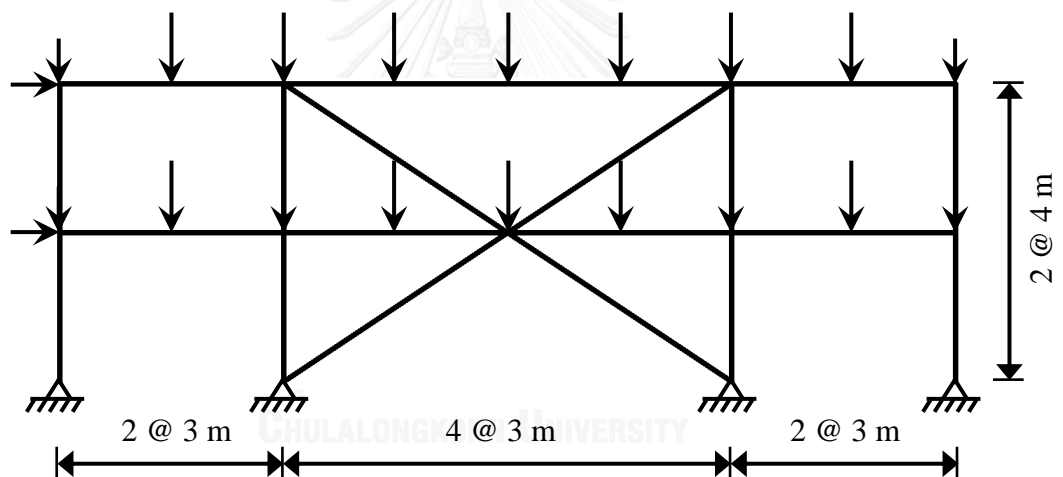


Figure 7.26: Examples 4: Mega X-bracing.

The complete structural responses of the CES structures with and without retrofitting have been presented in Figure 7.27 which is the load factor versus the top right sway displacement. At peak load level, the load factors with their corresponding displacements for inverted V-bracing, eccentrically inverted V-bracing, and mega X-bracing are $\alpha = 2.83$ with $v = 0.0005$ m, $\alpha = 2.81$ with $v = 0.0017$ m, and $\alpha = 2.08$ with $v = 0.01$ m, respectively. For a better understanding into structural performance, hinge

formations at peak load have been illustrated in Figure 7.28 for all bracing systems as well as the original CES structure. The computations have shown that both the concentrically and eccentrically inverted V-bracings provided better capacity than the mega X-bracing approximately 35%. Although, the maximum load from concentrically and eccentrically inverted V-bracings are more or less the same, but the overall responses are different; which demonstrates the important roles of full structural investigation. The eccentrically inverted V-braced structures are more ductile than the concentric ones but less stiff. The retrofitted structures using mega X-braces are both stiff and ductile. Comparing to the original unbraced CES structures, the conventional steel bracings enhance mainly the peak strength (i.e. from 2.8 to 3.7 times of original frame in this example) but deteriorate the ductility of the structures. It is worth mentioning that ductility is very important for the new trend of structural design, viz. performance-based design, due to its effectiveness of energy dissipation. For unbraced frame, no yielding occurred up to the peak load. Whereas for retrofitted frames, plastic hinges were firstly formed at some steel beams and then evolved significantly for eccentrically and concentrically inverted V-braced structures. This kind of hinge evolution is typical for structure dominated by gravity forces. Only the mega X-braces were found yielding due to the combined stresses.

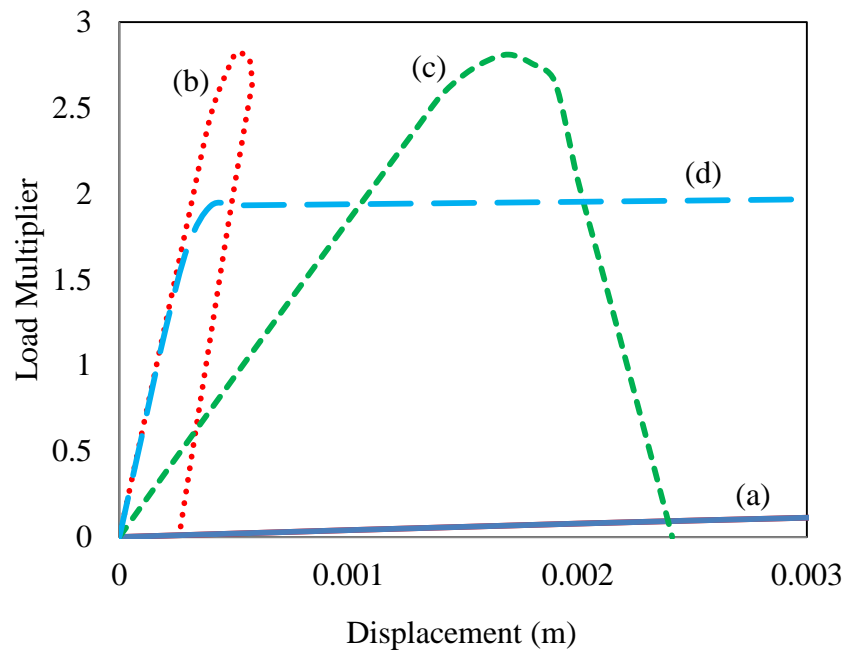


Figure 7.27: Examples 4: Responses of CES structures before and after retrofitting.

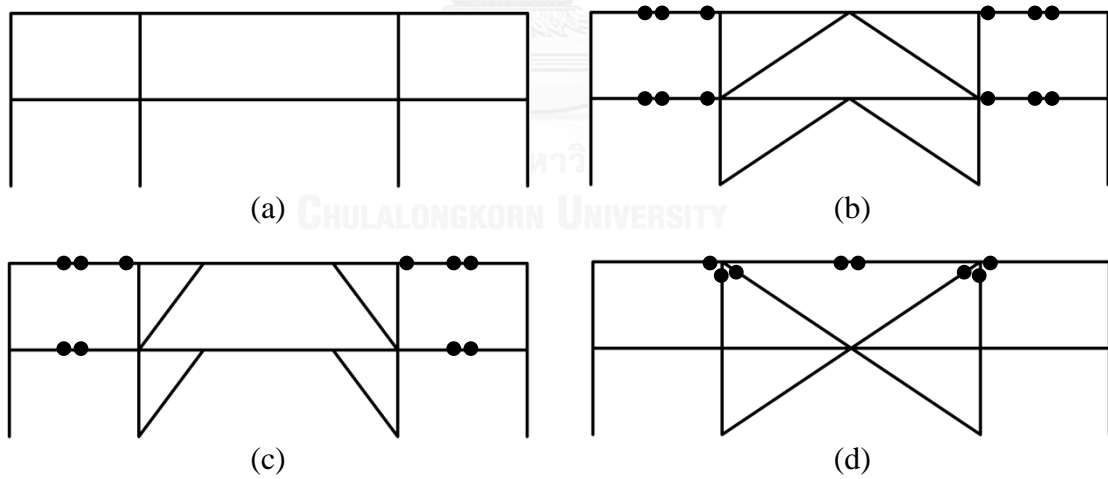


Figure 7.28: Examples 4: Hinge formations at peak load (● denotes hinge on perfectly plastic).

7.6.3 Example 5: Strengthening a five-bay, five-story rigid frame

The medium-rise rigid CES frame in example 2 has been retrofitted by three types of steel bracing system, i.e. inverted V-bracing, V-bracing, and X-bracing as shown in Figures 7.29-7.31. All steel braces were pinned-connected. Two steel sections were carefully selected to have the same structural weight (i.e. 0.2% difference). Inverted V-bracing and V-bracing were employed with profiles HEA200, and HEB120 was chosen for X-bracing. Steel Young's modulus of 200 GPa and yield strength of 275 MPa were adopted. The corresponding capacities for HEA200 are $S_{1u} = 1346$ kN, $S_{2u} = 107$ kNm; and for HEB120 are $S_{1u} = 850$ kN, $S_{2u} = 41.3$ kNm.

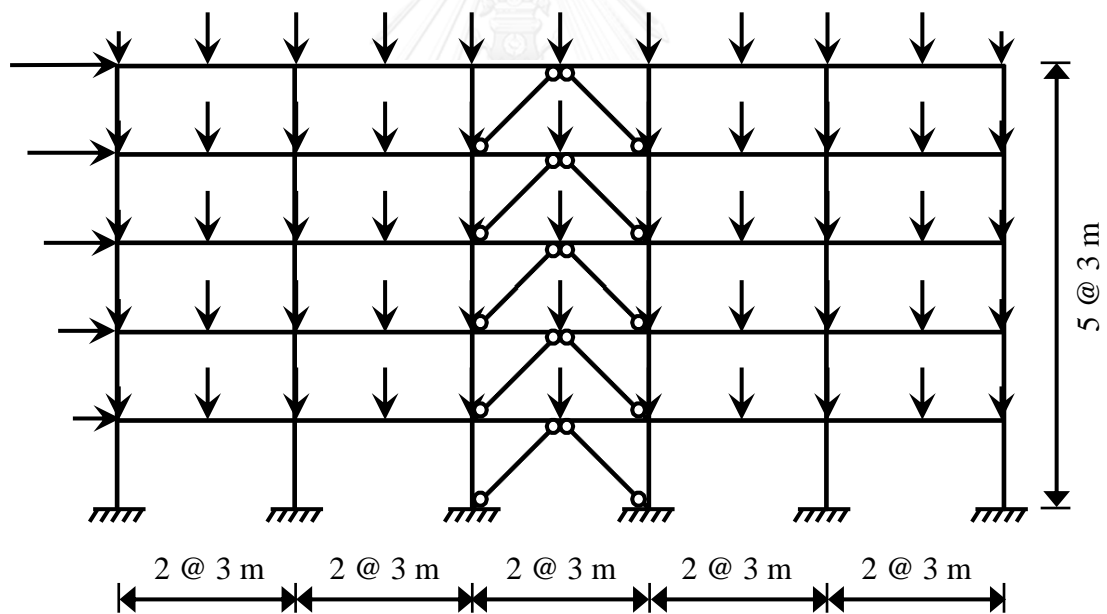


Figure 7.29: Examples 5: Inverted V-bracing.

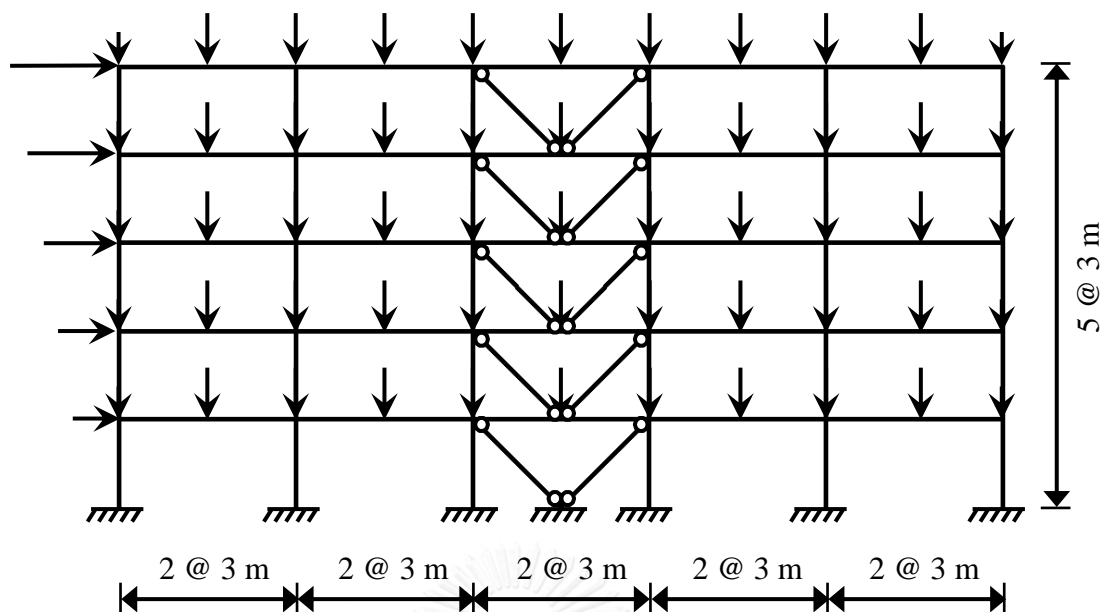


Figure 7.30: Examples 5: V-bracing.

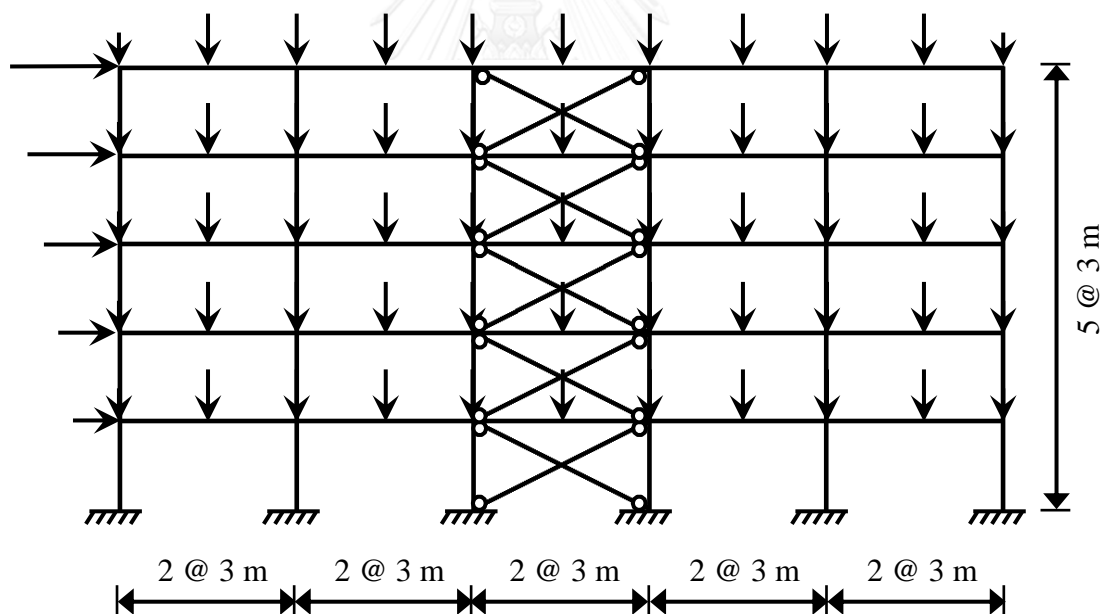


Figure 7.31: Examples 5: X-bracing.

The full structural response comparisons between unbraced CES composite frame and various bracing systems have been plotted in Figure 7.32. The labels on the figures denote the types of composite frame corresponding to the curves.

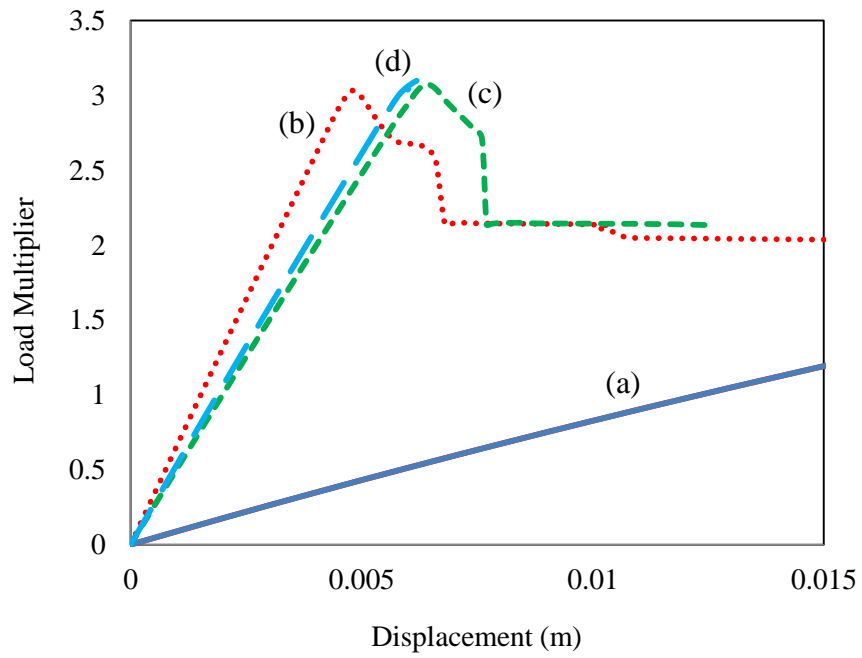


Figure 7.32: Examples 5: Responses of CES structures before and after retrofitting.

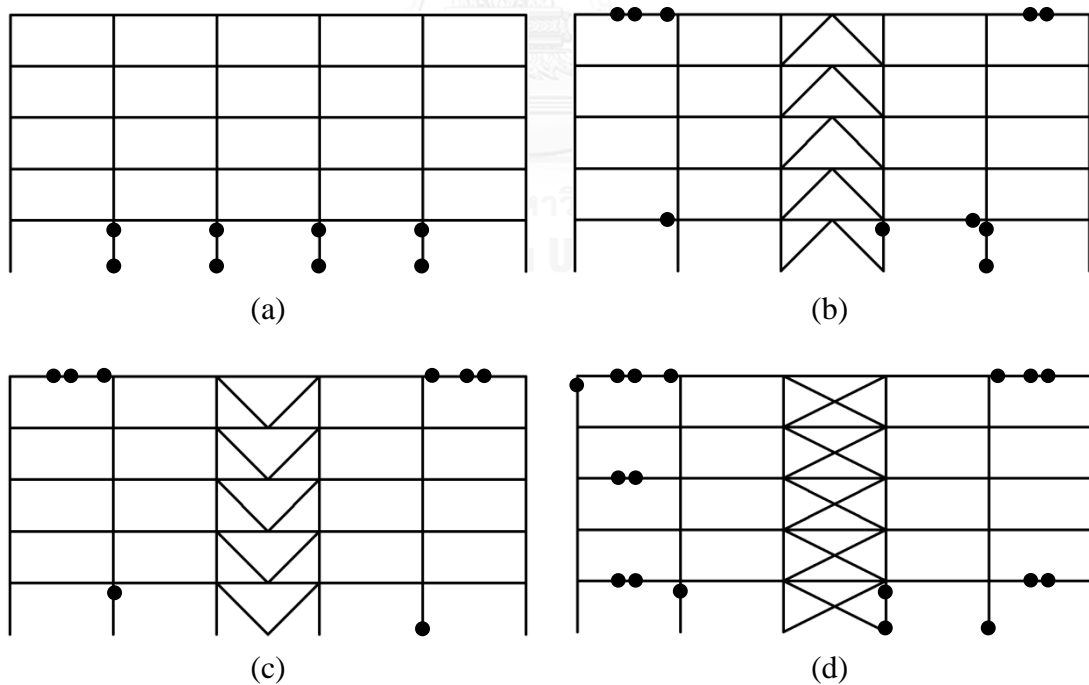


Figure 7.33: Examples 5: Hinge formations at peak load (• denotes hinge on perfectly plastic or 1st softening branch).

The maximum load factors of the three braced structures are practically the same, i.e. $\alpha = 3.03$, $\alpha = 3.07$, and $\alpha = 3.11$ for inverted V-bracing, V-bracing, and X-bracing, respectively. However, V- and X-braced frames are almost identical but softer than the inverted V-braced one. The enhancement from steel braces increased peak load capacity of the frame (i.e. 1.19 times in this case), but the post-peak response became significantly more brittle. The states of hinge formations for each CES structure have been illustrated in Figure 7.33 for further investigating the structural response. It is observed that many CES columns at the base of existing frame had yielded at the state of peak load (see Figure 7.33a) due to the combined stresses from gravity and lateral forces. However, the hinge developments have changed after strengthening with steel braces. For all of the three braced structures, plastic hinges were found in steel beam sections and the softening hinges in the columns were significantly reduced. This transformation is expected due to the fact that the steel braces helped resisting the lateral force and the columns absorbed mainly the gravity load. The hinge dispositions at peak load for the braced structures are displayed in Figures 7.33b-d. It is noticed that no plasticity was developed in the bracing members, since the unloading in the beam occurred after attaining the peak load which caused the sudden capacity drop or snap-through response when the columns underwent the softening behaviors.

7.6.4 Example 6: Strengthening a three-bay, twelve-story rigid frame

This example concerns the retrofitting of an existing twelve-story CES composite frame in example 3 by means of typical steel bracing systems. Three configurations of bracing were selected, i.e. inverted V-bracing, X-bracing, and mega X-bracing, as shown in Figures 7.34-35.

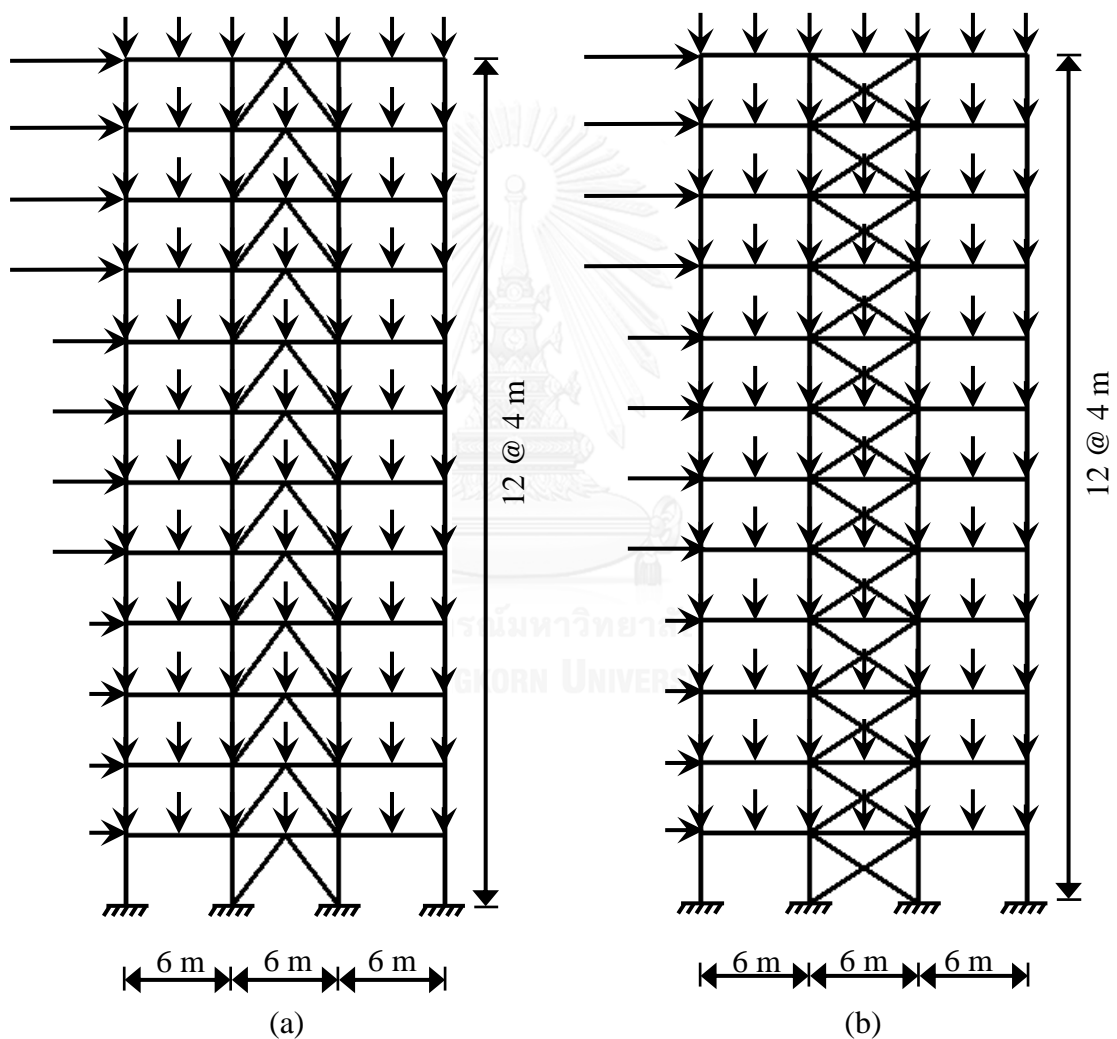


Figure 7.34: Examples 6: (a) Inverted V-bracing, (b) X-bracing.

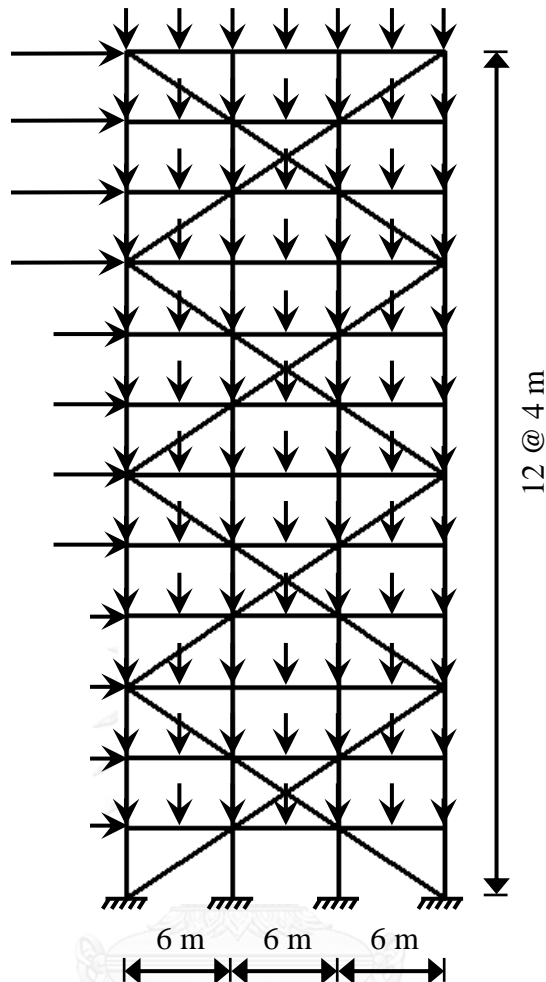


Figure 7.35: Examples 6: Mega X-bracing.

The steel profile HEA200 was employed for the inverted V-bracing, and HEAA180 section was adopted for both X- and mega X-bracings. The steel profiles were selected so that the steel weights of each bracing configurations are marginally different, i.e. 2.2%. Steel Young's modulus of 200 GPa and yield strength of 275 MPa were used for all bracing members. The corresponding capacities for HEA200 are $S_{1u} = 1346$ kN, $S_{2u} = 107$ kNm; and for HEAA180 are $S_{1u} = 913$ kN, $S_{2u} = 58.9$ kNm.

The comparisons between structural performances (load factor vs. top right sway displacement) of the existing and retrofitting composite structures have been illustrated in the Figure 7.36 whose labels referred to the types of structure being considered. For further clarity, the dispositions of plastic hinges for unbraced and braced frames were plotted in Figure 7.37 at the load level of peak load. The levels of plastic softening occurred in the CES columns have been made obvious for each state of the three softening branches, as well as the plastic hinge formed in any beams and bracing members.

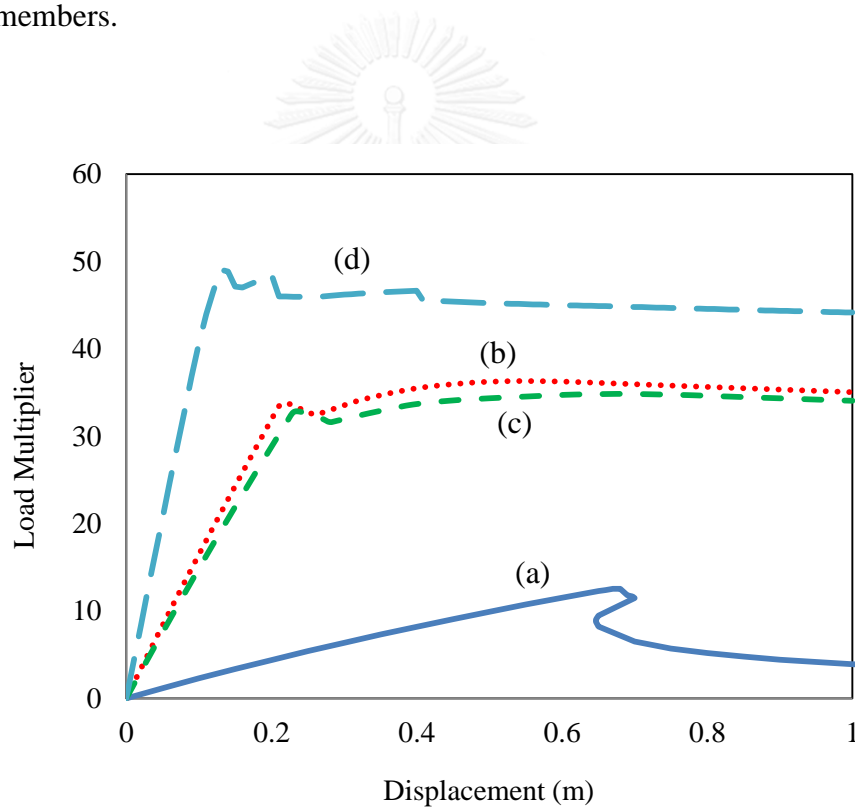


Figure 7.36: Examples 6: Responses of CES structures before and after retrofitting.

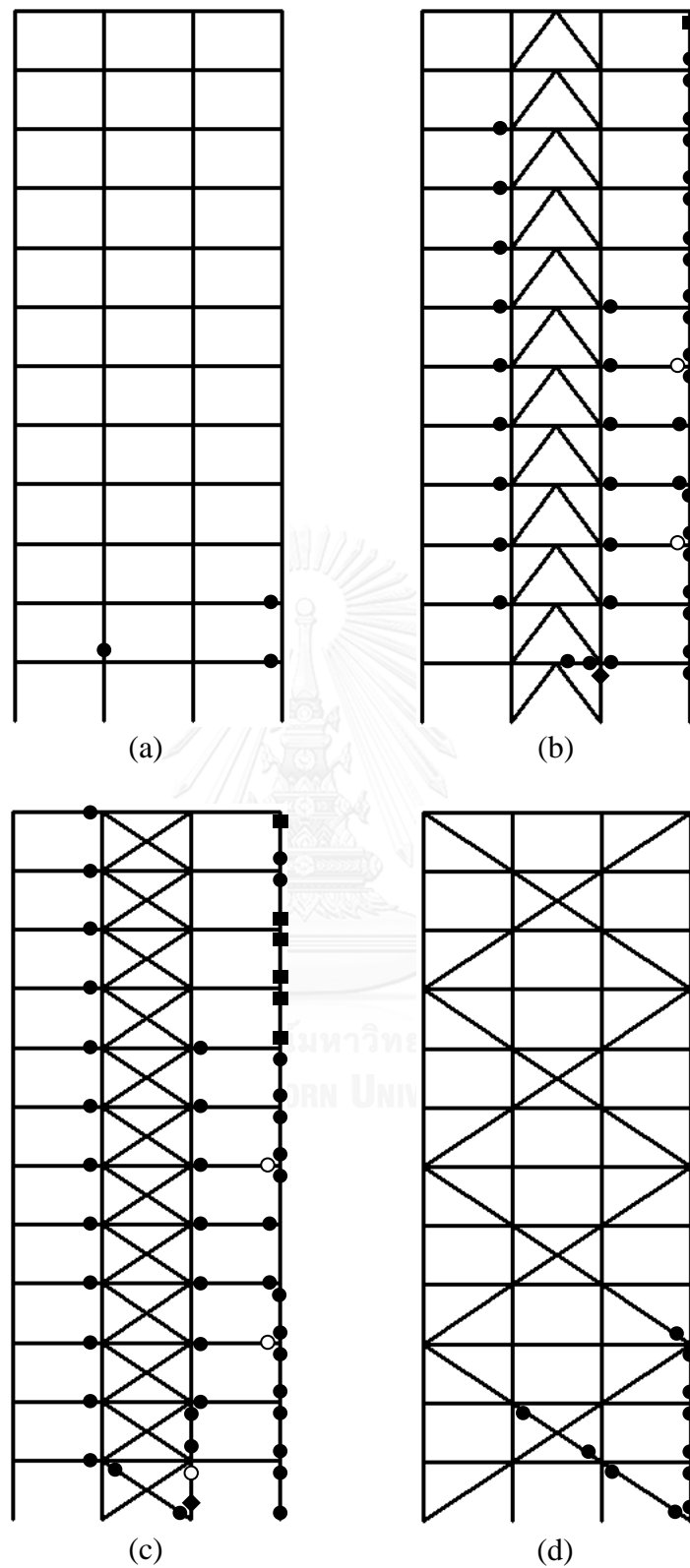


Figure 7.37: Examples 6: Hinge developments (● denotes hinge on perfectly plastic or 1st softening branch; ■, ♦ denote respectively hinge on 2nd, 3rd softening branch; and ○ denotes unloading hinge).

The computations have shown that using the same amount of structural steel, the mega X-bracing provides better enhancement to the peak load capacity of the existing structure than the inverted V- and X-bracing systems. In other words, it is more economical to achieve the target strength by using the mega X-bracing configuration. The inverted V- and X-braced structures behaved similarly and attained the maximum limit load at $\alpha = 36.32$ with $v = 0.54$ m and $\alpha = 34.85$ with $v = 0.68$ m, respectively. The mega X-braced composite frame reached the peak load capacity at $\alpha = 49.07$ with $v = 0.13$ m, which is 35% higher than the inverted V-braced frame and 41% higher than the normal X-braced frame. The conventional steel bracings enhance the lateral stiffness as well as the maximum load capacity of the unbraced frame significantly. For instance, the mega X-braced structure increased the peak load limit by 4 times and reduced the top lateral sway displacement by 5 times of the existing CES composite structure. It can be observed from Figures 7.3d-e that X-braced frame activated more plastic hinges on the second and third softening branch than the inverted V-braced frame which means that the CES columns contribute resistance more in the X-bracing system. For the mega X-braced structure, there was no unloading hinge or higher levels of softening hinge found in any member at the peak load. Only hinges on perfectly plastic or first softening branch were formed at some bracing members and columns (see Figure 7.3d), which has shown the efficiency of the mega X-bracing system. Since no snap-back or snap-through responses were encountered, the mega X-bracing solution is reliably more stable in terms of computational effort.

7.7 Concluding Remarks

The full spectrum of nonlinear responses for concrete encased steel composite structures has been traced and investigated by a simplified yet efficient approach with practical applications. A piecewise linear yield hyperplanes for concrete encased steel sections with an associated softening law have been proposed with detailed mathematical expressions. The proposed plasticity components have been implemented in a stepwise holonomic analysis scheme in order to validate with the experimental tests as well as to capture the complete responses of composite structures. Good results between the analyses and the tests have been achieved. In general, the proposed simplified analysis method is capable of predicting the CES structural responses including the difficult post-peak softening behavior with much less computational effort and time. In addition to the performance curves, full panoramas of the plastic hinge evolution have been illustrated for better investigation of the structural responses. By comparing the perfectly plastic with piecewise linear softening model, the computations have shown that the softening simulation has significant effects on the evaluation of post-peak response as well as the plastic hinge evolutions.

Effects of various steel bracing systems on the structural retrofitting for CES structures have been studied. The performance of common types of steel bracing such as V-bracing, inverted V-bracing, eccentrically inverted V-bracing, X-bracing, and mega X-bracing have been evaluated and compared. It is concluded that inverted V-bracing increases the lateral stiffness of the structure significantly (i.e. reduces the top sway displacement) as well as the maximum load-carrying capacity. However, it makes the retrofitting structure become more brittle. The efficiency of strength

enhancement from the X-bracing and eccentrically inverted V-bracing is generally the same as the inverted V-bracing. But in terms of stiffness, they are not as good as the inverted V-braced one. Unlike the mega X-bracing configuration, it usually enhances both the maximum strength and stiffness without deteriorating the ductility. Among the steel bracing systems in the present study, the V-bracing is the least efficient one in terms performance and economical view point.



CHAPTER 8

CONCLUSIONS AND RECOMMENDATIONS

8.1 Summary

An efficient fiber element based approach has been developed to simulate the nonlinear inelastic behaviors of concrete encased steel composite columns and beam-columns. Not only stub columns, where slenderness and geometric imperfection are negligible, but also slender CES columns were investigated. The present analysis approach realistically accommodates various important influences, i.e. materials nonlinearity, geometric nonlinearity, geometric imperfection, various levels of concrete confinement, local buckling of structural steel, and buckling of reinforcement bar (viz. after the crushing concrete material occur during simulation). The definition of concrete highly confinement zone for cross-shaped encased steel section has been proposed and validated with experimental tests. The proposed numerical approach is capable of tracing the complete structural performance including the challenging post-peak inelastic softening response. The maximum load-carrying capacity can be obtained as a by-product. Nonlinear inelastic load-lateral deflection curve, load-axial strain/shortening response, axial force-bending moment interaction diagram, and axial force-moment-curvature curve can be effectively generated. Despite rich features of the proposed numerical scheme, the computational time is highly efficient and suitable for practical design. An adaptive initial condition formulation with Müller numerical method has been developed to ensure the convergence solution. A total of 50 full-scale experimental tests of concrete encased

columns and beam-columns have been used to validate the developed numerical approach by comparing the ultimate load capacity, load-axial strain/shortening, and load-lateral deflection response curves. The verified analysis scheme was used to extend the study of critical influences on the performance of CES columns and beam-columns such as the spacing of lateral ties (effects of confinement level), column effective length ratio, load eccentricity ratio, structural steel yield stress, and concrete compressive strength.

As a result of mesoscale simulations of CES members, a piecewise yield function as well as an associated softening rule for CES sections have been proposed and implemented in a stepwise holonomic approach to capture full spectrum of CES structural responses. Mathematical expressions for the proposed plasticity components were derived and described in detail. The proposed composite structural analysis approach has been validated by comparing with relevant experimental tests. Both geometric and material nonlinearity were included in the analysis of CES structures. The proposed analysis method is capable of predicting the structural behaviors including the difficult post-peak softening response with less computational effort and time. In addition to the performance curves, panoramas illustrations of plastic hinge evolutions could be plotted event-by-event for insight investigation of the composite structural responses. After assessing the performance of CES structures, structural retrofitting by means of typical steel bracing systems has been carried out. Typical types of steel bracing systems such as V-bracing, inverted V-bracing, eccentrically inverted V-bracing, X-bracing, and mega X-bracing have been evaluated and compared. Some recommendations were given to select a suitable type of bracing configurations for the desired performance and economical view point.

8.2 Concluding Remarks

Some apposite concluding remarks from this study are as follows:

1. Various level of concrete confinement (viz. unconfined, partially confined, highly confined) need to be taken into account in numerical analysis of CES columns and beam-columns, since they affect mainly the maximum load-carrying capacity. However, these concrete confinements have less effect on the slender columns.
2. Two physical phenomena, i.e. buckling of reinforcement bars and local buckling of structural steel, play very important roles for predicting the realistic response of CES structures. They influence both the ultimate capacity and post-peak softening response.
3. Increasing the concrete compressive strength enhances the overall load capacity but it also deteriorates the ductility which makes the columns become more brittle.
4. For a column subjected to the eccentricity of load larger than half of its depth, increasing the concrete strength does not improve the load capacity significantly.
5. Higher structural steel yield stress enhances only the maximum strength capacity of the composite stocky columns more significantly than the slender ones, and does not affect the overall ductility.
6. Slender CES beam-columns are found to be more ductile than stocky ones. Similarly, columns with large eccentricity are more ductile than those with small eccentricity.

7. By comparing the perfectly plastic assumption with the proposed piecewise linear softening model, the computations have shown that it is indispensable to include the softening simulation in the CES structural analysis for realistic behavior. It truly has significant influences on the prediction of post-peak response as well as the evolution of plastic hinge formations.
8. The inverted V-bracing systems can increase the lateral stiffness of the existing unbraced structure significantly (i.e. reduces the sway displacement) as well as the maximum load-carrying capacity. However, using this bracing configuration will deteriorate the ductility and make the existing structure become more brittle.
9. For structures in the present study, strength enhancement from the X-bracing and eccentrically inverted V-bracing are generally the same as the inverted V-bracing. But regarding to the stiffness enhancement, the inverted V-bracing does a better job.
10. Generally, mega X-bracing system performs very well, since it enhances both the maximum strength and stiffness without deteriorating the ductility of existing structure.

8.3 Recommendations for Future Research

The recommendations for possible future research are described as follows:

1. The numerical model presented in the thesis has been developed for fully concrete encased steel composite columns/beam-columns. Similarly, the same approach can be implemented for other types of composite sections, e.g. partially encased steel sections, composite shear wall, and so on. It is

important to realize that for CES columns, stress in structural steel can develop up to yield point without activating local buckling due to the fully restrained from concrete. But for partially encased steel columns, steel flanges can experience local buckling before reaching the yield stress.

2. The present study focuses on CES structure with normal strength and normal weight concrete. It would be interesting to investigate the behavior of such composite structure for other materials, i.e. high-strength concrete, lightweight concrete, fiber-reinforced concrete, etc.
3. The effects of temperature dependent properties have not been incorporated in the present study yet. Therefore, the research on the CES structural behavior under elevated temperature is of important.
4. This study considers the structural response under static loading. Hence, further numerical models can be developed to investigate the CES structure under cyclic loading or preload effects.
5. The retrofitting of composite structure has been done by means of conventional steel braces under static loadings. For seismic-retrofitting structures, composite buckling restrained braces (BRBs) are commonly used. Instead of modeling the steel braces as perfectly plastic material, the BRBs can be modeled using the numerical approach as suggested in point 4 to study the composite structural responses during earthquake.

REFERENCES

- ACI (2011). "Building Code Requirements for Structural Concrete (ACI 318-11)."
- Al-Shahari, A., Y. Hunaiti and B. Ghazaleh (2003). "Behavior of lightweight aggregate concrete-encased composite columns." Steel & Composite Structures **3**(2): 97-110.
- Anslijn, R. and J. Janss (1974). Le calcul des charges ultimes des colonnes métalliques enrobées de béton, Centre de Recherches Scientifiques et Techniques de l'Industrie des Fabrications Métalliques.
- Brook, A., D. Kendrick and A. Meeraus (1988). "GAMS, a user's guide." ACM Signum Newsletter **23**(3-4): 10-11.
- Chen, C.-C. and N.-J. Lin (2006). "Analytical model for predicting axial capacity and behavior of concrete encased steel composite stub columns." Journal of Constructional Steel Research **62**(5): 424-433.
- Chen, C. and S. Yeh (1996). Ultimate strength of concrete encased steel composite columns. Proceedings of the third national conference on structural engineering.
- Chen, S., J. Teng and S. Chan (2001). "Design of biaxially loaded short composite columns of arbitrary section." Journal of structural engineering **127**(6): 678-685.
- Chiorean, C. G. (2013). "A computer method for nonlinear inelastic analysis of 3D composite steel–concrete frame structures." Engineering Structures **57**(0): 125-152.
- Cocchetti, G., G. Maier and X. Shen (2001). "Piecewise linear models for interfaces and mixed mode cohesive cracks." Computer Modeling in Engineering and Sciences **3**(3): 279-298.
- Cohn, M. and T. Rafay (1974). "Collapse load analysis of frames considering axial forces." Journal of the Engineering Mechanics Division **100**(4): 773-794.

- De Donato, O. and G. Maier (1972). "Mathematical programming methods for the inelastic analysis of reinforced concrete frames allowing for limited rotation capacity." International Journal for Numerical Methods in Engineering **4**(3): 307-329.
- Di Sarno, L. and A. S. Elnashai (2009). "Bracing systems for seismic retrofitting of steel frames." Journal of Constructional Steel Research **65**(2): 452-465.
- Dirkse, S. P. and M. C. Ferris (1995). "The path solver: a nonmonotone stabilization scheme for mixed complementarity problems." Optimization Methods and Software **5**(2): 123-156.
- El-Tawil, S. and G. G. Deierlein (1999). "Strength and ductility of concrete encased composite columns." Journal of Structural Engineering **125**(9): 1009-1019.
- El-Tawil, S., C. F. Sanz-Picón and G. G. Deierlein (1995). "Evaluation of ACI 318 and AISC (LRFD) strength provisions for composite beam-columns." Journal of Constructional Steel Research **34**(1): 103-123.
- Elghazouli, A. Y., J. M. Castro and B. A. Izzuddin (2008). "Seismic performance of composite moment-resisting frames." Engineering Structures **30**(7): 1802-1819.
- Ellobody, E. and B. Young (2011). "Numerical simulation of concrete encased steel composite columns." Journal of Constructional Steel Research **67**(2): 211-222.
- Ellobody, E., B. Young and D. Lam (2011). "Eccentrically loaded concrete encased steel composite columns." Thin-Walled Structures **49**(1): 53-65.
- Elnashai, A. S. and B. M. Broderick (1996). "Seismic response of composite frames—II. Calculation of behaviour factors." Engineering Structures **18**(9): 707-723.
- Fahnestock, L. A., R. Sause and J. M. Ricles (2003). Analytical and experimental studies on buckling restrained braced composite frames. Proc. of the international workshop on steel and concrete composite construction.

- Ferris, M. (1998). "Interfacing optimization and visualization software." Computer Sciences Department, University of Wisconsin: Madison, WI.
- Ferris, M. C. (2005). "MATLAB and GAMS: Interfacing optimization and visualization software." Mathematical Programming Technical Report 98: 19.
- Grierson, D. E. and S. B. Abdel-Baset (1977). "Plastic analysis under combined stresses." Journal of the Engineering Mechanics Division **103**(5): 837-854.
- Han, L.-H., W.-D. Wang and Z. Tao (2011). "Performance of circular CFST column to steel beam frames under lateral cyclic loading." Journal of Constructional Steel Research **67**(5): 876-890.
- Holzer, S., R. Melosh, R. Barker and A. Somers (1975). SINDER: a computer code for general analysis of two-dimensional reinforced concrete structures. Report. AFWL-TR. New Mexico. **1**: 74-228.
- Huang, Y., A. Wada, H. Sugihara, M. Narikawa, T. Takeuchi and M. Iwata (2000). "Seismic performance of moment resistant steel frame with hysteretic damper." Behaviour of Steel Structures in Seismic Areas: STESSA: 403-409.
- Iu, C. K., M. A. Bradford and W. F. Chen (2009). "Second-order inelastic analysis of composite framed structures based on the refined plastic hinge method." Engineering Structures **31**(3): 799-813.
- Kameshki, E. S. and M. P. Saka (2001). "Genetic algorithm based optimum bracing design of non-swaying tall plane frames." Journal of Constructional Steel Research **57**(10): 1081-1097.
- Kato, B. (1996). "Column curves of steel-concrete composite members." Journal of Constructional Steel Research **39**(2): 121-135.

- Kent, D. C. and R. Park (1971). "Flexural members with confined concrete." Journal of the Structural Division **97**(7): 1969-1990.
- Kim, D. K. (2005). A database for composite columns, Georgia Institute of Technology.
- Li, L., J. Sakai and C. Matsui (2003). Seismic behavior of steel encased reinforced concrete beam–columns. Proceedings of the international conference on advances in structures.
- Li, W., Q.-n. Li and W.-s. Jiang (2012). "Parameter study on composite frames consisting of steel beams and reinforced concrete columns." Journal of Constructional Steel Research **77**(0): 145-162.
- Li, W., Q.-n. Li, W.-s. Jiang and L. Jiang (2011). "Seismic performance of composite reinforced concrete and steel moment frame structures – state-of-the-art." Composites Part B: Engineering **42**(2): 190-206.
- Liang, Q. Q. (2009). "Performance-based analysis of concrete-filled steel tubular beam–columns, Part I: Theory and algorithms." Journal of Constructional Steel Research **65**(2): 363-372.
- Liang, Q. Q. (2009). "Performance-based analysis of concrete-filled steel tubular beam–columns, Part II: Verification and applications." Journal of Constructional Steel Research **65**(2): 351-362.
- Liang, Q. Q. (2011). "High strength circular concrete-filled steel tubular slender beam–columns, Part I: Numerical analysis." Journal of Constructional Steel Research **67**(2): 164-171.

- Liu, S.-W., Y.-P. Liu and S.-L. Chan (2012). "Advanced analysis of hybrid steel and concrete frames: Part 1: Cross-section analysis technique and second-order analysis." Journal of Constructional Steel Research **70**(0): 326-336.
- Mahin, S., P. Uriz, I. Aiken, C. Field and E. Ko (2004). Seismic performance of buckling restrained braced frame systems. Proc., 13th World Conf. on Earthquake Engineering, Int. Association of Earthquake Engineering (IAEE) Tokyo.
- Maier, G. (1970). "A matrix structural theory of piecewise linear elastoplasticity with interacting yield planes." Meccanica **5**(1): 54-66.
- Maier, G. (1971). "Incremental plastic analysis in the presence of large displacements and physical instabilizing effects." International Journal of Solids and Structures **7**(4): 345-372.
- Maier, G. (1976). "Piecewise linearization of yield criteria in structural plasticity." Solid Mechanics Archives **1**: 239-281.
- Maier, G., O. De Donato and L. Corradi (1972). Inelastic analysis of reinforced concrete frames by quadratic programming, Istituto di Scienza e Tecnica delle Costruzioni del Politecnico di Milano.
- Majid Zamani, S., A. Vafaei, C. Desai and M. Rasouli (2012). "Experimental investigation of behavior of steel frames with y-shaped concentric bracing." Journal of Constructional Steel Research **70**(0): 12-27.
- Mander, J. B., M. J. Priestley and R. Park (1988). "Theoretical stress-strain model for confined concrete." Journal of structural engineering **114**(8): 1804-1826.
- Massonnet, C. E. and M. A. Save (1965). Plastic analysis and design: beams and frames, Blaisdell Publishing Company.

- Matsui, C. (1979). "Study on elastic-plastic behavior of concrete-encased columns subjected to eccentric axial thrust." Annual Assembly of Architectural Institute of Japan: 1627-1628.
- Mirza, S. and B. Skrabek (1992). "Statistical analysis of slender composite beam-column strength." Journal of Structural Engineering **118**(5): 1312-1332.
- Mirza, S. A., V. Hyttinen and E. Hyttinen (1996). "Physical tests and analyses of composite steel-concrete beam-columns." Journal of Structural Engineering **122**(11): 1317-1326.
- Morino, S., C. Matsui and H. Watanabe (1984). "Strength of biaxially loaded SRC columns." Composite mixed construct., Proc. US/Japan.
- Müller, D. E. (1956). "A method for solving algebraic equations using an automatic computer." Mathematical Tables and Other Aids to Computation: 208-215.
- Park, R., M. Priestley and W. D. Gill (1982). "Ductility of square-confined concrete columns." Journal of the structural division **108**(4): 929-950.
- Patel, V. I., Q. Q. Liang and M. N. S. Hadi (2012). "High strength thin-walled rectangular concrete-filled steel tubular slender beam-columns, Part I: Modeling." Journal of Constructional Steel Research **70**(0): 377-384.
- Sanz Picon, C. (1992). Behavior of composite column cross sections under biaxial bending, MS Thesis.
- Shakir-Khalil, H. and J. Zeghiche (1989). "Experimental behaviour of concrete-filled rolled rectangular hollow-section columns." Structural Engineer **67**: 346-353.
- Shanmugam, N. E. and B. Lakshmi (2001). "State of the art report on steel-concrete composite columns." Journal of Constructional Steel Research **57**(10): 1041-1080.

Spacone, E. and S. El-Tawil (2004). "Nonlinear analysis of steel-concrete composite structures: State of the art." Journal of Structural Engineering **130**(2): 159-168.

SSRC, T. G. (Fourth Quarter 1979). "A specification for the design of steel-concrete composite columns." AISC Engineering Journal **4**: 101-115.

Tangaramvong, S. (2007). Mathematical Programming Approaches to the Plastic Analysis of Skeletal Structures under Limited Ductility PhD Thesis, The University of New South Wales.

Tangaramvong, S. and F. Tin-Loi (2007). "A complementarity approach for elastoplastic analysis of strain softening frames under combined bending and axial force." Engineering Structures **29**(5): 742-753.

Tangaramvong, S. and F. Tin-Loi (2008). "Simultaneous ultimate load and deformation analysis of strain softening frames under combined stresses." Engineering Structures **30**(3): 664-674.

Tangaramvong, S. and F. Tin-Loi (2009). "Limit analysis of elastoplastic frames considering 2nd-order geometric nonlinearity and displacement constraints." International Journal of Mechanical Sciences **51**(3): 179-191.

Tangaramvong, S. and F. Tin-Loi (2010). "The influence of geometric effects on the behavior of strain softening frames." Computational Mechanics **46**(5): 661-678.

Tangaramvong, S. and F. Tin-Loi (2011). "Mathematical programming approaches for the safety assessment of semirigid elastoplastic frames." International Journal of Solids and Structures **48**(6): 1011-1023.

Tangaramvong, S., F. Tin-Loi and W. Gao (2014). "Optimal retrofit of moment resisting frames using braces accounting for geometric nonlinearity and serviceability conditions." Engineering Structures **80**(0): 189-199.

- Taranath, B. S. (2011). Structural analysis and design of tall buildings: Steel and composite construction, CRC press.
- Tenchini, A., M. D'Aniello, C. Rebelo, R. Landolfo, L. S. da Silva and L. Lima (2014). "Seismic performance of dual-steel moment resisting frames." Journal of Constructional Steel Research **101**(0): 437-454.
- Thermou, G. E., A. S. Elnashai, A. Plumier and C. Doneux (2004). "Seismic design and performance of composite frames." Journal of Constructional Steel Research **60**(1): 31-57.
- Tsai, K., Y. Lien and C. Chen (1996). "Behaviour of axially loaded steel reinforced concrete columns." Journal of the Chinese Institute of Civil and Hydraulic Engineering **8**(4): 535-545.
- Tsai, M.-H. (2012). "A performance-based design approach for retrofitting regular building frames with steel braces against sudden column loss." Journal of Constructional Steel Research **77**(0): 1-11.
- Türker, T. and A. Bayraktar (2011). "Experimental and numerical investigation of brace configuration effects on steel structures." Journal of Constructional Steel Research **67**(5): 854-865.
- Wang, W.-D., L.-H. Han and X.-L. Zhao (2009). "Analytical behavior of frames with steel beams to concrete-filled steel tubular column." Journal of Constructional Steel Research **65**(3): 497-508.
- Wang, Y.-h., J.-g. Nie and C. S. Cai (2013). "Numerical modeling on concrete structures and steel–concrete composite frame structures." Composites Part B: Engineering **51**(0): 58-67.

Wang, Y. C. (1999). "Tests on slender composite columns." Journal of Constructional Steel Research **49**(1): 25-41.

Weng, C. C. and S. I. Yen (2002). "Comparisons of concrete-encased composite column strength provisions of ACI code and AISC specification." Engineering Structures **24**(1): 59-72.

Weng, C. C., S. I. Yen and H. S. Wang (2007). "A relative rigidity approach for design of concrete-encased composite columns." Journal of the Chinese Institute of Engineers **30**(4): 621-633.

Yen, J. R. (1991). "Quasi-Newton method for reinforced-concrete column analysis and design." Journal of Structural Engineering **117**(3): 657-666.

Zhao, G., Y. Li, B. Li, G. Xue, Z. Han and F. Cao (2005). Strength of slender steel reinforced concrete composite columns. Fourth International Conference on Advances in Steel Structures. Z. Y. Shen and G. Q. L. L. Chan. Oxford, Elsevier Science Ltd: 623-628.

Zhou, H. and T. L. Attard (2013). "Rehabilitation and strength sustainability of fatigue damaged concrete-encased steel flexural members using a newly developed polymeric carbon-fiber composite." Composites Part B: Engineering **45**(1): 1091-1103.

APPENDIX



จุฬาลงกรณ์มหาวิทยาลัย
CHULALONGKORN UNIVERSITY

VITA

Visoth Sambath KY was born on January 28, 1987 in Battambang Province, Cambodia. He studied at Preah Monivong high school and finished in 2005. Soon after high school, he went to Phnom Penh capital in order to continue his Bachelor degree. In 2005, he passed the entrance examination to conduct his study in the Department of Civil Engineering at Institute of Technology of Cambodia (ITC) for five years. During the final year of study at ITC in 2010, he also worked as an assistant project manager of a Korean company (LS FORMWORK CO., LTD) for a high-rise building project, Gold Tower 42, in Phnom Penh. As soon as he graduated from ITC in a major of Civil Engineering, he became a full-time lecturer in the Department of Civil Engineering at Norton University for one year. In 2011, he was awarded the Thailand Scholarship for Neighboring Countries to carry on his Master's degree in the field of Structural Engineering at Chulalongkorn University, Thailand. Since he could successfully finish his Master's degree one tri-semester before his two-year scholarship ended, he was able to apply on time for Chulalongkorn University Scholarship for ASEAN Countries in 2013 to pursue his PhD research successively in Structural Engineering Department at Chulalongkorn University. For only two years, he was capable of finishing his PhD research successfully in 2015 which is one year before the three-year scholarship ended.